1-1-2009

A validated finite element study of stress shielding in a novel hybrid knee implant

Ziauddin Mahboob
Ryerson University

A VALIDATED FINITE ELEMENT STUDY OF STRESS SHIELDING IN A NOVEL HYBRID KNEE IMPLANT

by

Ziauddin Mahboob
B.Eng. (Aerospace Engineering)
Ryerson University

A Thesis
Presented to Ryerson University
in partial fulfilment of the
requirements for the
Degree of Master of Applied Science
in the Program of
Aerospace Engineering

Toronto, Ontario, Canada, 2009

Author's Declaration

I hereby declare that I am the sole author of this thesis.

I authorise Ryerson University to lend this thesis to other institutions of individuals for the purpose of scholarly research.

I further authorise Ryerson University to reproduce this thesis by photocopying or by other means, in total or in part, at the request of other institutions or individuals for the purpose of scholarly research.

Acknowledgements

It is with sincere gratitude that I recgonise my instructors, peers, and friends who helped me piece together this thesis study from the ground up:

My supervisor Dr. Habiba Bougherara, for her consistent guidance throughout the duration of this study. In addition to her instruction on composite laminates, I am grateful for her much-needed encouragement that helped me see this thesis through.

Dr. Radovan Zdero, for his expert advice on experimental biomechanics, and for the use of the Martin Orthopaedic Biomechanics Laboratory at St. Michael's Hospital, Toronto.

Mr. Suraj Shah of the University of Toronto, and Mr. Anton Dubov of Ryerson University, for their invaluable expertise in experimental preparation and geometry modelling. Without the collaboration and guidance of them both, essential portions of this thesis would not have been possible.

Dr. Jeffrey Yokota, for his optimism, when I lacked it most.

My friends and colleagues Ms. Tawnya C. Cummins, Mr. Shoaib A. Shah, Mr. Shaheen Khurshid, and Mr. Richard Mohammed, for their prompt assistance in times of need.

Dr. Kamran Behdinan and Dr. Seyed M. Hashemi, for their past instruction in Finite Element Methods, which greatly prepared my understanding and competence in the field.

Ms. Leah Rogan, and the School of Graduate Studies at Ryerson University, for their assistance throughout the course of my post-graduate studies.

Last, but certainly not least, I recognise Julianna M. Cummins, and my brother Mamraj Mahboob, for their selfless, unconditional support in good times and bad. To you both, I will always remain indebted.

This page is intentionally left blank.

Abstract

A VALIDATED FINITE ELEMENT STUDY OF STRESS SHIELDING IN A NOVEL HYBRID KNEE IMPLANT

Ziauddin Mahboob, B.Eng.

A thesis presented to Ryerson University in partial fulfilment of the requirements for the degree of Master of Applied Science in the program of Aerospace Engineering

Toronto, Ontario, Canada, 2009

This study (1) proposes a hybrid knee implant design to improve stress transfer to bone tissue in the distal femur by modifying a conventional femoral implant to include a layer of carbon fibre reinforced polyamide 12, and (2) develops a finite element model of the prosthetic knee joint, validated by comparison with a parallel experimental study. The Duracon knee system was used in the experimental study, and its geometry was modelled using CAD software. Synthetic bone replicas were used instead of cadaveric specimens in the experiments. The strains generated on the femur and the implant surfaces were measured under axial compressive loads of 2000 N and 3000 N. A mesh of 105795 nodes was needed to obtain sufficient accuracy in the finite element model, which reproduced the experimental readings within 10-23% in six of the eight test locations. The model of the proposed hybrid design showed considerable improvements in stress transfer to the bone tissue at three test flexion angles of 0°, 20°, and 60°.

Table of Contents

List of Tables ..... **xi**

List of Figures ..... **xiii**

List of Medical Terminology ..... **xviii**

List of Abbreviations ..... **xx**

Nomenclature ..... **xxi**

1 Introduction **1**

2 Motivation **4**

2.1 Statistics of arthritis in Canada 4

2.2 Statistics of joint replacement in Canada 4

2.3 Statistics of primary vs. revision surgeries 5

3 The Human Knee **7**

3.1 Anatomy 7

3.1.1 Co-ordinate planes 7

3.1.2 Joints 8

3.1.3 Femur 8

3.1.4 Tibia and Fibula 9

3.1.5 The knee joint 9

3.1.6 Supports and stabilisers 10

3.2 Joint diseases 11

3.3 Biomechanics 12

3.3.1 The gait cycle 12

3.3.2 Motion of the knee joint 14

3.3.3 Relevant structural loads 15

3.4 Bone as an engineering structure 16

3.4.1 Porosity, Volume fraction, and Density 17
3.4.2 Cortical bone 18
3.4.3 Cancellous bone 20
3.5 Synthetic bone models 22
3.5.1 Synthetic models used in this study 23
4 Knee Arthroplasty 25
4.1 Reviewing the history 25
4.2 The Stryker® Duracon TS™ knee system 27
4.3 Prosthesis failure 28
4.3.1 Load transfer and Stress shielding 28
4.3.2 Bone resorption 29
4.3.3 Evidence of bone loss in the distal femur after TKA 30
4.3.4 Prevention of stress shielding to date 33
4.4 Polymer composites in knee prostheses 34
4.4.1 Ultra high molecular weight polyethylene (UHMWPE) 35
4.4.2 Carbon fibre reinforced polyamide 12 (CF/PA12) 38
4.5 Applying CF/PA12 composite in knee implants 42
5 Current study 44
5.1 Problem statement 44
5.2 Research question 44
5.3 Aims of this study 44
6 Experimental study 46
6.1 Synthetic bones in literature 46
6.2 Measuring strain on bone surfaces 49
6.2.1 Gauge factor and sensitivity 50
6.2.2 The Wheatstone quarter bridge circuit 51

6.2.3 Strain derived from voltage output 52
6.2.4 Strain gauge selection 52
6.3 Experiment overview 53
6.4 Preparation 55
6.4.1 Femoral and tibial assembly preparation 55
6.4.2 Strain gauge installation 58
6.4.3 Data acquisition and Signal analysis 59
6.5 Setup and alignment 62
6.5.1 Medial-lateral alignment 63
6.5.2 Anterior-posterior alignment using Fuji Prescale™ Film 64
6.6 Methodology 65
7 Geometry modelling 66
7.1 Femur 66
7.2 Implant components 69
8 Finite Element Modelling 73
8.1 Overview 73
8.2 Literature review 73
8.3 Material properties 75
8.3.1 Synthetic analogue bone models 76
8.3.2 CoCrMo alloy 77
8.3.3 UHMWPE 78
8.3.4 CF/PA12 79
8.3.5 Cement block 79
8.3.6 Summary 80
8.4 Finite elements 80
8.4.1 SOLID187 3-D 10-Node Tetrahedral Structural Solid 80

8.4.2 CONTA174 3D 8-node Surface-to-surface contact 81
8.4.3 TARGE170 3D Target segment 82
8.5 Assemblies 84
8.6 Boundary conditions 85
8.7 Contacts 85
8.7.1 Articulating surface contact 86
8.8 Mesh sensitivity and Convergence 87
8.9 Mesh refinement in the critical regions of interest 90
9 Results and Discussion 92
9.1 Experimental study 92
9.1.1 Contact area and alignment 92
9.1.2 Gauge measurements 92
9.2 Finite element study: Conventional design 94
9.2.1 FEA calculated surface strains 94
9.2.2 Stresses on the UHMWPE surface 95
9.3 Validation of the FE model 96
9.3.1 Comparing the experimental and FEA strain measurements 96
9.3.2 Comparing UHMWPE surface stress results with literature 100
9.4 Finite element study: Hybrid design 101
9.4.1 Resected condylar surface 102
9.4.2 Resected anterior distal femur 104
9.5 Further discussion 110
10 Concluding statements and Future considerations 112
APPENDIX A Load-displacement curves of the experimental study 115
APPENDIX B Surface strain readings on the FE model 116
B.1 2000 N load case 116

B.2 3000 N load case 117

APPENDIX C UHMWPE strain distribution 119

APPENDIX D Condylar surface principal stresses for 0° flexion 120

References 121

List of Tables

Table 2.1 Knee replacements in Canada by type of surgery, 2002-2006 [5] 6
Table 3.1 Summary of the stages in the gait cycle [54, 56] 14
Table 3.2 Joint force during various activities as per Paul [71] 16
Table 3.3 Mean anisotropic elastic properties of femoral cortical bone by Reilly and Burstein [75] 18
Table 3.4 Mean anisotropic ultimate properties of femoral cortical bone by Reilly and Burstein [75] 19
Table 3.5 Proximal tibia cancellous bone properties 21
Table 3.6 Distal femur cancellous bone properties 21
Table 3.7 Dimensions of the fourth generation femur model [115] 23
Table 3.8 Isotropic properties of simulated bone [111] 24
Table 4.1 Elastic moduli at room temperature for different types of UHMWPE [164] 35
Table 4.2 CF/PA12 composite constituent properties [40] 39
Table 4.3 2006 compression test results of CF/PA12 specimens by Campbell *et al.* [38, 39] 40
Table 4.4 2008 compression test results of CF/PA12 cylinders by Campbell *et al.* [41] compared to cortical tissue 42
Table 6.1 Approximate mean stiffness values of composite femurs, dried cadaveric femurs and frozen cadaveric femurs as published by Cristofolini *et al.* [110] 48
Table 6.2 Vishay® 350-Ohms strain gauge specifications [199] 53
Table 8.1 Simulated cortical and cancellous bone properties 77
Table 8.2 Cobalt-chromium alloy properties 78
Table 8.3 UHMWPE properties 79
Table 8.4 CF/PA12 properties 79
Table 8.5 Concrete properties 80
Table 8.6 Material properties used in the FE model of the bone-implant system 80
Table 8.7 Mesh characteristics and associated vertex displacements 89
Table 9.1 Gauge locations and strain measurements 93
Table 9.2 Gauge locations and strain measurements 94
Table 9.3 FEA results of the UHMWPE surface stress 95
Table 9.4 2000 N load case – FEA and experimental surface strain results (location of gauge readings suspected of error shaded grey) 96
Table 9.5 3000 N load case – FEA and experimental surface strain results (location of gauge readings suspected of error shaded grey) 97
Table 9.6 Published maximum stresses generated in UHMWPE components (~2000 N) 100

Table 9.7 maximum stresses generated in UHMWPE components (3000 N) 100
Table 9.8 Condylar surface von Mises stresses under 3000 N (anomaly shaded in grey) 104
Table D.1 Condylar surface principal stresses [MPa] for 0° flexion 120

List of Figures

Figure 1.1 Typical knee implant system *in vivo* 2
Figure 2.1 Number of hospitalisations for knee replacements in Canada, 1995-2006 [5] 5
Figure 2.2 Chart of primary surgeries compared to revisions, 2005-2006 [5] 6
Figure 3.1 Anatomical planes of reference [47] 7
Figure 3.2 Distal end of the femur. Anterior view (left), Posterior view (right) [49] 8
Figure 3.3 Proximal end of the tibia. Anterior view (left), Posterior view (right) [49] 9
Figure 3.4 Articulating surfaces of the knee joint [49] 10
Figure 3.5 Ligaments of the knee joint [49] 11
Figure 3.6 Wear of cartilage in the femoral condyle; [52] (left), [53] (right) 12
Figure 3.7 The phases of the gait cycle [57] 13
Figure 3.8 Knee joint compressive force during normal, level gait from Paul [71] 16
Figure 3.9 Knee joint forces during slow (1.10 m/s), normal (1.48 m/s), and fast (2.01 m/s) level walking from Paul [65] 16
Figure 3.10 Viscoplastic behaviour of cortical bone [77] 20
Figure 3.11 Viscoelastic behaviour in cortical tissue shown by strain rate sensitivity [78] 20
Figure 3.12 Fourth generation, medium, left femur [115] 23
Figure 4.1 The Stryker® Duracon™ knee system [130] 27
Figure 4.2 Pre-op (left) and post-op (right) radiographs using a Duracon impant system [131] 27
Figure 4.3 Diagram showing load transmission from femur to tibia (arrows), and region of no load (labelled) as per Cameron and Cameron [151] 30
Figure 4.4 Distal femur regions marked into 'zones' by Mintzer *et al.* [23] 31
Figure 4.5 Postoperative (top) and follow up (bottom) radiographs showing significant bone loss in zones 1, 2 and 3, from Mintzer *et al.* [23] 31
Figure 4.6 Lateral radiograph with arrowheads showing osteopenia behind the anterior flange; from van Loon *et al.* [24] 32
Figure 4.7 Strain rate dependence of UHMWPE in compression [165] 36
Figure 4.8 Temperature dependence of UHMWPE in compression [165] 36
Figure 4.9 Linear elasticity model compared to actual behaviour in compression [165] 36
Figure 4.10 Ogden hyperelasticity model compared to actual behaviour in compression [165] 36
Figure 4.11 Linear viscoelasticity model (1-term Prony series) compared to actual behaviour in compression [165] 37

Figure 4.12 Linear viscoelasticity (2-term Prony series) model compared to actual behaviour in compression [165] 37
Figure 4.13 J_2-plasticity model compared to actual behaviour in compression [165] 37
Figure 4.14 Hybrid model by Bergström and colleagues [166-169] compared to actual behaviour in compression 37
Figure 4.15 Inflatable bladder moulding to manufacture CF/PA12 THA femoral stems [40] 39
Figure 4.16 Typical compression stress-strain curve of CF/PA12 cylinders by Campbell *et al.* [38, 39] ..41
Figure 4.17 Failed stem samples after compression testing: a) barrelling, and b) buckling along the 45° shear plane [38, 39] 41
Figure 6.1 Experimental setup to obtain structural bending stiffness by McNamara *et al.* [114] 47
Figure 6.2 Left to right: axial compression, torsion, and four point bending experiments by Cristofolini *et al.* [110] 48
Figure 6.3 Diagram of a foil strain gauge [193] 50
Figure 6.4 Strain gauge in a quarter bridge Wheatstone circuit [194] 51
Figure 6.5 Regular Wheatstone bridge circuit [197] 52
Figure 6.6 Quarter bridge circuit with one strain gauge [195] 52
Figure 6.7 Vishay® 350-Ohms uniaxial linear-pattern strain gauge model CEA-06-125UW-350 [199] ..53
Figure 6.8 Instron® FastTrack™ 8874 [201] 54
Figure 6.9 Instron® FastTrack™ 8800 controller panel 54
Figure 6.10 Profile of the Duracon system femoral component showing anterior (A) and posterior (P) sides [203] 55
Figure 6.11 Left femur setup showing strain gauge locations in the bone-implant system rigidly fixed in a cement block 56
Figure 6.12 Fracture of a PFC femoral component from Duffy *et al.* [204] 57
Figure 6.13 Superior (left) and anterior (right) view of the tibial components implanted in a brick of synthetic cancellous bone tissue 57
Figure 6.14 Three lead wire conductors separated and soldered to a strain gauge 59
Figure 6.15 Illustration of circuit options to connect a strain gauge to the quarter bridge circuit [197] 60
Figure 6.16 A two-channel DSub-15-pin connector can be attached to wiring from two strain gauges 61
6.17 UNI2-8 all-purpose eight-channel amplifier (left, from [206]) is installed in the CRONOS-PL unit to accept the four DSub-15 connectors (right) 61
Figure 6.18 DSub-15s connected to the CRONOS-PL unit 62
Figure 6.19 Experimental setup 63

Figure 6.20 Close-up showing the relative ease of medial-lateral alignment due to the complementary tibial (concave) and femoral (convex) surfaces....64
Figure 6.21 Two-sheet type pressure sensitive Fuji Prescale™ film [209]....65
Figure 7.1 Mimics™ screenshot showing CT images in the coronal, axial, and sagittal planes (clockwise from top left) at a particular point location on the femur....66
Figure 7.2 Surface roughness, and cavity in the geometry....67
Figure 7.3 Grid generated and improved....67
Figure 7.4 Full femur final CAD model....68
Figure 7.5 Resected distal femur showing cancellous (darker core) and cortical (lighter outer layer) tissue....68
Figure 7.6 Femoral component CAD model....69
Figure 7.7 Exploded view of the hybrid femoral component, showing the CF/PA12 layer....70
Figure 7.8 UHMWPE tibial bearing CAD model....71
Figure 7.9 Tibial tray and fixation stem CAD model....71
Figure 7.10 Exploded view of the conventional bone-implant assembly....72
Figure 8.1 SOLID187 element description [224]....81
Figure 8.2 SOLID187 stress output directions [224]....81
Figure 8.3 CONTA174 element description [225]....82
Figure 8.4 TARGE170 element description [227]....83
Figure 8.5 From left to right, assemblies representing 0°, 20°, and 60° flexion....84
Figure 8.6 Boundary conditions on the assembly for the 3000 N load case....85
Figure 8.7 Contact locations in the conventional implant assembly....86
Figure 8.8 Contact locations in the hybrid implant assembly....86
Figure 8.9 Contact region between the femoral component and the UHMWPE articulating surface....87
Figure 8.10 Location of the vertices used to test for mesh sensitivity....88
Figure 8.11 From left to right, Mesh 1 to Mesh 5, successively refined. Mesh 4 was chosen....88
Figure 8.12 Change in displacement for Vertex 1....89
Figure 8.13 Change in displacement for Vertex 2....89
Figure 8.14 Change in displacement for Vertex 3....90
Figure 8.15 The UHMWPE surface mesh refined at the contact region....90
Figure 8.16 The anterior region of the distal femur showing mesh refinement at the surfaces....91
Figure 9.1 Contact location and area, 2000 N case....92
Figure 9.2 Contact location and area, 3000 N case....92
Figure 9.3 Experimental strain measurements for each load case....93

Figure 9.4 Calculated strains for each load case using the FE model 94
Figure 9.5 2000 N case – UHMWPE surface von Mises stress distribution 95
Figure 9.6 3000 N case – UHMWPE surface von Mises stress distribution 95
Figure 9.7 2000 N load case – Comparing experimental and FE-calculated strains 96
Figure 9.8 3000 N load case – Comparing experimental and FE-calculated strains 97
Figure 9.9 2000 load case – Experimental strain vs. FE-calculated strain 99
Figure 9.10 3000 N load case – Experimental strain vs. FE-calculated strain 99
Figure 9.11 Comparing maximum UHMWPE stresses under a compressive load of around 2000 N 101
Figure 9.12 Comparing maximum UHMWPE stresses under a compressive load of 3000 N 101
Figure 9.13 Zero-degree flexion – Equivalent von Mises stress distribution on the condylar surfaces below the implant 102
Figure 9.14 20° flexion – Equivalent von Mises stress [MPa] distribution on the condylar surface 103
Figure 9.15 60° flexion – Equivalent von Mises stress [MPa] distribution on the condylar surface 103
Figure 9.16 0° flexion – Equivalent von Mises stress [MPa] distribution contours in the anterior distal femur 105
Figure 9.17 Equivalent von Mises stress [MPa] distribution in the anterior distal femur 106
Figure 9.18 20° flexion – Equivalent von Mises stress [MPa] distribution in the anterior distal femur ... 108
Figure 9.19 60° flexion – Equivalent von Mises stress [MPa] distribution in the anterior distal femur ... 109
Figure 9.20 X-ray radiograph from van Loon *et al.* [24] showing bone loss in the same region 110
Figure 9.21 Stress-shielded region in the bone tissue shown by the FE study at 0° flexion 110
Figure 9.22 Stress-shielded region shown by the FE study at 20° flexion 110
Figure 9.23 Stress-shielded region shown by the FE study at 60° flexion 110
Figure A.1 Axial load vs. Displacement, 2000 N case 115
Figure A.2 Axial load vs. Displacement, 3000 N case 115
Figure B.1 FEA strain readings (με) taken at Location 1 116
Figure B.2 FEA strain readings (με) taken at Location 2 116
Figure B.3 FEA strain readings (με) taken at Location 3 116
Figure B.4 FEA strain readings (με) taken at Location 4 116
Figure B.5 FEA strain readings (με) taken at Location 5 and Location 6 117
Figure B.6 FEA strain readings (με) taken at Location 7 117
Figure B.7 FEA strain readings (με) taken at Location 8 117
Figure B.8 FEA strain readings (με) taken at Location 1 117
Figure B.9 FEA strain readings (με) taken at Location 2 117
Figure B.10 FEA strain readings (με) taken at Location 3 118

Figure B.11 FEA strain readings (με) taken at Location 4 118
Figure B.12 FEA strain readings (με) taken at Location 5 and Location 6 118
Figure B.13 FEA strain readings (με) taken at Location 7 118
Figure B.14 FEA strain readings (με) taken at Location 8 118
Figure C.1 2000 N case – UHMWPE surface von Mises strain distribution (exaggerated deformation) .119
Figure C.2 3000 N case – UHMWPE surface von Mises strain distribution 119
Figure C.3 Linear elasticity model compared to actual compression behaviour of UHMWPE as per Bergström [165] 119
Figure D.1 Conventional design M aximum and Minimum Principal stress at zero flexion 120
Figure D.2 Hybrid design Maximum and Minimum Principal stress at zero flexion 120

List of Medical Terminology [1]

abduction	outward movement, away from the median axis of the body
adduction	inward movement, towards the median axis of the body
amphiarthrosis	slightly movable joint
arthritis	acute or chronic inflammation of a joint, often accompanied by pain and structural changes and having diverse causes, as infection, crystal deposition, or injury
arthroplasty	the surgical repair of a joint or the fashioning of a movable joint, using the patient's own tissue or an artificial replacement
articular	of or related to the joints
bicondylar	of or related to both condyles (of the femur or tibia)
biocompatibility	chemical, mechanical, and surface compatibility of a foreign object by the living tissue surrounding it
biomimetic	imitating biology and/or living tissue
cancellous bone	spongy bone tissue
condylar	of or related to the condyles in the distal femur or proximal tibia
cortical	hard, compact bone tissue
CT or CAT	computer tomography or computed axial tomography; an X-ray technique for producing cross-sectional image of the body
diarthrosis	freely movable joint, synovial joint
distal	situated away from the point of origin or attachment, as of a limb or bone; terminal
femur	thighbone; a bone in the human leg extending from the pelvis to the knee, that is the longest, largest, and strongest in the body
lateral	direction away from the midline of the body or the sagittal plane
medial	inward direction towards the midline of the body
median axis	axis parallel to the sagittal plane; axis that divides the body into right and left halves
mediolateral	axis extending in the medial and lateral directions
osteoarthritis	the most common form of arthritis, usually occurring after middle age, marked by chronic breakdown of cartilage in the joints leading to pain, stiffness, and swelling.
osteolysis	dissolution or degeneration of bone tissue through disease
osteopenia	reduction of bone mineral density in skeletal tissue below healthy levels
osteoporosis	increase in bone porosity and subsequent decrease in bone density through disease; usually occurs after osteopenia

patella	the flat, movable bone at the front of the knee; kneecap
patellofemoral	related to the patella and the femur
prosthesis	an implant; a device, either external or implanted, that substitutes for or supplements a missing or defective part of the body
proximal	situated toward the point of origin or attachment, as of a limb or bone
resorption	dissolution or removal of a substance; e.g. bone tissue
sagittal plane	a longitudinal plane that divides the body of a bilaterally symmetrical animal into right and left sections
synarthrosis	immovable joint
synovial	belonging to, or related to the synovial joint or diarthrosis (*see* diarthrosis)
talus	anklebone; the uppermost bone of the proximal row of bones of the tarsus
tibia	shinbone; the inner of the two bones of the leg, that extend from the knee to the ankle and articulate with the femur and the talus
tibiofemoral	related to the tibia and the femur
unicondylar	of or related to only one condyle

List of Abbreviations

ACL	Anterior cruciate ligament
A-P	Anterior-posterior
ASTM	American Society of Testing and Materials
BMD	Bone mass density
CF	Carbon fibre
CIHI	Canadian Institute for Health Information
CJRR	Candian Joint Replacement Registry
CoCrMo	Cobalt-chromium-molybdenum alloy
CT	Computer tomography, or computed axial tomography (CAT)
DICOM	Digital Imaging and Communications in Medicine
FE	Finite element
GF	Gauge factor
IGES	Initial Graphics Exchange Specification
M-L	Medial-lateral
PA	Polyamide
PCA	Porous coated anatomical (knee implant)
PCL	Posterior cruciate ligament
PMMA	Polymethyl methacrylate
PFC	Press fit condylar (knee implant)
THA	Total hip arthroplasty
TKA	Total knee arthroplasty
UHMWPE	Ultra high molecular weight polyethylene

Nomenclature

Latin

A	Cross section area of a conductor
I	Current
P	Porosity
V_f	Volume fraction
E	Elastic modulus / Modulus of elasticity / Young's modulus
E_1 or E_L	Longitudinal elastic modulus (along the fibre) of a lamina/ply
E_2, or E_T	Transverse elastic modulus (perpendicular to the fibre) of a lamina/ply
E_3	Elastic modulus in the direction normal to the longitudinal-transverse (1-2) plane of a laminate/ply
E_x, E_z, E_z	Elastic modulus of multi-layer composite laminates in the global x-, y-, and z-direction
G, G_{xy}, G_{yz}, G_{xz}	Shear modulus
GF	Gauge factor of a strain gauge
L	Length of a conductor/resistor (e.g. strain gauge foil)
R	Resistance of a conductor
R_1, R_2 , R_3, R_4	Resistance of a Wheatstone bridge circuit element
R_G	Resistance of a strain gauge
V	Voltage
V_{EX}	Source excitation voltage in a Wheatstone bridge ciruit
V_o	Output voltage in a Wheatstone bridge circuit

Greek

Δ	Change in a property; usually followed by the notation of the property
Ω	Ohms, unit of resistance
ε	Strain
$\mu\varepsilon$	Microstrain ($\varepsilon \times 10^{-6}$)
v, v_{xy}, v_{yz}, v_{xz}	Poisson's ratio
ρ	Resistivity of a conductor
ρ_{app}	Apparent density
ρ_{tiss}	Tissue density

1 INTRODUCTION

Understanding the human body as a machine, and its behaviour as mechanisms, has enabled researchers to repair and heal the body – thereby improving quality of life for the diseased or disabled. Such an understanding of joint function has contributed greatly towards the design of replacement 'prosthetic' joints [2]. The field of joint replacement, or *arthroplasty*, is one that has been developing over the last century, particularly in orthopaedics [3, 4]. Hip and knee implants remain the most common joint replacements conducted worldwide, and the number of primary surgeries continues to increase with every year [3, 5]. In view of the worldwide increase in knee arthroplasty, there is a constant focus on ways to improve the design of prosthetic joints. As artificial joints need to sufficiently complement biological tissue under physiologic loads [2, 6], the need to design long-lasting implants is paramount – especially since the age group of patients opting for joint replacement seem to be getting younger [7].

In the spirit of continual improvement, this study addresses one of the many ongoing areas of research on knee implant components – stress shielding and subsequent bone loss. 'Stress shielding', or equivalently called 'load shielding' or 'strain shielding', is a postoperative phenomenon that occurs in the 'bone-implant' system, where the higher modulus implant (usually metallic alloys with elastic modulus between 100-200 GPa) assumes a large portion of the applied load usually carried by the bone tissue (modulus up to 20 GPa). Since the bone experiences lesser load in the presence of the implant than it did before surgery, it naturally adapts to this decreased loading scenario by reducing its mineral density (osteopenia) and becoming more porous (osteoporosis) [2, 8]. It has been shown that the degree of stress shielding is directly proportional to the degree of stiffness mismatch [9, 10]. This 'remodelling' process is an example of how living tissue tends to degenerate when put out of use; in this case by the insufficient load transfer from the implant to the peripheral bone tissue. This process can be a gradual but direct consequence of arthroplasty, and can aggravate the overall loss of bone tissue (osteolysis) [11].

The loss of surrounding bone tissue directly affects implant fixation causing interface de-bonding and micromotions, and eventually leading to implant loosening [12, 13]. It had been suggested that osteolysis eventually ends when the bone tissue reaches an 'equilibrium' density [8], but further evidence indicates otherwise [14-17]. Bone loss due to stress shielding can be an ongoing phenomenon: as the bone density decreases, the relative strength of the implant material increases causing the implant to carry even more load; further compromising the bone tissue [2]. So goes the cycle of continuing bone loss which leads to catastrophic failure of the loosening implant, causing the patient much pain and necessitating a revision surgery. Knee implants concern two long bones – the bottom end of the femur (distal femur), and the

upper end of the tibia (proximal tibia). As such, a complete knee implant 'system' includes components for the femur (femoral component in Figure 1.1) and the tibia (polyethylene surface and stemmed tibial plate/tray in Figure 1.1). While several different factors contribute to osteolysis after knee arthroplasty [11, 18, 19], the prevalence of stress shielding-related osteolysis has been shown convincingly in the distal femur [8, 15-17, 20-25], and is still debated in the proximal tibia [26-31].

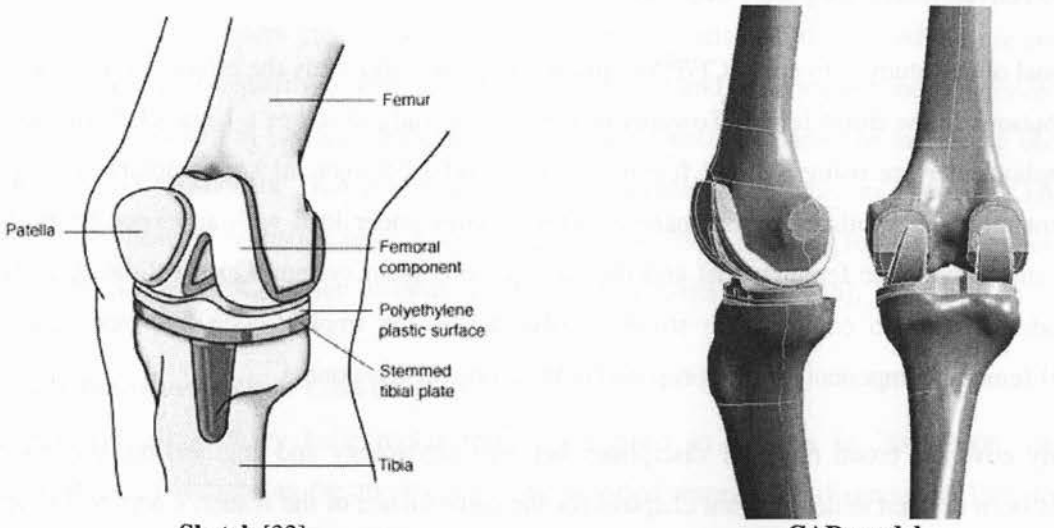

Sketch [32] **CAD model**

Figure 1.1 Typical knee implant system *in vivo*

This study focuses specifically on the distal femur, and explores a way to reduce stress shielding in this location by pursuing the concepts of 'isoelasticity' [33-36] and 'biomimetism' [37]. An 'isoelastic' implant is meant to replicate the elastic properties of bone tissue, such that the combined bone-implant assembly deforms as one unit [35]. 'Biomimetism' is a broader, but similar concept describing the mimicry of biology or living tissue [37]. Of course, the perfect isoelastic/biomimetic implant in reality is far-fetched. But designing an implant material to mimic bone tissue in deformation and cyclic fatigue is a significant step in improving the load transfer between the implant and bone. It follows that any improvement in load transfer (i.e. reduction in stress shielding) will contribute towards reducing bone loss, thereby increasing implant life.

The innovation in this study is a novel 'hybrid' femoral component, designed to include a layer of carbon-fibre reinforced polymer along its inner surface to act as an 'interface layer' with the femoral bone tissue. The idea is to improve the sudden change in elastic modulus across the implant-bone interface by introducing a nearly biomimetic material in between. As will be discussed later, the composite used is carbon-fibre reinforced polyamide 12 (CF/PA12), developed between 2006 and 2008 by a team of researchers from the École Polytechnique de Montréal (Montreal, QC, Canada) and the Industrial Materials Institute (National Research Council, Boucherville, QC, Canada) [38-41]. CF/PA12 has been

successfully shown to replicate the properties of cortical bone tissue when manufactured under optimum conditions, and has been used to manufacture hip implants with promising *in vitro* results [39-42]. Since these CF/PA12 orthopaedic hip implants are a very recent innovation, and have not yet been used in hip arthroplasty, its clinical performance remains to be seen. However, the *in vitro* compressive and fatigue performance CF/PA12 implants indicates the excellent *in vivo* potential of this material as a biomimetic alternative to conventional orthopaedic implants [41].

The broad goal of this study is to apply CF/PA12 in knee implants, and study the effect of this material on stress distributions in the distal femur. Towards this goal, this study develops a finite element model of the bone-implant interface using realistic femur geometry and a commercial knee implant system. The finite element model is validated by comparing surface strains under load with an experimental study conducted using a synthetic femur model and the same knee implant system. Once validated, the finite element model is used to compare the stress transfer across the implant-bone interface between a conventional femoral component and the proposed hybrid femoral component.

As this study covers a broad range of disciplines between physiology and engineering, the reviewed literature has been divided under relevant chapters for the convenience of the reader. *Chapter 2* describes the statistics of primary orthopaedic replacements conducted in Canada, and discusses the increasing number of primary and revision knee replacements procedures. *Chapter 3* provides a description of the human knee, touching on relevant subtopics of joint anatomy, diseases (pathology), biomechanics, mechanical properties, and synthetic bone models. *Chapter 4* discusses knee replacements, prosthetic knee implants and their failure, a further discussion of bone loss in the distal femur, and descriptions of polymer composites relevant to this study. *Chapter 5* lays out the research question, the goals and scope of this study.

Chapter 6 describes the experimental study conducted, and includes a review of synthetic simulated bone models as viable replacements of cadaveric specimens. *Chapter 7* describes and displays the CAD modelling of the femur and implant geometry required to develop the finite element model. *Chapter 8* concerns all the finite element analyses conducted for this study, including tests of the conventional and hybrid femoral components. *Chapter 9* discusses the results of the experimental and finite element studies, their validation and their interpretation. *Chapter 10* discusses the limitations of this study, a brief commentary on the future work possible based on this study, including the potential of the validated finite element model developed in this study for further knee implant-related research.

2 MOTIVATION

Osteoarthritis and related conditions constitute a large group of disorders affecting the joints, ligaments, tendons, bones and other components of the musculoskeletal system. These medical conditions are highly prevalent, and are major causes of morbidity, loss of productivity of patients, and health care utilisation. Knee replacements contribute greatly in treating knee joint arthritis, and the procedures are cost effective means of improving the quality of life by reducing joint pain and encouraging independence in patients who do not respond to non-surgical therapies. The following statistics show the increasing occurrence of osteoarthritis and subsequent TKA procedures that merit continuing studies in improving knee implant systems. All following statistics have been obtained from the Canadian Joint Replacement Registry (CJRR), published by the Canadian Institute for Health Information (CIHI) [5].

2.1 Statistics of arthritis in Canada

In a survey of all *primary* knee replacements performed in Canada in 2005-2006, degenerative osteoarthritis was indicated as the most commonly reported responsible diagnosis (93%), followed by inflammatory (rheumatoid) arthritis (4%), and post-traumatic arthritis (2%). These statistics indicate only the most responsible cause of knee replacement for each patient surveyed, as diagnosed by participating surgeons [5].

2.2 Statistics of joint replacement in Canada

Figure 2.1 displays the progression of knee replacement hospitalisations in Canada between the fiscal years 1995-1996 and 2005-2006. This data includes total and partial knee replacements. Data for the fiscal year 2005-2006 are the most recent Canadian data available. There were 68,746 hospitalizations for hip and knee replacements in Canada on Canadian residents in 2005–2006, representing a 10-year increase of 101% from 34,281 procedures in 1995–1996 and a one-year increase of 17% from 58,714 procedures in 2004–2005. This one-year increase is larger than that observed in the previous fiscal year (2004–2005), when the one year increase from the previous year was under 10% (9.7%). In 1995–1996, the number of hip replacements exceeded the number of knee replacements in Canada (17,358 versus 16,923 surgeries, respectively). Since then, knee replacements have annually surpassed the number of hip replacements, and the gap has been steadily widening. In 2005–2006, there were 40,701 hospitalizations for knee replacements. The number of knee replacements in 2005–2006 more than doubled since 1995–1996 (an increase of 140%), with a 21% increase compared to the previous year (2004–2005) [5]. The

140% increase in knee replacement hospitalisations since 1995-1996 indicates the prevalence of the procedure and the necessity to contribute towards its improvement.

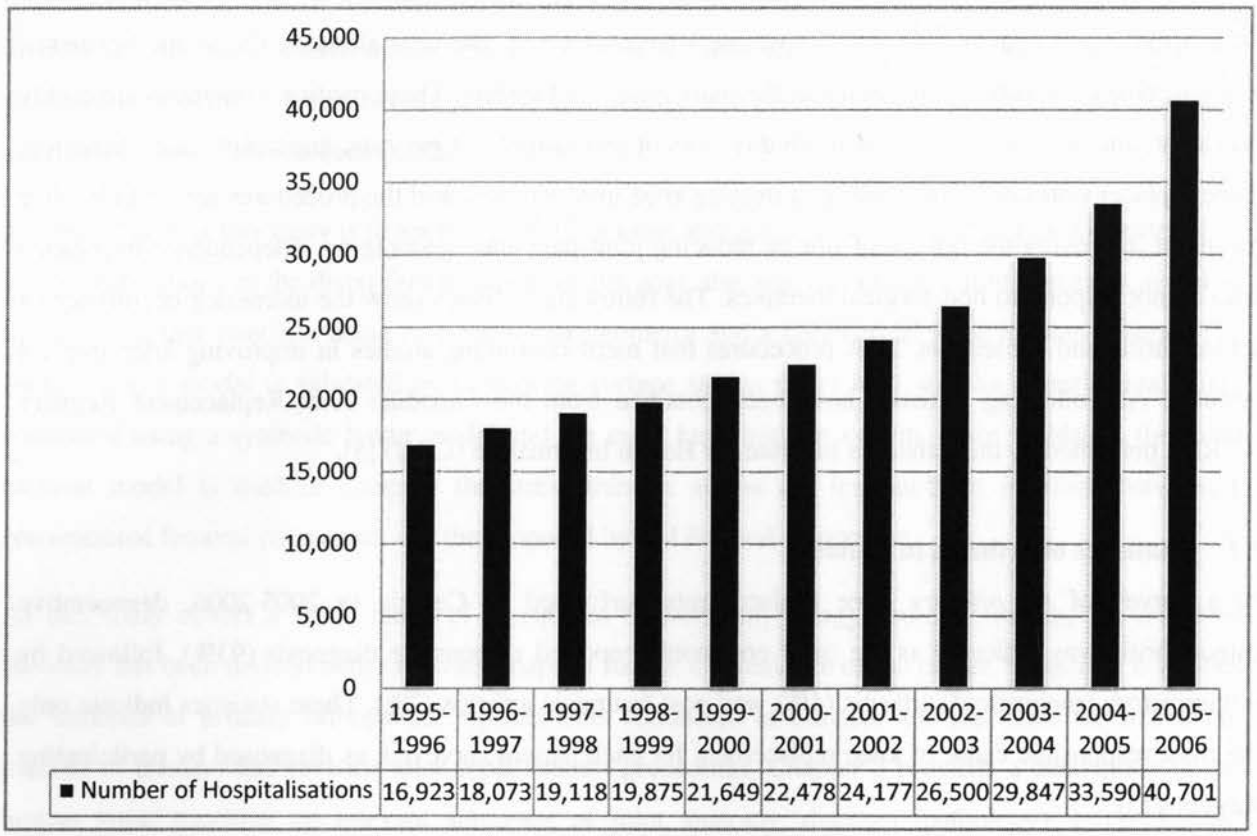

Figure 2.1 Number of hospitalisations for knee replacements in Canada, 1995-2006 [5]

2.3 Statistics of primary vs. revision surgeries

As shown in Table 2.1, of the 18,124 knee replacements performed on Canadians in 2005-2006, 17,082 (95%) involved primary surgeries and the remaining 973 involved revisions. Of the revisions, 779 surgeries (4.3% of the total) were first revisions, 124 (0.7%) were second revisions, 20 (0.1%) were third revisions, and the remaining 0.1% are fourth revisions of higher.

Figure 2.2 puts these statistics in perspective. In the table, column 'N' displays the number of replacements, and the column '%' displays the same data as a percentage of the total number of replacements performed in that year (given in the last row).

Type of Replacement	2002–2003		2003–2004		2004–2005		2005–2006		3-Year Increase
	N	%	N	%	N	%	N	%	%
Primary	9,589	94	13,905	94	17,860	94	17,082	94	78
Revision	615	6	932	6	1,132	6	973	5	58
First revision	502	5	768	5	918	5	779	4	55
Second revision	94	1	133	1	167	1	124	1	32
Third revision	13	0	21	0	30	0	20	0	54
> Third revision	6	0	10	0	17	0	13	0	117
Excision	5	0	5	0	8	0	11	0	120
Not Stated	16	0	16	0	23	0	58	0	263
Total	10,225	100	14,858	100	19,023	100	18,124	100	77

Table 2.1 Knee replacements in Canada by type of surgery, 2002-2006 [5]

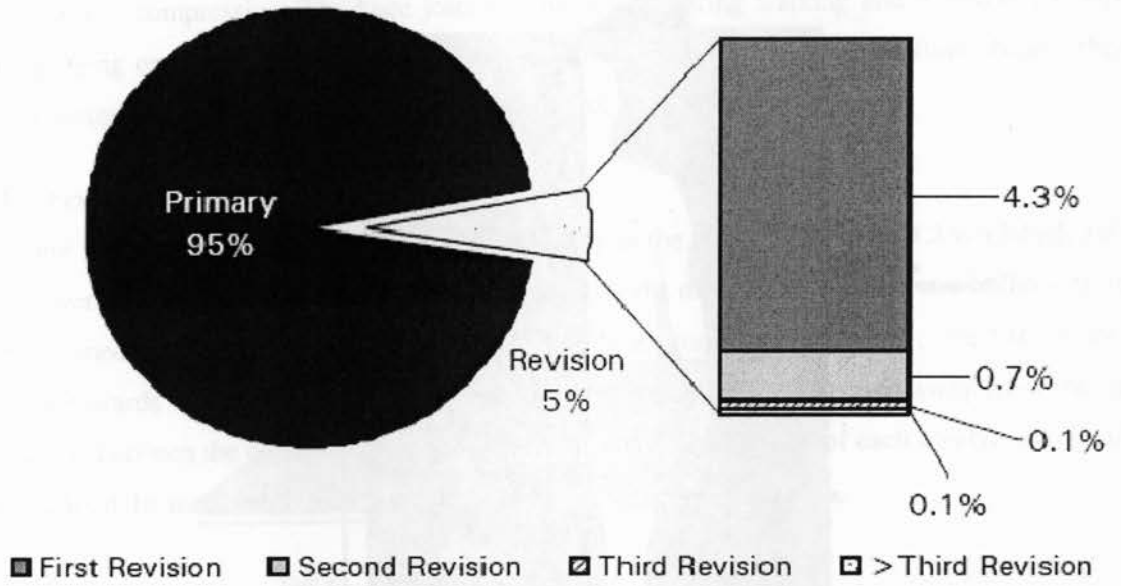

Figure 2.2 Chart of primary surgeries compared to revisions, 2005-2006 [5]

The numbers in Table 2.1 indicate that primary and revision surgeries have generally increased since 2002-2003. The Canadian Joint Replacement Registry states that increase in revision surgeries is driven by the annual increase in primary knee replacements [5]. The trend in primary knee replacement procedures and the subsequent increase in revision surgeries indicate that this procedure will continue to remain a popular treatment for knee joint arthritis. While knee prostheses have improved greatly since the 1960s [3, 43-46], there are areas where advances need to be made, e.g. stress-shielding and bone resorption (discussed further in Section 4.3.1, p.28) .

3 THE HUMAN KNEE

3.1 Anatomy

3.1.1 Co-ordinate planes

The human body may be divided into three major planes, as shown in Figure 3.1. The *sagittal plane* divides the bi-symmetric human body into right and left halves. The *coronal plane*, alternatively called the *frontal plane*, divides the body into anterior and posterior sections. The *transverse plane*, or the *axial plane*, divides the body into superior (upper) and inferior (lower) halves. Figure 3.1 displays the planes, and the terminology used to describe directions along the body planes [47, 48].

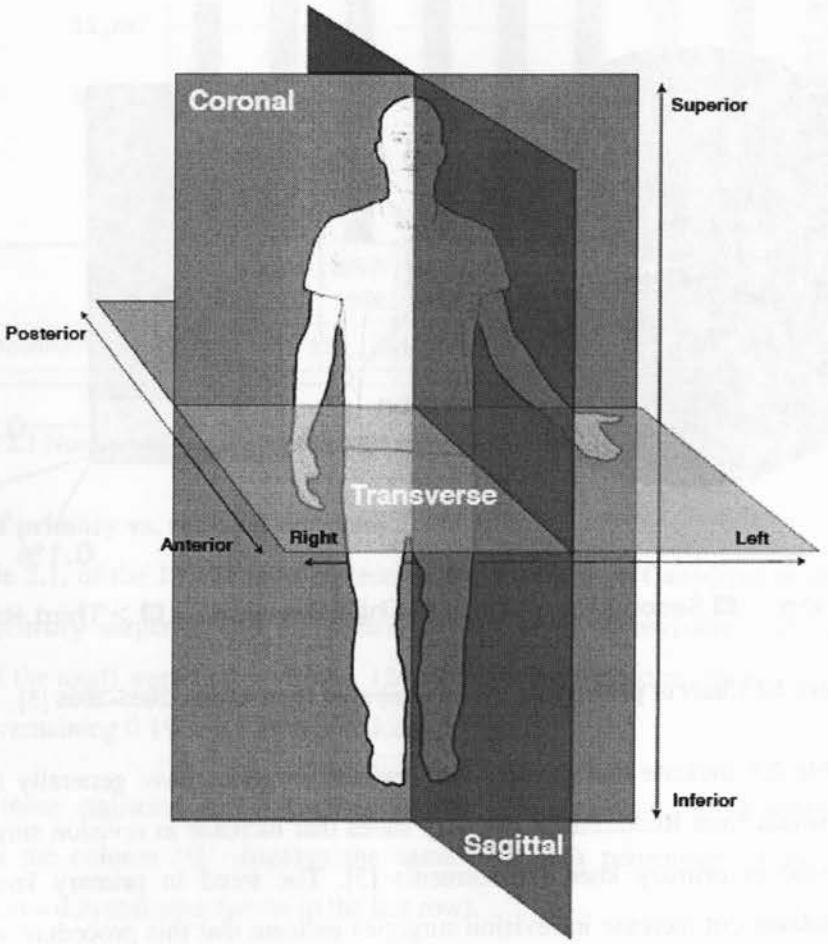

Figure 3.1 Anatomical planes of reference [47]

3.1.2 Joints

Based on the range of motion, three functional categories of joints exist in the human body. An immovable joint is a *synarthrosis*, a slightly movable joint is an *amphiarthrosis*, and a freely movable joint is a *diarthrosis* (or a synovial joint). The knee joint is a synovial joint. Synovial joints are specialised for movement, permitting a wide range of motion. In healthy conditions, the bony surfaces within a synovial joint do not contact one another because those surfaces are covered by a softer tissue called articular cartilage. The articular cartilage reduces friction and also acts as a shock absorber [48].

In synovial joints like the knee, a *synovial membrane* lines the joint cavity in locations where the articular cartilage is absent. Synovial membranes produce the *synovial fluid* that fills in the joint cavity. This fluid also acts to provide lubrication, and is reported to reduce friction between cartilage surfaces in a joint to around one-fifth of that between two cubes of ice. The synovial fluid also cushions shocks when the joint is subjected to compression. The knee joint is compressed during walking and is severely compressed during jogging or running. When the pressure suddenly increases, the synovial fluid absorbs the shock and distributes it evenly across the articular surfaces [48].

3.1.3 Femur

The femur is a bone of the upper leg, known commonly as the thighbone. Figure 3.2 is a labelled diagram of the lower extremity, or the distal end, of the femur. At the distal end, there are two bulbous features of bone, the medial and lateral *condyles* of the femur. In anatomical terminology, 'medial' refers to the direction towards the midline of the body, and 'lateral' refers to the direction away from the midline. Posteriorly, between the condyles is the *intercondular notch*. On the side of each condyle is a small bony 'bump' called the medial or lateral *epicondyle* [49].

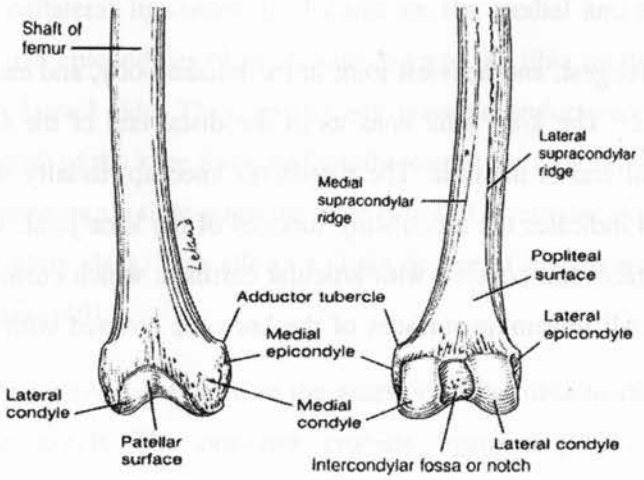

Figure 3.2 Distal end of the femur. Anterior view (left), Posterior view (right) [49]

3.1.4 Tibia and Fibula

The tibia and the fibula are bones of the lower leg. Figure 3.3 is a labelled diagram of the upper extremity, or proximal end, of the tibia and fibula. The tibia is commonly known as the shinbone. The tibia is the larger of the two bones and is the primary weight-bearing bone of the lower leg [49]. Only the tibia is functionally attached to the knee joint. Figure 3.3 is a diagram of the upper portion of the tibia, with parts relevant to the knee joint labelled.

At the proximal end of the tibia (i.e. the knee joint end), two large features of the bone are named the *medial condyle* and the *lateral condyle* (see Figure 3.3). Also indicated are the articular surfaces on the tibia that cover the condyles. Between the condyles exists a protrusion called the *intercondular eminence* [49].

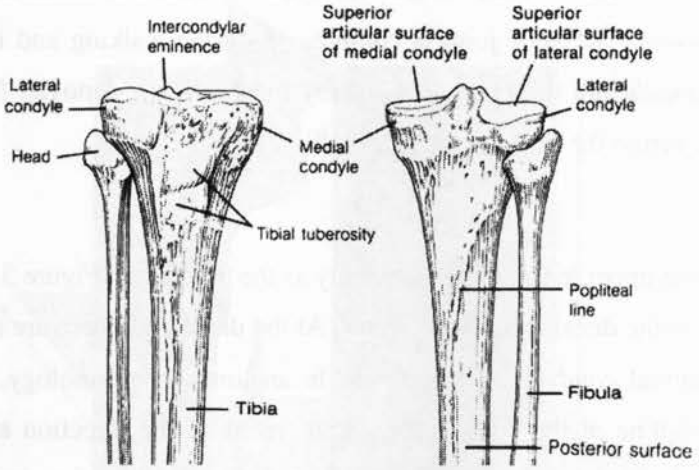

Figure 3.3 Proximal end of the tibia. Anterior view (left), Posterior view (right) [49]

3.1.5 The knee joint

The knee is the largest, strongest, and heaviest joint in the human body, and each knee supports almost half the body's weight [32]. The knee joint consists of the distal end of the femur, which rotates (or articulates) on the proximal end of the tibia. The patella (or kneecap) usually slides on a groove at the femur end [50]. Figure 3.4 indicates the articulating surfaces of the knee joint. Where these three bones come in contact, their surfaces are covered with articular cartilage which cushions the bones to enable smooth joint movements. All remaining surfaces of the knee are covered with the synovial membrane [50].

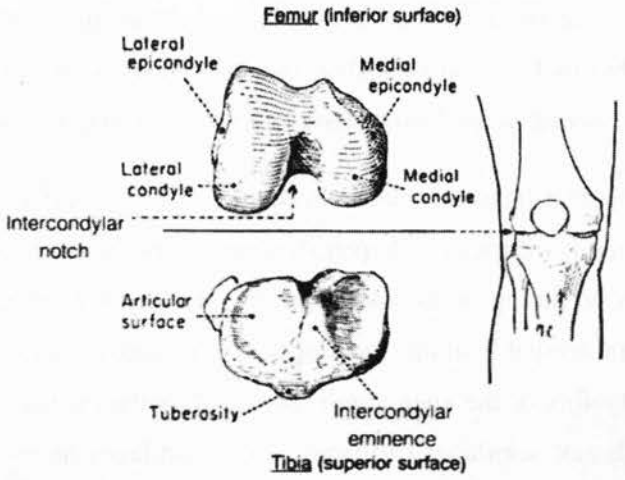

Figure 3.4 Articulating surfaces of the knee joint [49]

The convex condyles of the femur sit in the concave superior articulating surfaces of the tibia. The intercondular eminence of the tibia partially protrudes up into the intercondular notch of the femur, but it leaves considerable space for the internal ligaments of the knee to pass through the notch. The patella, or kneecap, is encased in the tendons of the quadriceps muscle and is located anterior to the knee joint, fitting into the patellar surface (labelled in Figure 3.2) of the femur. Strictly speaking, the patella is not part of the true knee joint, but rather an anterior bony protection for the tissue within the knee joint. The stability of the knee joint and the primary restrictions of the actions are provided by the complex structure of ligaments in the knee [49].

3.1.6 Supports and stabilisers

Six major ligaments support the knee joint – two *collateral* ligaments, two *cruciate* ligaments, and two *popliteal* ligaments. The collateral ligaments are located on the medial and lateral sides of the knee, running from their respective epicondyles of the femur down to the tibia on the medial side, and to the head of the fibula on the lateral side. They restrict any possible abduction (outward movement) and adduction (inward movement) of the knee joint, and totally restrict the rotation of the knee in an extended position. The collateral ligaments are tight when the knee is in full extension. When the knee is flexed, the collateral ligaments are slightly slack. This allows a slight degree of inward and outward rotation of the knee joint in a flexed position [49].

The anterior cruciate ligament (ACL) runs from the anterior of the tibia to the posterior of the femur, through the intercondular notch. The posterior cruciate ligament (PCL) also goes through the intercondular notch, running from the posterior of the tibia to the anterior of the femur. The two cruciate ligaments primarily restrict the anterior-posterior sliding of the knee joint. In effect, the cruciate ligaments

prevent the femur from sliding off the tibia. In addition, the cruciate ligaments also contribute to restricting knee rotation. The cruciate ligaments take over the restriction of rotation where the collateral ligaments leave off, thereby serving as the final restrictors of knee rotation in a flexed position [49].

The oblique and arcuate popliteal ligaments run from the posterior of the femur to the posterior of the tibia. These ligaments primarily restrict the hyperextension of the knee. They also contribute to the restriction of anterior-posterior sliding of the knee joint. In summary, the ligaments of the knee restrict abduction, adduction, lateral-medial sliding, anterior-posterior sliding, hyperextension, and rotation during extension. Further stability of the knee joint is provided by the medial and lateral *meniscus*, also known as the medial and lateral semilunar cartilages. These cartilages lie on the superior articulating surfaces of the tibia and are attached to the tibia. They act to deepen the indentation into which the condyles of the femur fit. The menisci serve as shock-absorbing cushions for the knee joint and also increase the stability of the joint [49].

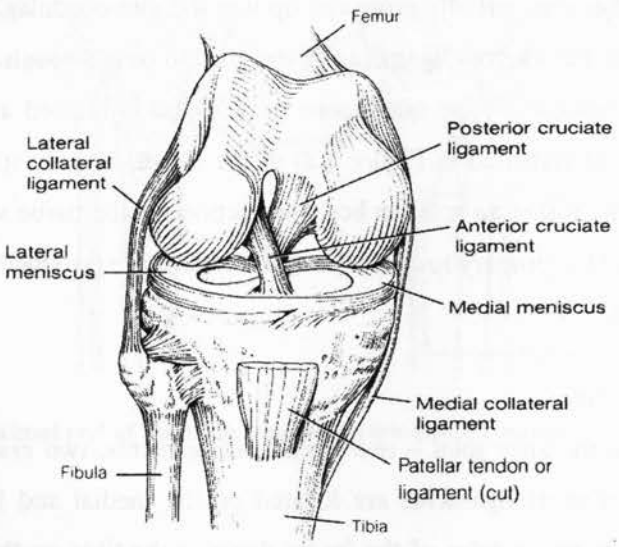

Figure 3.5 Ligaments of the knee joint [49]

3.2 Joint diseases

Osteoarthritis, rheumatoid (inflammatory) arthritis, and post-traumatic arthritis are the most common causes of chronic knee pain and loss of knee function. Osteoarthritis is the most common form of arthritis, usually occurring after middle age [51]. It is marked by a chronic breakdown of cartilage in the joints, which causes the bones to rub against one another, leading to pain, stiffness, and swelling. Rheumatoid arthritis is a condition where the synovial membrane thickens and inflames, secreting too much synovial fluid into the joint space. Chronic inflammation of the synovial membrane can lead to a loss of articular

cartilage, and subsequently loss of joint function. Post-traumatic arthritis, as the name suggests, is inflammation of a joint caused by physical injuries. As the knee degenerates due to arthritis, the individual's leg may develop varus deformities, whereby the knee bends outwards (bowlegged) or inwards (knock-kneed) respectively. These deformities contribute to much pain, and gradual functional loss of the knee [50].

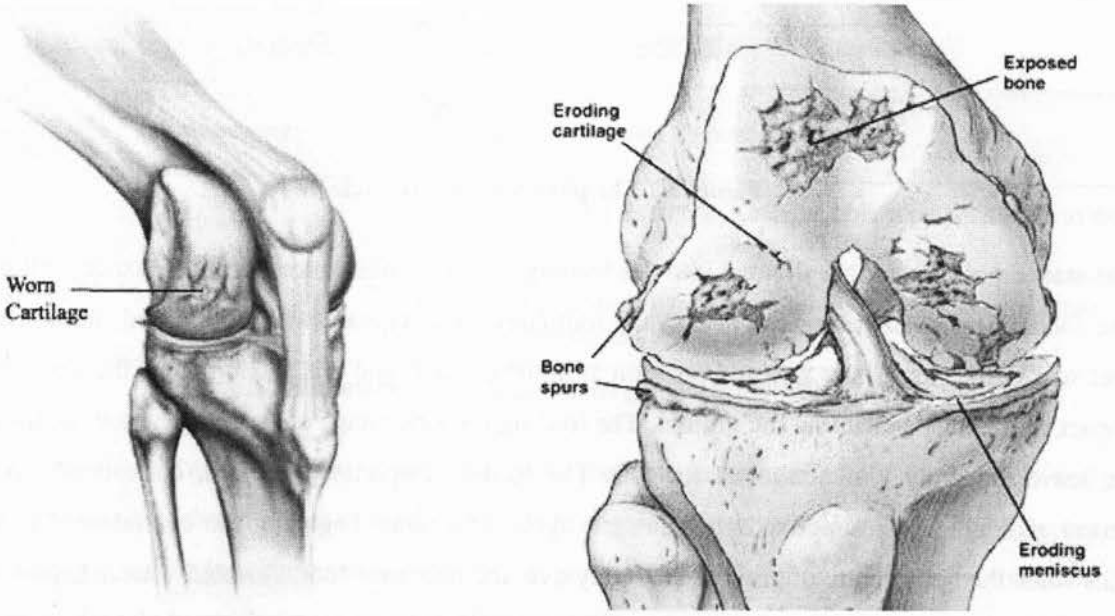

Figure 3.6 Wear of cartilage in the femoral condyle; [52] **(left),** [53] **(right)**

3.3 Biomechanics

3.3.1 The gait cycle

The knee joint is an integral mechanism for everyday tasks such as walking, climbing stairs, jumping, etc. Each type of activity produces a unique biomechanical load pattern on the knee joint. The most common, and therefore the most important activity is simple level walking. Walking is a product of repeated cycles of gait, where one gait cycle is understood to begin when one foot contacts the ground until the same foot contacts the ground again [54]. By multiplying an average number of daily steps by 365 days, Seedhom and Wallbridge [55] estimate that the average adult takes some 0.9-1.5 million steps annually. Researchers have studied gait by separating it into two primary phases – the *stance* phase which is approximately 60% of the gait cycle, and the *swing* phase which constitutes the remaining 40% [56].

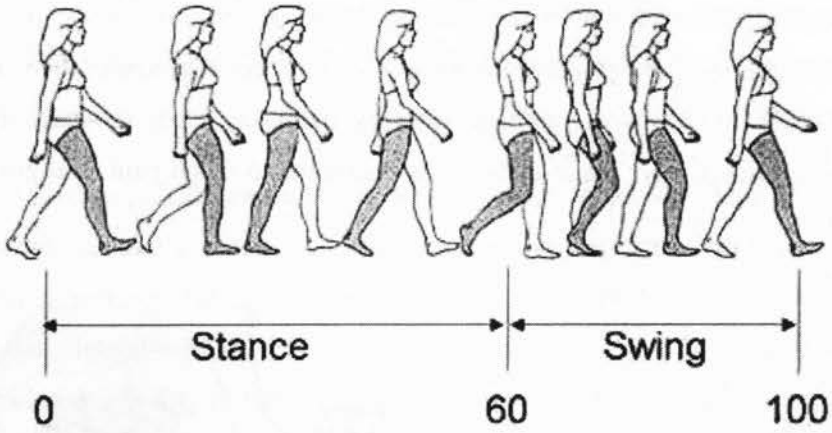

Figure 3.7 The phases of the gait cycle [57]

The stance phase is further divided into the loading response, midstance, terminal stance, and preswing. The *loading response* begins the instant the foot comes into contact with the ground (initial contact, or heel strike). The knee is in a flexed position at initial contact, and this flexion helps the knee absorb the impact of the heel contacting the ground. The loading response stage ends when the toes of the opposite leg leave the ground (contralateral toe-off). The loading response, therefore, corresponds to the first period of double limp support during the gait cycle. *Midstance* begins at the contralateral toe-off, and ends when the body centre of gravity is directly over the reference foot. *Terminal stance* begins when the centre of gravity is over the reference foot, and ends when the foot of the other leg contacts the ground (contralateral initial contact). This initiates the *weight loading* on the leg. During the terminal stance, after weight loading at around 35% of the gait cycle, the heel of the reference foot rises from the ground. Note that the weight loading period of the reference leg corresponds with the weight unloading period of the opposite leg. *Preswing* begins at the contralateral initial contact, and ends when the toes of the reference leg leave the ground (toe-off) [54, 56, 58].

The swing phase is further divided into the intitial swing, midswing, and terminal swing. The *initial swing* stage begins at toe-off, and continues until the reference knee reaches a maximum flexion of around 60 degrees. *Midswing* lasts from the maximum knee flexion to until the tibia is perpendicular to the ground. *Terminal swing* begins when the tibia is perpendicular to the ground and ends at initial contact, at which point the gait cycle resumes again. The knee reaches its maximum extension just before initial contact[54, 56, 58].

Gait Cycle	Stance phase 0-60%	Loading response 0-10%	Initial contact to contralateral toe-off
		Midstance	Contralateral toe-off to when the body CG is directly above the reference foot; weight loading begins
		Terminal stance	CG directly above the reference foot to contralateral initial contact; weight loading ends and heel of the reference foot leaves ground at ~35%
		Preswing 50-60%	Contralateral initial contact to toe-off
	Swing phase 60-40%	Initial swing	Toe-off to maximum knee flexion
		Midswing	From maximum knee flexion to when the tibia is perpendicular to the ground
		Terminal swing	Tibia perpendicular to the ground until initial contact; knee reaches maximum extension just before initial contact

Table 3.1 Summary of the stages in the gait cycle [54, 56]

The normal knee flexes two times during the gait cycle, the first to approximately 15 degrees, and a second time reaching a midswing peak of 60-65 degrees. In comparison to normal walking, the maximum stance-phase flexion during jogging reaches 44.3 ± 5.2 degrees [59]. While climbing up stairs, this is 66.7 ± 5.8 degrees, and while going down stairs it is 63.9 degrees. The mean range of knee motion during level walking is estimated to be 61 degrees. The mean range of knee motion during stair ascent and descent is 96 degrees [59].

3.3.2 Motion of the knee joint

The knee is conventionally considered to be a hinge, though some rotation occurs during flexion-extension. In principle, movement of the knee joint has 6 degrees of freedom – 3 translations that include anterior-posterior, medial-lateral, and inferior-superior; and 3 rotations that include flexion-extension, internal-external, and abduction-adduction. The primary motion is rotation that occurs in the sagittal plane and ranges from 0 to 140 degrees. During the gait cycle, the knee reaches a maximum flexion of around 65 degrees during the toe-off phase. Movements of the knee joint are guided by the shapes of the joint surfaces and by the orientation of the ligaments involved in the knee joint. Since the knee joint is located between the two longest lever arms of the body (the upper and lower leg), the effect of the cruciate and collateral ligaments is extremely important in stabilising the joint under considerable forces and cyclic loading [2, 59].

When all the constraints in the knee joint are taken into account, two primary actions and one secondary action remain. The possible actions of the knee are flexion, extension, and slight rotation when the knee is being flexed. Some individuals may have a longer popliteal ligament, and this condition allows for slight hyperextensions of the knee joint – but this is not possible in all individuals. In the analysis of the knee joint action, there is only one position of extension and an infinite number of positions for flexion, and slight rotation towards the end of full extension [49].

As mentioned in Section 3.1.6 (p.10), the cruciate and the collateral ligaments stabilise the knee. While the cruciate ligaments stabilise the joint in the anterior-posterior (or forward-backward) orientation, the collateral ligaments provide medial-lateral (or side-to-side) stability. The medial collateral ligament primarily restrains the valgus rotation (inward movement of the proximal tibia in the coronal plane) of the knee joint. The lateral collateral ligament primarily restrains varus rotation (outward movement of the proximal tibia in the coronal plane) of the knee joint. More can be written to detail the motion of the knee joint, but further detail is irrelevant to the scope of this thesis, which is mainly concerned with static analyses on the knee joint.

3.3.3 Relevant structural loads

There are historical studies of biomechanics of human walking and the study of hip joint forces performed by Eberhart *et al.* [60] (as reported by Andriacchi and Alexander [61]), Pauwels [62], and Rasch [63, 64] (as reported by Paul [65]); and more recent studies as those of Winter [66], Sutherland *et al.* [67], and Andriacchi and Alexander [61]. During normal gait, the knee joint experiences compressive loads that are between 2 and 4 times the body weight [65, 68, 69]. This range is the basis of a variety of studies conducted on knee prostheses. Around 1970, Paul [69] noted that the forces transmitted by the knee joint "exceeds the body weight", without quoting any numbers. Morrison [68] estimated that the total force transmitted by the knee joint during level walking is 2-4 times the body weight. Bartel *et al.* [2] recommend using 3-4 times the body weight to simulate tibiofemoral contact force when designing total knee replacements.

Denham and Bishop [70] state that during regular knee function the resulting forces transmitted through the joint are so balanced that force transmission in the femur is largely axial, while bending moments and shearing forces are small. The investigations by Paul [71] indicate that the joint force in the knee during regular, unhurried gait peaks just under 3 times the body weight at around 50% of the gait cycle, as shown in Figure 3.8. Figure 3.9 plots the tibiofemoral joint force in the knee during slow, normal, and fast level walking at 1.01, 1.48, and 2.01 m/s respectively. During slow and normal gait, the maximum compressive force in the knee joint is 2.5 and 3 times the body weight respectively, occurring at around 50% of the

cycle. Interestingly, during fast gait (2.01 m/s), the maximum compressive joint force occurs at around 15% of the gait cycle, peaking at nearly 4 times the body weight. Table 3.2 shows the results reported by Paul [71] on the compressive forces transmitted through the knee joint during various activities.

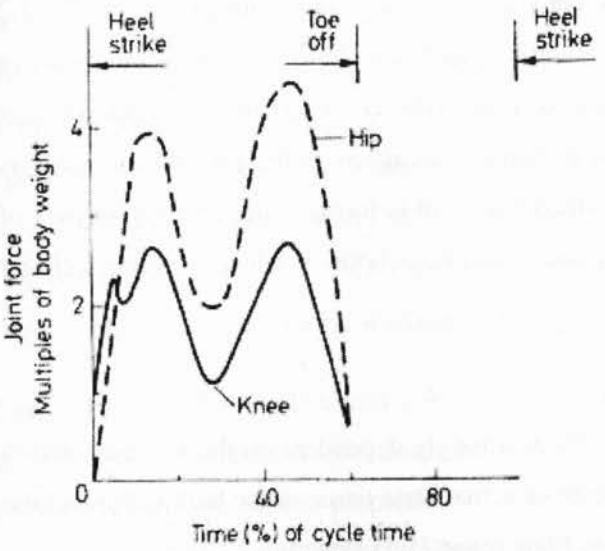

Figure 3.8 Knee joint compressive force during normal, level gait from Paul [71]

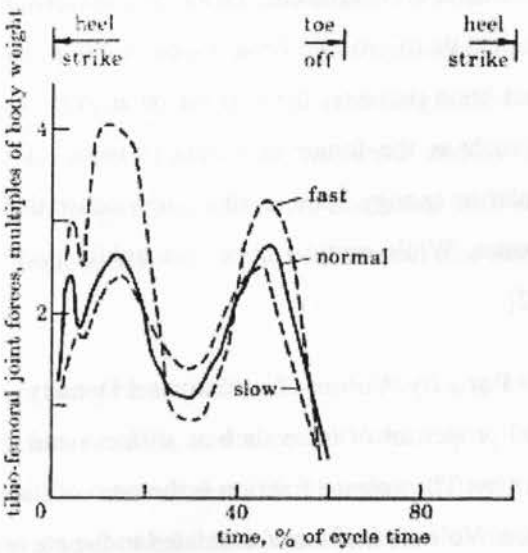

Figure 3.9 Knee joint forces during slow (1.10 m/s), normal (1.48 m/s), and fast (2.01 m/s) level walking from Paul [65]

Activity	Peak compressive force (× Body weight)
Level walking at 1 m/s	2.7
Level walking at 1.5 m/s	2.8
Level quick walking at 2 m/s	4.3
Stairs up	4.4
Stairs down	4.9
Ramp up	3.7
Ramp down	4.4

Table 3.2 Joint force during various activities as per Paul [71]

3.4 Bone as an engineering structure

From an engineering perspective, the bone is an extraordinary material having unique material properties, the ability to repair itself, and the ability to adapt to its mechanical environment by biological remodelling and turnover. On a weight basis, bone is around 60% inorganic, 30% organic, and 10% water. The respective volume fractions are 40%, 35%, and 25%. The inorganic phase of bone is a ceramic crystalline

material, which is an impure form of naturally occurring calcium phosphate called hydroxyapatite; $Ca_{10}(PO_4)_6(OH)_2$. The inorganic phase of bone consists primarily of type I collagen (90% weight fraction), other minor collagen of types III and VI, and a variety of non-collagen proteins [2, 37].

Bone tissue is a hierarchical, anisotropic composite at many levels. At the highest hierarchical level (1-2 mm scale), there are two basic types of bone tissue – cortical, and cancellous bone. *Cortical* bone, or compact bone tissue, is the densest bone in the skeletal structure. The central shaft (diaphysis) of long bones such as the femur and tibia is made of cortical bone. *Cancellous* bone, otherwise known as trabecular or spongy bone, is much less dense than cortical bone and is found at the ends (epiphysis) of long bones. While cortical bone is a tightly packed tissue, cancellous bone is a highly porous cellular solid [2].

3.4.1 Porosity, Volume fraction, and Density

Material properties of bone such as stiffness and strength are strongly dependent on the volume fraction and density. The volume fraction is the ratio of the volume of actual bone tissue to the bulk volume of the specimen. Volume fraction V_f is related to the porosity of bone tissue P via Equation 3.1.

$$V_f = 1 - \frac{P}{100}$$ **Equation 3.1** [2]

Cortical bone has a porosity of less than 30%, or equivalently a volume fraction of about 0.70. Cancellous bone rarely has a volume fraction greater than 0.60. Age is a major influence on the porosities of bone tissue. Cortical bone can vary from a porosity of 5% at age 20 up to nearly 30% at age 80. Cancellous bone may vary from 50% porosity in the young adult proximal femur to about 95% in the elderly vertebra [2].

A variety of measures are used to describe bone density, but the most common measures are tissue density and apparent density. Tissue density ρ_{tiss} is the ratio of tissue mass to volume of the actual bone tissue, not including any porosity. Apparent density ρ_{app} is the ratio of tissue mass to the bulk volume of the specimen, including vascular porosity. Tissue density, apparent density and volume fraction are related as shown by Equation 3.2.

$$\rho_{app} = \rho_{tiss} V_f$$ **Equation 3.2** [2]

For hydrated bone, tissue density is the same for cortical and cancellous bone at around 2.0 g/cc. Ruff and Hayes [72, 73] have shown that the apparent density of hydrated human cortical bone is about 1.85 g/cc, and does not vary significantly from site to site. The average apparent density of cancellous bone depends

heavily on anatomical location. In the human tibia, the apparent density is about 0.30 g/cc, and in the load bearing portions of the proximal femur it is about 0.50 g/cc [2].

3.4.2 Cortical bone

Cortical (compact) bone can be generally assumed to be transversely isotropic in humans. This means that cortical bone material has one primary axis in the longitudinal direction, and is isotropic in the plane perpendicular to the longitudinal axis (the transverse plane). As per Bartel *et al.* [2], the longitudinal axis is generally aligned along the shaft (the diaphyseal axis) of long bones like the femur and or tibia. Cortical bone is both stronger and stiffer when loaded in the longitudinal direction, compared with radial or circumferential directions. Such a structure enables the leg bones to resist uniaxial stresses that develop along the diaphyseal axis during walking and running [2].

Work done by Reilly and Burstein [74, 75] show that five independent material constants (Longitudinal and transeverse modulus, longitudinal and transverse Poisson's ratio, and shear modulus) describe the transversely isotropic elastic properties of cortical tissue. The mean values of all human femoral bone samples tested are listed in Table 3.3. Reilly and Burstein also showed that cortical bone has asymmetric strengths – it is stronger in compression than tension for each principal material direction, as shown in Table 3.4. The strength to modulus ratio for cortical bone is around 0.0113 for longitudinal compression, and 0.0078 for longitudinal tension. Compared to high performance engineering metal alloys such as Aluminium-6061-T6 (corresponding ratio is 0.0045) and Titanium-6Al-4V (0.0073), cortical bone proves to be a high-performance material in compression [2].

Cortical elastic properties	Number of specimens	Mean values
Longitudinal elastic modulus	170	17 GPa
Transverse elastic modulus	31	11.5 GPa
Shear modulus	166	3.28 GPa
Poisson's ratio, longitudinal	147	0.46
Poisson's ratio, transverse	26	0.58

Table 3.3 Mean anisotropic elastic properties of femoral cortical bone by Reilly and Burstein [75]

Cortical ultimate strengths		Mean values (MPa)
Ultimate longitudinal stress	Tension	133
	Compression	193
Ultimate transverse stress	Tension	51
	Compression	133
Ultimate shear stress	Torsion	68

Table 3.4 Mean anisotropic ultimate properties of femoral cortical bone by Reilly and Burstein [75]

It must be kept in mind that bone is still essentially a heterogeneous structure due to variations in microstructural parameters such as porosity. Research has shown that the different moduli and strengths of cortical tissue is dependent on the bone density through linear or power law relations [76]. But in the case of bone-implant stress analysis, it is often appropriate to assume average properties for cortical bone, such as those reproduced in Table 3.3 and Table 3.4. As Bartel *et al.* [2] observe, since the modulus of metallic implants is much greater than that of cortical bone, ±20% variations in the modulus of cortical bone will not substantially affect stem stress calculations.

It must also be noted that cortical bone may exhibit some viscoplastic behaviour under low stress loads [77] as well as viscoelastic properties at higher stresses [78] (since its modulus and strength increase as the rate of loading is increased). Fondrk *et al.* [77] showed the viscoplastic behaviour over time through a multiple load constant stress creep test (stepwise increase in constant loads). Figure 3.10 shows the increase in creep rate as the magnitude of stress is increased (denoted by labels 1-7). McElhaney [78] showed the strain rate sensitivity of cortical bone under longitudinal tensile loading. However, the effect is not considered substantial, since over a six-order-of-magnitude increase in strain rate, the modulus changes only two-fold, and strength by a factor of three (See Figure 3.11). Also, as far as the majority of physiological activity is concerned, they tend to occur in a relatively narrow range of strain rates (0.01-1.0/sec) [2]. Cortical bone, therefore, can be reasonably assumed to behave elastically for physiologic stress tests.

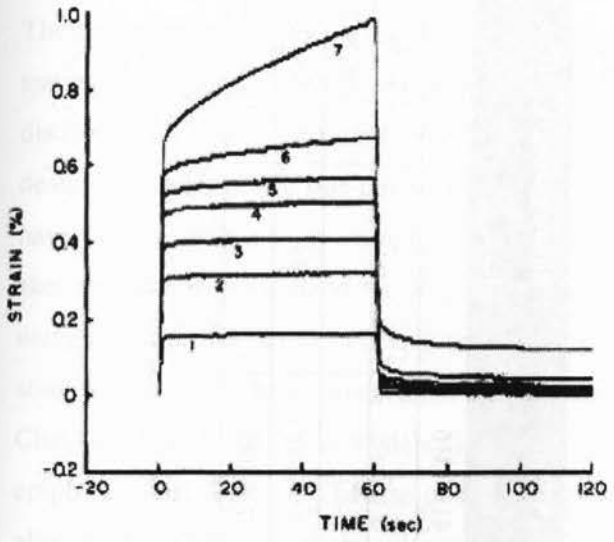

Figure 3.10 Viscoplastic behaviour of cortical bone [77]

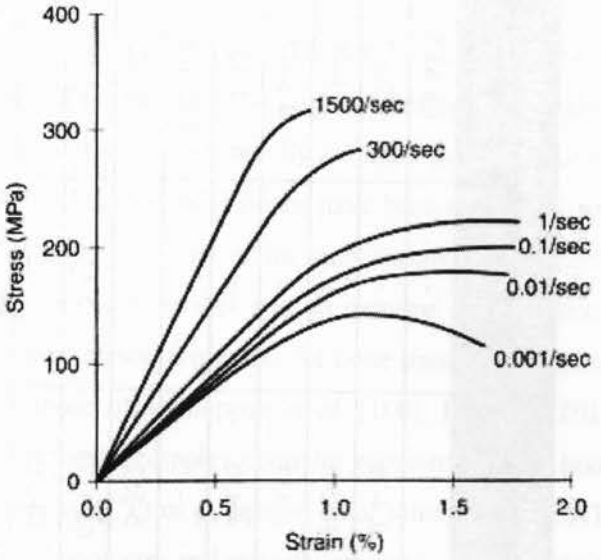

Figure 3.11 Viscoelastic behaviour in cortical tissue shown by strain rate sensitivity [78]

3.4.3 Cancellous bone

Cancellous (trabecular) bone is a highly heterogeneous material, and its properties and density varies depending on location in the human body [79-81]. Many investigators have catalogued the distribution of cancellous bone properties from multiple locations in the human skeleton [79, 82, 83] (see Table 3.5 and Table 3.6). The anisotropy and tremendous variation in properties have been attributed to the tendency of cancellous bone to adapt and remodel according to its function as per Wolff's Law [84-87]. The large variation in apparent density makes it difficult to obtain general values for mechanical properties, as shown in Table 3.5 and Table 3.6. Consequently, analysis of structural problems is more difficult than that of cortical bone. However, as in the case of cortical tissue, the required accuracy of the properties depends on the precision of the expected analysis – e.g. Bartel *et al.* [2] observe that "a two-fold variation in trabecular modulus from 200 to 400 MPa may have little effect on calculated stem stresses in a bone implant system". Nevertheless, it must be understood that there are significant differences in cancellous tissue properties across skeletal regions – as displayed clearly in Table 3.5 and Table 3.6.

Study	Year	Apparent density (g/cc)		Elastic Modulus (MPa)		Ultimate strength (MPa)	
		Mean	Range	Mean	Range	Mean	Range
Behrens *et al.* [88]	1974	-	-	-	-	-	1.8-63.6
Lindahl [89]	1976	-	-	-	1.4-79	-	0.2-6.7
Carter and Hayes [90]	1977	-	-	-	10-500	-	1.5-45
Williams and Lewis [91]	1982	-	-	-	8-457	-	1.5-6.7
Goldstein *et al.* [82]	1983	-	-	-	4-430	-	1-13
Hvid and Hansen [92]	1985	-	-	-	-	-	13.8-116.4
Ciarelli *et al.* [93]	1986	-	-	-	5-552	-	0.52-11
Linde *et al.* [94]	1989	0.29	0.09-0.66	445	61-1174	5.33	0.68-14.1
Ashman *et al.* [95]	1989	0.26	0.13-0.75	1107	340-3350	-	-

Table 3.5 Proximal tibia cancellous bone properties

Study	Year	Apparent density (g/cc)		Elastic Modulus (MPa)		Ultimate strength (MPa)	
		Mean	Range	Mean	Range	Mean	Range
Pugh *et al.* [96]	1973	-	-	-	413-1516	-	-
Behrens *et al.* [88]	1974	-	-	-	-	-	2.25-66.2
Ducheyene *et al.* [97]	1977	-	-	-	-	-	0.98-22.5
Rohlmann *et al.* [98]	1980	0.50	0.14-1.00	389	44-1531	7.36	0.56-22.9
Ciarelli *et al.* [93]	1986	-	-	-	7.6-800	-	0.56-18.6

Table 3.6 Distal femur cancellous bone properties

3.5 Synthetic bone models

The performance of orthopaedic implants, such as those used in TKA and THA, may be studied by either testing them on cadaveric bones or using finite element (FE) models. The goal most often is to analyse distributions of stress and strain in the implant and in bone tissue to eventually facilitate the design or re-design of implants. For this purpose, attempts to develop FE models of bones have been numerous, and have become increasingly complex. Brekelmans *et al.* [99] were one of the first researchers to model skeletal parts to understand the stresses experienced. This early model was an extreme simplification, using two dimensional models and homogenous, isotropic, elastic properties for bone tissue. Subsequent studies have used three dimensional models, such as those of Valliappan *et al.* [100], Huiskes [101], Cheal *et al.* [102], but these models did not fully account for the complex condylar geometry of long bone epiphyses (end regions). The rise of computed tomography (CT) or computed axial tomography (CAT) allowed the use of more representative models in terms of geometry and material properties, such as those developed by Cheal *et al.* [103], McNamara *et al.* [104], Taylor *et al.* [105], Bougherara *et al.* [42], Zdero *et al.* [106], to name a few. These studies have used full bone models that treat the overall structure as a continuum, thereby ignoring the diversity in the microstructure of the bone. Regardless, these approaches are useful in designing implants where the comparative, rather than the absolute, values of stresses are required – e.g. in determining the load-sharing between an implant and the surrounding bone.

It is difficult to validate FE models against the same cadaveric specimens over time, due to problems with storage, hydration and degradation of skeletal tissue. Papini *et al.* [107] note that using *in vitro* cadaveric specimens to validate FE models introduce a specimen-specific bias, leading to results that cannot always be reproduced or considered universally acceptable. Also, in addition to the broad differences in cadaveric bone quality, the abundance of testing and storage technique makes it inconvenient to match or collate data generated from research worldwide. In view of these challenges in establishing a consistent 'reference bone' specimen, synthetic bone has proved to be a significantly useful alternative. These composite analogue models are valuable tools for the consistent analysis of implant performance, both in equilibrium and in fatigue testing [108, 109]. Cristofolini *et al.* [110] indicate that the advantages of composite analogue bones over cadaveric bones are the negligible inter-specimen variability, ready availability, and ease of storage.

The first anatomically realistic analogue bone model was produced in 1987 by Pacific Research Laboratories (Vashon, WA, USA) [110, 111]. This first generation of composite models modelled cortical bone using carbon-fibre reinforced epoxy, and cancellous bone using polyurethane foam. The second generation of composite bones introduced in 1991 had improved cortical layers made of fibreglass fabric reinforced epoxy. A third generation of composite bone was released in 1998 to improve anatomical

details on the bone and simplify the fabrication process. With cortical layers manufactured using short glass fibre reinforced epoxy, these third generation models were shown to be reasonable approximations of structural stiffness in natural bone by Heiner and Brown [112]. Geometric and static mechanical characteristics were validated and shown to fall within the range of human cadaveric specimens [110-114]. However, fatigue resistance of the third generation models was shown to be insufficient for some types of cyclic testing [108]. Fourth generation models were released in 2007 that still used short glass fibre reinforced epoxy for cortical material, but provided better fracture and fatigue resistance [108]. Chong *et al.* [108, 109] showed that, in addition to realistic compressive properties, the fourth generation model showed a tensile yield modulus, ultimate tensile strength, fracture toughness, and fatigue crack propagation that were closer to literature values for fresh-frozen cortical bone than the third generation models. Also, the tensile modulus did not significantly change between 25°C (room temperature) and 37°C (body temperature), which was not the case for the third generation models.

3.5.1 Synthetic models used in this study

The experimental work in this study was conducted using a fourth generation femur specimen (model #3403, Sawbones Worldwide, Pacific Research Laboratories, Vashon, WA, USA) [111], which was replicated in geometry modelling to develop the FE model. by. The femur model was eventually scanned using Mimics® Medical Imaging Software (The Materialise Group, Leuven, Belgium) and imported into SolidWorks 2008 (SolidWorks Corp., Dassault Systèmes Concord, MA, USA) to generate the geometry used to develop the FE model, as discussed in Chapter 7 (p.66). The femur used is a 'medium' left-knee model. The image of the synthetic femur is shown in Figure 3.12. Table 3.7 lists the dimensions of the model.

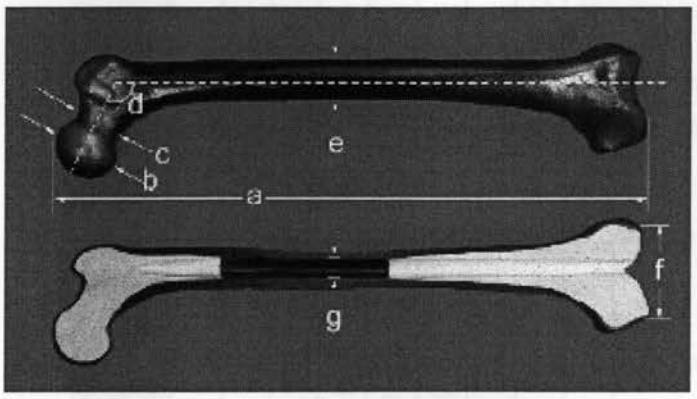

Figure 3.12 Fourth generation, medium, left femur [115]

Labels	Dimensions (mm)
a	455
b	45
c	31
d	135
e	27
f	74
g (canal)	13

Table 3.7 Dimensions of the fourth generation femur model [115]

As mentioned earlier, the fourth generation models are made of short glass fibre reinforced epoxy (cortical regions) and solid rigid polyurethane foam (cancellous regions). The composite material

properties are isotropic, as published by the manufacturer (given in Table 3.8). The manufacturer reports that the tensile and compressive properties of simulated cortical bone were tested as per American Society for Testing and Materials (ASTM) standards D638 and D695, respectively [111]. The simulated cancellous bone material was tested as per ASTM D1621 [111].

	Density (g/cc)	Compressive (MPa)		Tensile (MPa)	
		Strength	Modulus	Strength	Modulus
Simulated cortical bone	1.64	157	16,700	106	16,000
Simulated cancellous bone	0.27	6.0	155	n/a	n/a

Table 3.8 Isotropic properties of simulated bone [111]

4 KNEE ARTHROPLASTY

Knee arthroplasty, or knee replacement procedures, are meant to relieve arthritis pain, and restore joint function by replacing the contact surfaces of the knee joint. Usually cartilage and bone are removed and replaced by metals or synthetic materials. Typical knee implants, or *prostheses*, that replace the entire knee joint consist of a femoral and a tibial component, and may involve resurfacing of the patella. The following section provides an overview of the development of knee replacement surgery and implant design.

4.1 Reviewing the history

Insall and Clarke [4] report that the first surgeries performed to improve joint function in the knees were conducted circa 1860 by A. Verneuil. To lubricate the joints, these 'interposition' surgeries made use of a variety of materials including skin, muscle, fat and even pig bladder inserted into the joint space. The results were "disappointing" [4]. In the same year, Ferguson [116] resected the entire knee joint to treat knees damaged by deformity, tuberculosis, or other infectious diseases. The results of such procedures were sufficiently poor to dissuade anything more than occassional attempts under severe cases [4]. As reported by Campbell [117], the first artificial implants appeared in the 1940s as moulds fitted to the femoral condyles. This was followed by tibial implants in the next decade, but both designs were susceptible to loosening causing persistent pain in patients.

Combined femoral and tibial implants replacing the articular surfaces were first introduced between the late 1940s and 1960s [3, 118], the first of which was the design by McKeever [119]. In the 1960s, knee arthroplasty began in Boston with the 'MGH mould femoral hemiarthroplasty' pioneered at the Massachusetts General Hospital, and the McKeever metallic tibial hemiarthroplasty pioneered at the Robert Breck Brigham Hospital (now Brigham and Women's Hospital) [44]. Hemiarthroplasty is a surgical procedure that replaces one half of the joint with an artificial surface and leaves the other half in its pre-opearative state. Scott [44] reports that in the 1960s, patients with severe deformity not amenable to the McKeever technique began to receive uncemented hinged metal implant designed by Walldius [120], or the cemented hinged GUEPAR implant [4]. The appeal of hinged implants was in its simplicity (one degree of freedom), and in the fact that all ligaments could be sacrificed since the implant was self-stabilising [4]. Initial results were promising, but failures appeared due to component loosening, metastatic infection, metal synovitis, and degeneration of the unresurfaced patella [44]. The designs of the 1950s and 1960s treated the knee joint as a simple hinge, and therefore did not account for the complex motion of the knee which involves multiple degrees of freedom and constraints [118].

Insall and Clarke [4] categorise knee implants into a surface replacement design, or constrained design. Surface implants can be unicondylar (where only one condyle is replaced), or bicondylar (where both condyles are replaced) [121]. Bicondylar arthroplasty is frequently called Total Knee Arthroplasty (TKA). Bicondylar prostheses are further categorised by Carr and Goswami [3] into functional or anatomical. Anatomical models avoid, and preserve the cruciate ligaments (ACL and PCL). The fixed surface of anatomical designs contains a cut-out slot that serves as a passage for the cruciate ligaments. Functional designs use joint surface geometries that are not anatomical, but which maximise surface area and reduce stress on polyethylene surfaces. Some surgeons choose to retain the cruciate ligaments in functional designs by using movable articulating surfaces to avoid contact between the ACL and PCL. In other cases, the cruciate ligaments are removed, and a 'cruciate-sacrificing' prosthesis is used [3].

The first cemented total condylar knee was developed in the late 1960s to early 1970s by Freeman and Swanson [122-124], which was a functional model. The first anatomical total condylar knee (i.e. resurfaced all condyles) was invented by Kodoma and Yamamoto [3, 125]. The Kodama-Yamamoto Mark I knee [126] was also the first cementless total condylar knee [3]. A precursor to some anatomical models, the Geomedic knee was the first cemented bicondylar knee design that preserved the cruciate ligaments [43]. The first functional model to have a tibial peg for insertion was the Eftekhar Mark III knee, introduced in 1973 [43].

Buechel and Pappas [127, 128] developed a mobile bearing functional design in 1977 that eventually led to their New Jersey Low Contact Stress (NJLCS) model manufactured by DePuy, Johnson & Johnson, USA. In such mobile bearing designs, the tibial component articulating surface has some freedom of movement, and the NJLCS model was the first total condylar knee design with a rotating tibial component [3]. In the late 1970s to early 1980s, the first porous coated total condylar knee was developed by Hungerford *et al.* [129]. Called the porous coated anatomical (PCA) knee, it used a coating of cobalt-chrome beads on the femoral component, and contained pegs that embedded into the femur for stability [129].

Today there are an estimated 150 different types of knee prosthesis systems [3, 43], incorporating a variety of features such as cemented fixation or uncemented press-fit fixation, symmetrical or asymmetrical femoral component, rotating or fixed tibial bearing surface, flat or concave fixed tibial bearing surface, etc. Each design caters to specific patient requirements of gender, size, resurfacing etc., and the choice depends on the preference of the surgeon. For the purposes of this study, a widely used commercial implant, Duracon™ knee system (Stryker Corporation, Kalamazoo, MI, USA), will be employed in the experimental and finite element analyses.

4.2 The Stryker® Duracon TS™ knee system

The Duracon™ Total Stabiliser is a revision knee system manufactured by Stryker Orthopaedics (Stryker Corporation, Kalamazoo, MI, USA) [46]. The Duracon is a modular knee system, where the femoral component and the core tibial component are both made of cobalt-chromium-molybdenum (CoCrMo) alloy. The tibial bearing inserts are made of ultra high molecular weight polyethylene (UHMWPE) [46].

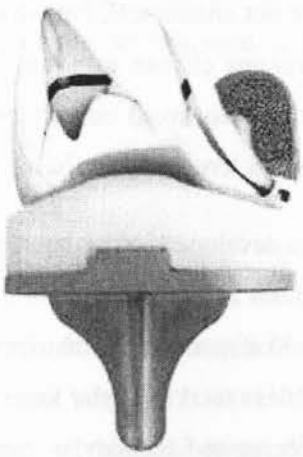

Figure 4.1 The Stryker® Duracon™ knee system [130]

A Duracon system was used in the experimental analysis in this study, as explained in Chapter 6, p.46. The geometry of the Duracon femoral and tibial components was replicated to generate the CAD model used in the FE study, as explained in Chapter 7, p.66. The material properties of the implant components used in the FE study are discussed and listed in Section 8.3, p.75.

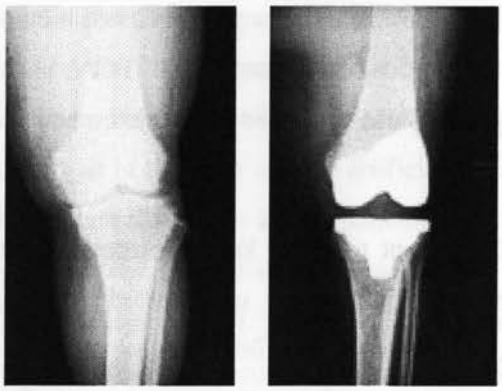

Figure 4.2 Pre-op (left) and post-op (right) radiographs using a Duracon impant system [131]

4.3 Prosthesis failure

The combined structure of the bone-implant system is a composite structure replacing bone, which is itself a composite made out of cancellous and cortical bone [2]. After arthroplasty, the new structure will consist of both cancellous and cortical bone, the implant, and usually some sort of interface layer or cement. Cementless implants also give rise to interface layers [2]. The bone-implant structure must be able to withstand forces applied to it due to the contact between the articulating surfaces of the knee prosthesis. Prosthesis failure may occur in the prosthetic structure itself [55, 132-135], in the bone-implant interface [136-139], or within the structure of the bone [8, 12, 13, 17, 22, 23, 140, 141].

Implant materials need to be of adequate strength to function for extended periods of usage [142], and must be compatible with the biological environment around them [143]. Fatigue behaviour of metals and polymers used in implants is of important concern, since cracks and flaws in the prosthetic materials do not heal on their own like biological tissue and consequently get worse under repeated loading [144, 145]. Besides the fatigue of prosthetic materials, there a variety of documented causes for the failure of knee implants that include patellar instability [146-148], wear in the tibial polyethylene surface [55, 133-135, 149], infection caused by debris generated from worn surfaces [11, 132, 150], crushing of the cancellous bone tissue below the tibial plate [2], implant loosening and migration [3, 14, 139], and stress shielding [8, 13, 17, 28, 30, 151-154]. Each cause of failure merits its own detailed study so that the overall implant behaviour may be predicted and improved, but this study is only concerned with the failure of the femoral component of the implant caused by stress shielding.

4.3.1 Load transfer and Stress shielding

Interfaces may vary from simple bony contact that allows only shear and compressive loads [155], to bony ingrowth interface layers that provide transfer for tensile, compressive and shear loads [136, 152, 156, 157]. In some instances there may be a fibrous layer that provides a less-stiff connection between the bone and implant [2]. To study all forms of prosthesis failure, it is important to understand how loads are transferred from the prosthetic components to the attached skeletal structure. For the purposes of this study, the specific failure mechanism of concern is implant loosening and bone resorption due to stress shielding in the femoral component. The consequences of load transfer from implant to bone (or the lack thereof) that eventually cause implant loosening will be discussed in the following paragraphs.

Loading applied to the bone tissue by the implant surfaces may be substantially different from the loading originally applied on the same region before implantation. This phenomenon is an extremely important consideration when designing implants, since the living skeletal tissue remodels and adapts itself when the loading environment is altered. For instance, if loading on the bone tissue is increased, both the

volume and mechanical properties of the bone may eventually increase in response through growth and accumulation of bone tissue. When an artificial structure is implanted, such as the femoral or tibial components of knee prostheses, the load previously carried by the surrounding bone tissue will now be shared between the implant structure and the bone. As a consequence, the amount of load carried by the bone tissue is generally reduced, and the bone tissue will adapt and remodel according to the new loading situation [2, 13, 140].

The reduction of loading on the bone tissue due to the presence of higher stiffness prosthetic materials is known as *stress shielding*, and the consequent reduction of bone volume and stiffness is termed *bone resorption* [2]. Tayton *et al.* [9] and Christel *et al.* [10] have shown that the degree of stress shielding is proportional to the degree of stiffness mismatch. Angelides *et al.* [15] demonstrated that stresses near the articulating surfaces of the distal femur was decreased by one order of magnitude after femoral component implantation. The consequences of bone resorption due to stress shielding can be quite disastrous for the resurfaced knee joint [17]. While prosthetic components are required to be of sufficient stiffness to withstand physiologic loads over extended periods of time, this requirement eventually gives rise to problems of stress shielding. There is sufficient radiographic evidence that displays changes in bone volume and mineral density near implant-bone interfaces after TKA procedures, proving the importance of mitigating stress shielding in improving implant performance [17, 22].

4.3.2 Bone resorption

In composite systems like bone-implant systems, there exist parallel load paths among which the load is shared according to the relative stiffness of the components in the composite structure. When the prosthesis is implanted, the stiffness of the bone may decrease due to decreased load carried by the bone, which will increase the relative stiffness of the implant with respect to the bone. This in turn will cause the implant to carry more of the load, further reducing the load fraction carried by the bone, thereby causing a further decrease in bone stiffness [2]. This cycle of consistent, ongoing decrease in bone stiffness is called *osteolysis*. In a survey of the most common reason for revision surgery, Benjamin *et al.* [158] have shown 21% of the surgeries were due to complications of osteolysis. Osteolysis due to the presence of implant material may reach a point where the structural integrity of the system is compromised and the risk of failure of both the bone and fixation stems is increased [11, 19]. It must be noted that osteolysis may also result from wear debris of prosthetic material [11, 18], but this study is specifically concerned with addressing osteolysis and bone resorption as a result of stress shielding.

4.3.3 Evidence of bone loss in the distal femur after TKA

Cameron and Cameron [151] conducted a series of four-year follow-up examinations of 65 ICLH Freeman-Swanson knees (Protek, Switzerland), and a 3-month to 36-month follow-up of 120 Tricon P knees (Richard Manufacturing Co., Memphis, TN, USA) in 1987. The X-ray examinations revealed a marked increase in the porosity of bone tissue (or *osteoporosis*) in the femoral condyles, which the researchers called 'stress-relief osteoporosis'. The degree of osteoporosis was categorised into nothing, minimal, mild, moderate, and severe. In almost all cases, it was found that osteoporosis occurred in the anterior regions of the femoral condyle closest to the femoral implant. 83% of the ICLH knees showed mild to severe stress relief osteoporosis after four years. In case of Tricon P knees, 68% of the 3-month old knees indicated minimal-moderate osteoporosis, and all of the 36-month old knees showed mild-severe osteoporosis. Osteoporosis was most prevalent in the anterior part of the distal femur, shown in Figure 4.3 (labelled 'no load'). The fact that this phenomenon occurred in two totally different types of femoral components showed that this is not implant dependent [151].

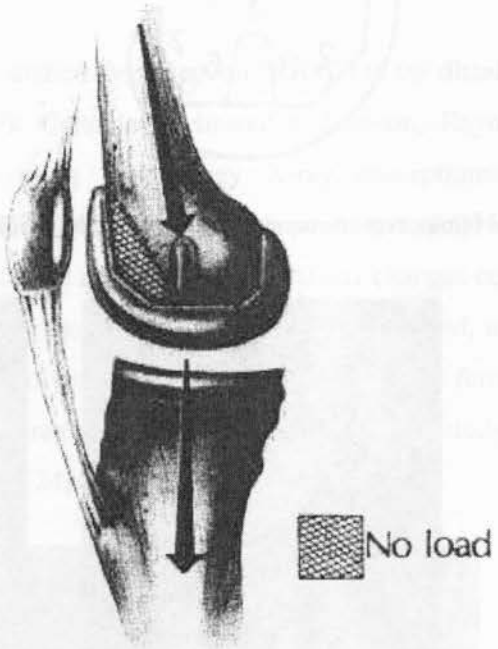

Figure 4.3 Diagram showing load transmission from femur to tibia (arrows), and region of no load (labelled) as per Cameron and Cameron [151]

Mintzer *et al.* [23] conducted a more systematic study in 1990 by following bone loss in marked regions of the distal femur. A total of 147 were studied, where postoperative X-ray examinations were compared to follow up X-rays (between 1-8 years). 51 cases were cemented KII prosthetic knees (Kinematic II, Howmedica, Rutherford, NJ, USA), 49 were uncemented PFC knees (Press Fit Condylar, Johnson & Johnson, Braintree, MA, USA), 27 were cemented PFC knees, and 30 were cemented KI (Kinematic I,

Howmedica). The researchers marked out zones in the distal femur as shown in Figure 4.4, and used these labels to track bone loss. Bone loss was most frequently detected in zones 1, 2, and 3 (see Figure 4.5). Bone loss in the zones 4-7 occurred in only less than 3% of the cases reviewed. Interestingly, increase in bone density was observed in the posterior regions of the femur (zones 5-7) in 4% of the cases. All these cases were associated with anterior bone loss in zones 1-3. This increase in the bone density in some locations was attributed to remodelling due to the re-distribution of stresses after TKA. It was concluded that the prevalence of bone loss was independent of the mode of fixation (cemented or uncemented) and implant design. Mintzer *et al.* also noted that since a change in bone density of at least 20% may be required before it can be detected in X-ray radiographs, apparent bone loss may indicate that the bone strength in the distal anterior femur is considerably compromised as bone strength is proportional to the square of its density [23].

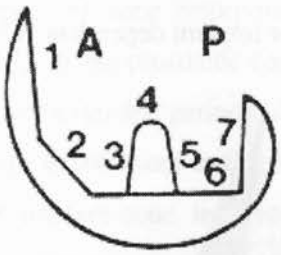

Figure 4.4 Distal femur regions marked into 'zones' by Mintzer *et al.* [23]

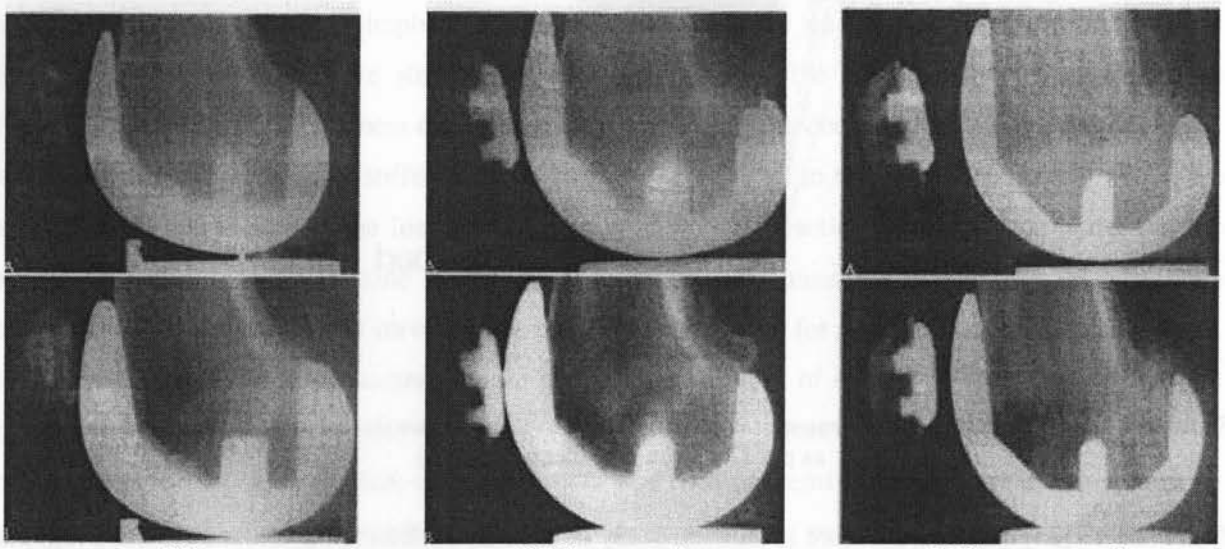

KII
1 year follow up

PFC cemented
2 year follow up

PFC uncemented
2 year follow up

Figure 4.5 Postoperative (top) and follow up (bottom) radiographs showing significant bone loss in zones 1, 2 and 3, from Mintzer *et al.* [23]

In 1995, Petersen *et al.* [8] studied quantitatively the change in bone mineral density (BMD) of the distal femur after uncemented TKA. A reduction in mineral density is a condition termed *osteopenia*, which is usually a precursor to osteoporosis. Eight patients participated, all with PCA Primary prosthetic knees (Howmedica, Rutherford, NJ, USA). BMD was measured using dual-photon absorptiometry with a gadolinium-153 source. The post-operative measurements were conducted at 0-3 months and 2 years. Three locations were examined – (1) behind the anterior flange of the femoral component, (2) above the femoral pegs, and (3) and behind the pegs in the posterior region of the distal femur. Between 3 months and 2 years, significant mean reduction of 36% in BMD was observed behind the anterior flange (region 1). Above the femoral pegs (region 2), the mean BMD increased by 22%, and in the posterior region of the distal femur (region 3) the BMD remained unchanged. These results indicate that there is a marked change in bone mineral densities in the distal femur after TKA, usually involving a reduction in bone mass in the anterior region of the distal femur, and sometimes associated with a corresponding increase in bone mass in the posterior regions. These findings are consistent with those observed by Mintzer *et al.* [23] discussed earlier [8].

In 2001, van Loon *et al.* [24] also studied the reduction of BMD in the distal femur of 12 cases implanted with PFC knee system (Press Fit Condylar, Johnson & Johnson, Raynham, Massachusetts, USA). Measurements were conducted using dual-energy X-ray absorptiometry (DEXA). The density measurements were taken after TKA operations, and compared with follow-up results after 1 year. The study also measured the BMD in the hip and spine to study if any changes occurred in the femoral neck or lumbar regions after prosthetic knee implantation. The study concluded, as expected, significant distal femoral bone loss occurred – especially behind the anterior flange of the femoral implant (see Figure 4.6). The mean decrease in BMD in this region after 1 year was 22%. The study also observed no change in BMD in the hip and lumbar regions [24].

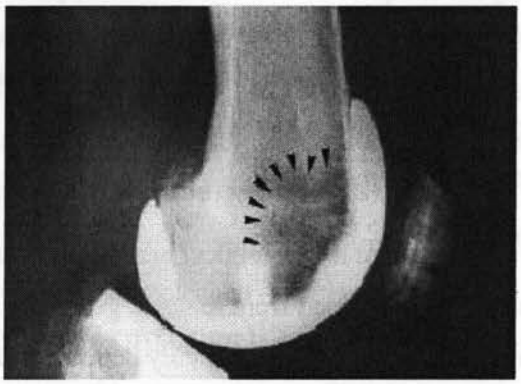

Figure 4.6 Lateral radiograph with arrowheads showing osteopenia behind the anterior flange; from van Loon *et al.* [24]

A more recent study in 2004 by Soininvaara *et al.* [20] also examined the BMD in the distal femur of 69 patients 1 year after TKA surgery. Thirty-seven of the cases were implanted with the modular Duracon system (used later in the experimental portion of this study), 23 cases were Nexgen knees (Zimmer, Warsaw, IN, USA), and 9 were AMK knees (DePuy, Johnson & Johnson, Warsaw, IN, USA). The highest rate of bone loss occurred in the first 3 months after the surgery. An average decrease in bone density of 17.1% was observed after one year in the region most adjacent to the implant. No significant effect of gender, or implant design was seen in the results. Age and body mass index were found to be determinants of bone loss [20].

Reviewing all clinical studies conducted to investigate the prevalence of bone loss in the distal femur, all of them agree that bone resorption is severe, and occurs within the first two years after knee surgery. The overwhelming evidence suggests that the most drastic bone loss occurs in the anterior region, just behind the flange of the femoral implant – suggesting this is the location where stress shielding is at its highest. There are indications that the other regions in the distal femur (such as the posterior region, and around the fixation pegs) experience an increase in bone density, and this has been attributed to an increase in the stress transfer in these regions (low shielding). All researchers agree that the bone loss causes gradual but definite implant loosening that directly influences the frequency of revision surgeries. All authors also indicate that the incidence of bone loss is independent of implant design and gender. It follows that managing stress shielding to replicate the normal physiological environment in bone tissue is an important factor in improving implant longevity.

4.3.4 Prevention of stress shielding to date

The literature on stress shielding is vast for tibial knee implants and hip implants, but very few studies suggest remedies for the stress shielding in the femoral knee implant. Those discussed in previous studies involve either improving geometry or altering mechanical properties, including implant fixation techniques, custom designed implants, and using 'isoelastic' implant material. As far as implant fixation techniques go, Mintzer *et al.* [23] in 1990 already showed that bone loss in the distal femur due to stress shielding was independent of cementing (discussed in the previous section). This eliminates cementing (or lack thereof) as a potential area of improvement.

Recently, in 2007, Harryson *et al.* [159] studied the theoretical benefits of custom-designed femoral knee components using a finite element model developed from realistic geometry import. The motivation for this study was that the longevity of a cementless implant is highly dependent on the initial fit between the bone surface and the implant – which is best if the implant is custom-designed. CT scans of a patient's knee joint were used to generate a custom design for the femoral knee implant. Using finite element

modelling, the performance of the custom design was compared to that of a conventional one. As indicated by the results, one of the many advantages observed was an 'even' stress distribution generated at the bone-implant interface – when compared with the uneven stress distribution caused by the conventional design. However, the stress distribution did not indicate any actual *reduction* in stress shielding, i.e. the custom design did not reproduce the natural 'implant-less' loading environment in the bone tissue. It remains to be studied if the observed 'even' distribution of stress will somehow contribute to any reduction in long-term bone loss [159].

'Isoelastic' implants are meant to mimic the elasticity of the surrounding bone tissue. This solution has been widely suggested in the past only for orthopaedic hip implants [33-36]. Mathys [33] developed a cementless isoelastic hip implant femoral stem in 1973-74, made out of a thick layer of polyacetal resin around a thin steel core. Clinical studies of Mathys' design by Niinimaki *et al.* [36] after a mean follow-up duration of 8.2 years found that 31 of 71 cases showed good fixation and functional result, while 24 of the 71 cases showed considerable loosening. The researchers concluded that, overall, the uncemented isoelastic stems indicated a high rate of loosening, but offered no explanation as to why many cases showed good functional results. The loosening can be attributed to the uncemented nature of the implant fixation, which may have lead to micromotions and subsequent loosening. To reduce the risk of loosening in polymer composite implants, there now exist biocompatible hydroxyapatite coating material that may be applied on implant surfaces to induce osseointegration (bone growth into the implant surface coating) [37, 42, 160]. To the author's knowledge, there has been no study to date that has attempted to pursue isoelasticity in femoral knee implants – which is the main focus of this thesis study.

4.4 Polymer composites in knee prostheses

The conflicting requirement of high-strength and low-stiffness (low elastic modulus) to reduce stress-shielding, which is generally not possible using metallic components, gave rise to the possibility of using polymer composites for orthopaedic applications [161]. The merits of using polymer composites include the convenience of controlling the volume fraction of the constituent materials and their overall arrangement in the macrostructure to produce tailored-for-requirement composites. Also beneficial are the absence of corrosion (biocompatibility and bioinertness), and the possibility of designing radio-transparent composites that do not interfere with X-ray radiography [161]. Two polymer composites relevant to this study are ultra high molecular weight polyethylene (UHMWPE) and carbon fibre reinforced polyamide 12 (CF/PA12). UHMWPE is a choice bearing material in nearly all contemporary state-of-the-art tibial components of knee prostheses. CF/PA12 is a more recently innovated polymer composite that this study aims to incorporate into femoral components to reduce stress shielding in distal femurs.

4.4.1 Ultra high molecular weight polyethylene (UHMWPE)

Ultra high molecular weight polyethylene is a unique polymer notable for its chemical intertness, lubricity, impact resistance, and abrasion resistance. UHMWPE has been used as a bearing material in artificial joints since 1962 [149]. Despite desirable qualities, wear and damage of the UHMWPE components has been one of the major factors limiting orthopaedic implant longevity [11, 18, 55, 132, 134, 135, 162, 163]. More recently, highly crosslinked (sterilised by gamma ray irradiation) and thermally treated UHMWPE available since 1998 has been the major innovation in reducing wear and surface damage in tibial inserts. Crosslinking is obtained by irradiation with gamma rays, and possible further heat treatment. Table 4.1 shows the elastic moduli of several types of UHMWPE measured by Kurtz *et al.* [164], including un-irradiated and gamma ray irradiated UHMWPE (note that kGy is a unit of irradiation measure, kilogrey). Though problems of wear remain, it is a fact that there are currently no clinically proven, acceptable alternatives to UHMWPE as bearing material in tibial components of knee prostheses [130].

Type of treated UHMWPE	Elastic modulus (MPa)
Un-irradiated	830
30 kGy γ, Nitrogen packed	930
100 kGy γ, treated at 100°C	990
100 kGy γ, treated at 150°C	780

Table 4.1 Elastic moduli at room temperature for different types of UHMWPE [164]

Like other thermoplastics, UHMWPE shows a complicated nonlinear response during loading and unloading. The behaviour is characterised by initial linear viscoelasticity at small strains, followed by localised yielding with increasing deformation at sites where the flow resistance is lowest. At large deformations, the molecular chains are stretched and realigned, continually stiffening the mechanical response until ultimate failure. Values for true stress in tension are can be very different from that in compression, for a given applied strain. This behaviour is further complicated by a dependence on strain rate and temperature [165]. Figure 4.7 and Figure 4.8 show strain rate and temperature dependence, respectively, for 100 kGy (kilogrey units) gamma-sterilised UHMWPE in compression. Several models have been proposed to predict the behaviour of UHMWPE, namely the simplest linear elasticity model shown by Kurtz et al; the hyperelasticity, linear viscoelasticity, and isotropic J_2-plasticity models considered by Bergström [165]; and the most complex hybrid model (HM) developed by Bergström and colleagues [166-169]. These relevance and suitability of each of these models will be summarily discussed in the following paragraphs.

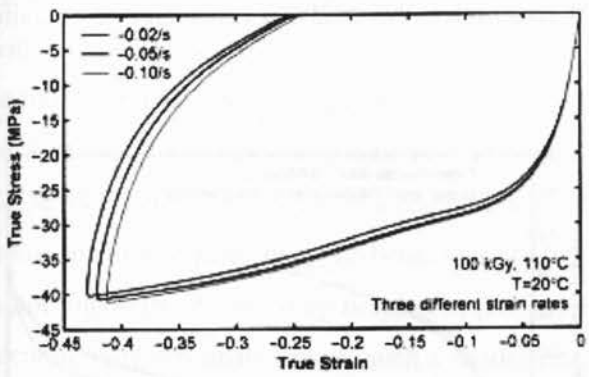

Figure 4.7 Strain rate dependence of UHMWPE in compression [165]

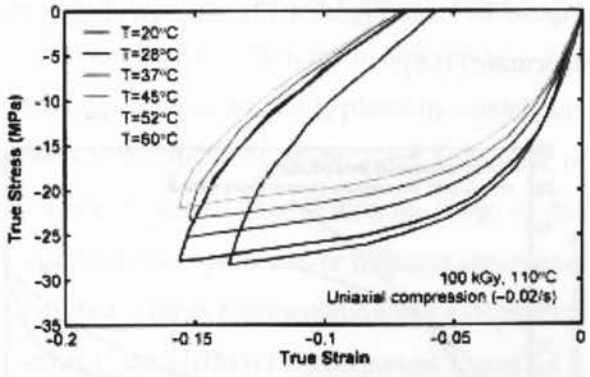

Figure 4.8 Temperature dependence of UHMWPE in compression [165]

The linear elasticity model is the most basic of all models, where only two material parameters need to be determined experimentally – the elastic modulus and Poisson's ratio. Values of elastic modulus for virgin and crosslinked UHMWPE at room temperature are given by Kurtz *et al.* [164] shown earlier in Table 4.1. According to Bergström [165], it is often sufficient to assume a Poisson's ratio value of 0.4, and also states that unless the UHMWPE component is highly confined, Poisson's ratio has a very weak influence on the predicted material response. The linear elasticity model is only accurate for very small strains (less than 0.01) under compression loading as shown in Figure 4.9, where a modulus of 900 MPa shows the best fit. A hyperelasticity model considered by Bergström [165] based on the word of Ogden [170] does not reproduce data obtained experimentally at any point in the compression, as shown by Figure 4.10.

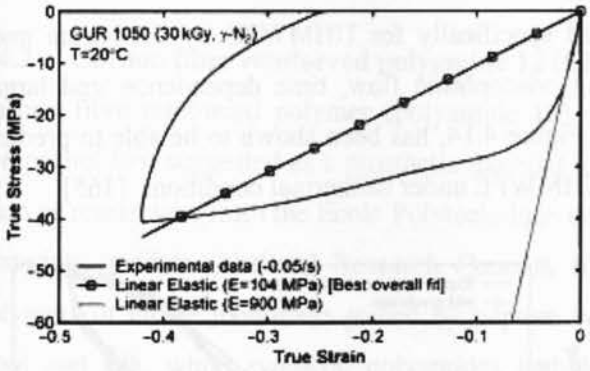

Figure 4.9 Linear elasticity model compared to actual behaviour in compression [165]

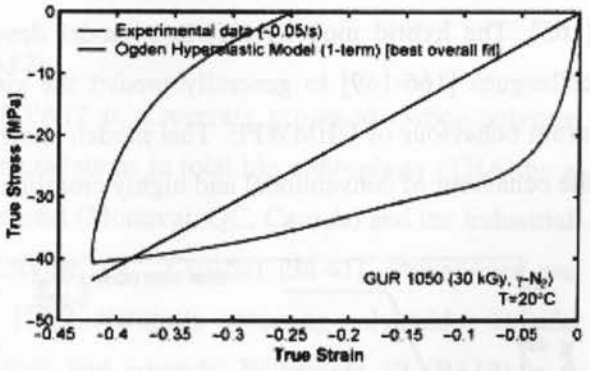

Figure 4.10 Ogden hyperelasticity model compared to actual behaviour in compression [165]

The linear viscosity model can be used to predict time dependence and viscoelastic flow, and is shown to be applicable only at strains below yield strain. The deformation predictions are dependent on relaxation terms (relaxation moduli) expressed as a power series of exponential functions called the Prony series [165]. Depending on the number of Prony series terms applied, the linear viscoelasticity model shows good fits for small to moderate strains (below yield strain) at a strain rate of -0.05/s in compression

(Figure 4.11 and Figure 4.12). At even slightly different strain rates, this model is considered to be quite inaccurate [165].

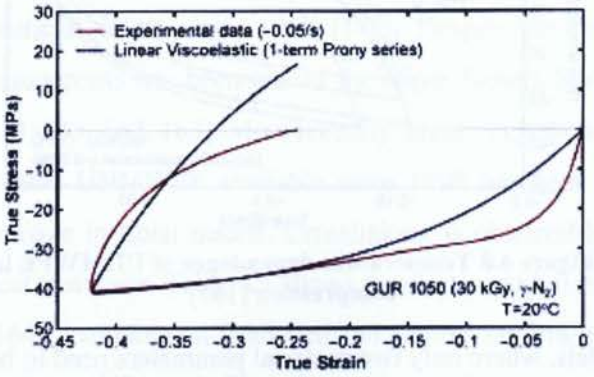

Figure 4.11 Linear viscoelasticity model (1-term Prony series) compared to actual behaviour in compression [165]

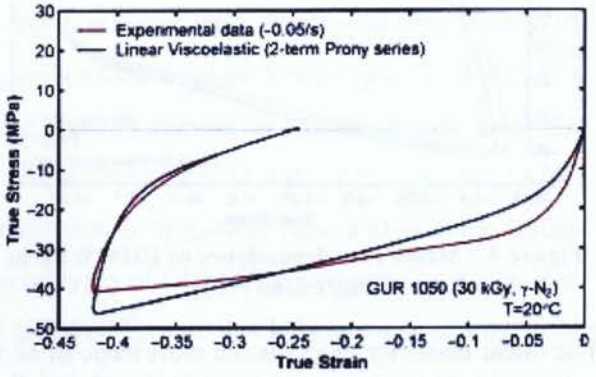

Figure 4.12 Linear viscoelasticity (2-term Prony series) model compared to actual behaviour in compression [165]

The isotropic J_2-plasticity theory is based on classical metals plasticity theory, and is essentially a piecewise linear model (see Figure 4.13) in which material parameters specify the vertices of the stress-strain curve [165]. This model can be made to fit monotonic, constant strain rate, constant temperature data sufficiently well. The limitations of this model are it always predicts a linear unloading behaviour (shown clearly in Figure 4.13) and it is incapable of considering the influence of different deformation rates. It is an inaccurate tool to predict cyclic, and large-deformation-to-failure behaviour of UHMWPE [165]. The hybrid model (HM) is a model developed specifically for UHMWPE by Bergström and colleagues [166-169] to generally predict the yielding, viscoplastic flow, time dependence, and large strain behaviour of UHMWPE. This model, shown in Figure 4.14, has been shown to be able to predict the behaviour of conventional and highly crosslinked UHMWPE under isothermal conditions. [165]

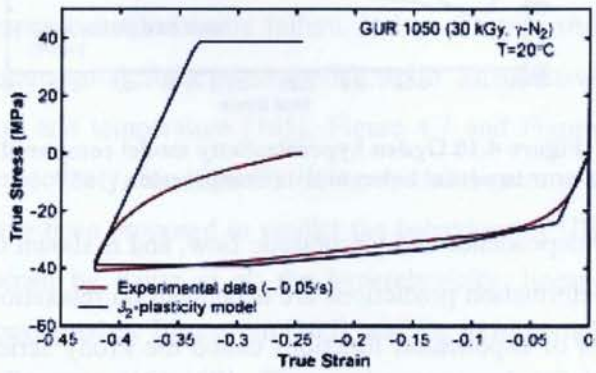

Figure 4.13 J_2-plasticity model compared to actual behaviour in compression [165]

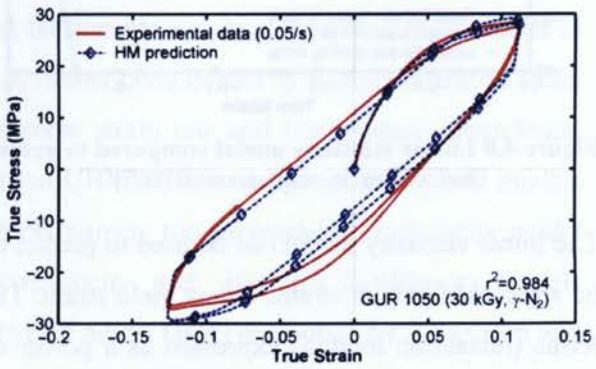

Figure 4.14 Hybrid model by Bergström and colleagues [166-169] **compared to actual behaviour in compression**

Each of the models discussed so far may be applied depending on the importance of UHMWPE behaviour within the scope of the study. For instance, should cyclic behaviour be important, the hybrid model would be most suitable. If only loading behaviour at constant strain rates is required, the J_2-plasticity model may be applied. The linear viscoelasticity model may be applied if the focus of study is the behaviour of UHMWPE below yield strain at a compression deformation rate around -0.05/s. Within the scope of this study, the time-dependent cyclic behaviour of UHMWPE at different temperatures or different strain rates is not important. As noted by Bergström [165], "although a linear elastic representation of UHMWPE is accurate only for small strains, such a model can be of value if the UHMWPE component is part of a larger system and the response of the UHMWPE component is not the focus of the study and has little influence on overall response". As such, a linear elastic model will be applied in this study in FE simulations of the UHMWPE tibial bearing.

The Duracon implant system used in this study incorporates a highly crosslinked UHMWPE commercially advertised as the N2\Vac™ (Stryker Corporation, Kalamazoo, MI, USA) gamma-sterilised UHMWPE (not heat treated, i.e. annealed or remelted). As published by the manufacturer, the uniaxial yield strength for this UHMWPE is 23.2 ± 0.4 MPa; ultimate strength is 54.8 ± 2.5 MPa. As the density of the N2\Vac is not specifically listed, the density of UHMWPE used in this study is 939.2 kg/m^3, or 0.9392 g/cc, which is the density of another variant of UHMWPE with similar strength and modulus developed by Stryker Corporation advertised as the X3™ Advanced Bearing Technology (this variant has improved wear characteristics, but maintains the same strength and modulus as the N2\Vac) [171].

4.4.2 Carbon fibre reinforced polyamide 12 (CF/PA12)

Carbon fibre reinforced polymer (polyamide 12) or CF/PA12 is a recently proposed carbon-polymer composite, first suggested as a prosthetic material for femoral stems in total hip arthroplasty (THA) by a team of researchers from the École Polytechnique de Montréal (Montreal, QC, Canada) and the Industrial Materials Institute (National Research Council, Boucherville, QC, Canada) [38-41]. Polyamides are polymers of amide monomers joined by peptide bonds [172]. Naturally occurring polyamides include wool and silk, while synthetic polyamides include nylons and aramids. Polyamide 12 (PA12) is a commercially available thermoplastic polymer that can contribute to the development of suitable biomaterials when reinforced by carbon fibres [39, 40]. CF/PA12 has shown to be a highly suitable biomimetic material especially in hip implant stems. The innovation in this study is the use of CF/PA12 in knee implants by lining the posterior surface of the femoral component.

The first study on the structural properties of CF/PA12 were conducted by Campbell *et al.* [38, 39] published in 2006. Tests were conducted on hollow cylindrical geometries with 3 mm wall thickness

manufactured using polyamide 12 (PA12) matrix reinforced with long discontinuous carbon fibres (CF). In its initial state, the composite material comes in the form of braided non-consolidated strands with a fibre orientation varying between 20 and 45 degrees. The idea was to vary the orientation of each layer in the composite stem to control material properties in different directions. These femoral stems were manufactured by inflatable bladder moulding, a process that combines compression moulding (where two heated plates are used to simultaneously compress the composite material) and bladder moulding (where a hollow tube is produced by moulding over an internal bladder). Braided carbon fibre and polyamide 12 strands are mounted onto an inflatable bladder and then inserted in a mould cavity, as shown in Figure 4.15. The mould is closed and placed into a heated press at an optimum temperature and pressure, for an optimum amount of time. The optimum manufacturing conditions are those which produce the least void content or air pockets (good consolidation quality) in the composite material, as were eventually studied by Campbell *et al.* [40]. The theoretical density of this composite is 1.448 g/cc, but te actual density of the moulded CF/PA12 material under optimum conditions was calculated to be 1.42 g/cc using Archimedes' method [38, 39]. The constituent characteristics of the resulting CF/PA12 composite (where the fibre phase is carbon, and the matrix phase is polyamide 12) is given in Table 4.2 [40].

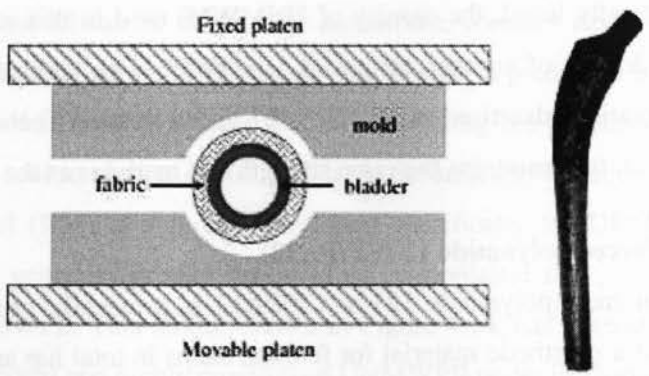

Figure 4.15 Inflatable bladder moulding to manufacture CF/PA12 THA femoral stems [40]

CF volume fraction	0.55
CF weight fraction	0.683
Density of CF (g/cc)	1.78
Density of PA12 (g/cc)	1.03
Diameter of CF fibres (μm)	10

Table 4.2 CF/PA12 composite constituent properties [40]

The femoral stem was modelled to resemble cortical bone in behaviour. In the 2006 study by Campbell *et al.* [38, 39], five hollow cylindrical test specimens were tested. Each consisted of six layers of composite

braided CF and PA12 strands that have a specific ply configuration – the CF in the first two layers are oriented at ±45°, followed by one layer with 0/90° orientation, followed by three layers with ±45° orientation. The best consolidation quality (indicated by a density that is closest to the theoretical density of 1.443 g/cc) was reported to be obtained at a temperature of 250°C, at a pressure varying between 50-90 psi, for a holding time of 4 minutes. Using Archimedes' method, the actual density at optimum moulding conditions was measured to be 1.43 g/cc – the closest obtained to the theoretical density. Uniaxial compression tests were conducted on five 44 mm-long samples with 3 mm-thick walls, and outer diameter 22 mm. Compression was performed by an electromechanical machine (model and manufacturer not reported) using 100 kN load cell with parallel plates. Compressive strength and strain were calculated from the load-deflection curves at the maximum load value. The compression results are reproduced in Table 4.3. The results indicate that the hollow cylindrical test spcimens possessed properties that resembled cortical bone in the human femur. The compression stress-strain curve for a typical specimen is given in Figure 4.16. The curve shows a typical linear elastic region ending when maximum strength is reached, where failure can occur by barreling or buckling, as shown in Figure 4.17 [38, 39].

Stem specimen	Bulk compressive modulus (GPa)	Bulk compressive strength (MPa)	Strain at maximum strength (%)	Density (g/cc)
1	15.5	167	1.94	1.39
2	14.0	177	1.88	1.40
3	14.5	179	1.83	1.40
4	15.8	178	1.70	1.37
5	15.4	217	1.85	1.40
Mean	**15.1**	**184**	**1.84**	**1.39**
Standard deviation	0.8	19	0.09	0.01

Table 4.3 2006 compression test results of CF/PA12 specimens by Campbell *et al.* [38, 39]

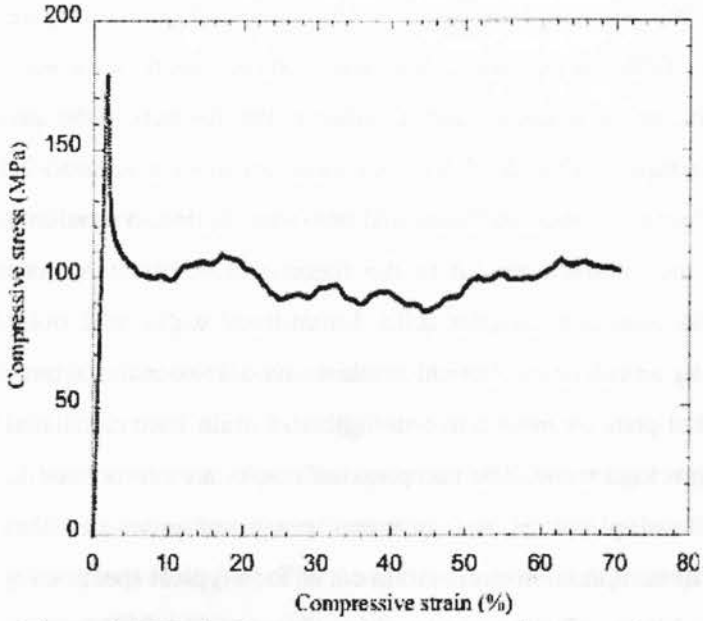

Figure 4.16 Typical compression stress-strain curve of CF/PA12 cylinders by Campbell *et al.* [38, 39]

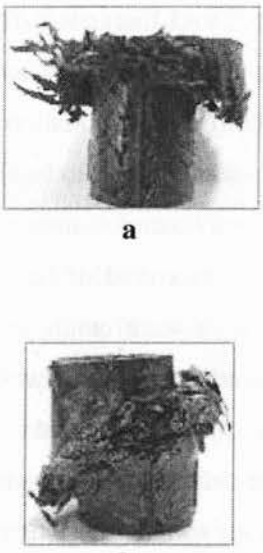

Figure 4.17 Failed stem samples after compression testing: a) barrelling, and b) buckling along the 45° shear plane [38, 39]

In 2008, Campbell and colleagues published two studies; one on the manufacturing and properties of CF/PA12 hollow cylinders and hip implant femoral stems [40], and another on the performance of the femoral stems [41]. In the first study, Campbell *et al.* [40] published a more detailed analysis of the optimal manufacturing conditions for CF/PA12 to obtain a composite structure with the best consolidation quality possible (low void content) and therefore the highest stiffness and rigidity. CF/PA12 in the form of braided sleeves of co-mingled CF and PA12 strands were used in the study to manufacture actual hip implant femoral stems as depicted earlier in Figure 4.15 (not just hollow cylindrical specimens). The femoral stems were again manufacturing by inflatable bladder moulding, where six layers of braided sleeves of CF/PA12 yarns were placed around a silicone bladder mandrel [40].

Several manufacturing conditions were studied in the 2008 study by Campbell *et al.* [40], and this time the optimal moulding conditions was shown to be at a temperature of 250°C and compression pressure of 480 kPa, maintained for 5 minutes. The compression performance of femoral stems manufactured at different moulding conditions were compared. As in the 2006 study [38, 39], the stress-strain curves indicated that the femoral stems also undergo a linear stress-strain behaviour when subjected to compression, followed by yielding and abrupt softening until a plateau is reached. Yielding occurred by shear deformation at ±45° with respect to the loading axis, i.e. along the orientation of the carbon fibres. The maximum load at failure (28-32 kN) was reported to be roughly 10 times larger than normal physiological loads experienced during gait (2.5-3 kN) [40].

In the second 2008 study, Campbell *et al.* [41] showed that the fatigue performance of CF/PA12 material tested surpassed, by far, the required fatigue performance for hip implant stems. Two specimen configurations were used – hollow cylindrical configurations, and hip implant femoral stem configurations. Compression and flexural (short-term) tests were conducted on the hollow cylindrical specimens of CF/PA12 (22 mm outer diameter, 3 mm wall thickness), whereas cyclic fatigue (long-term) tests were performed on both cylindrical specimens and on actual geometry femoral stems. The compression tests indicated a modulus of 12.2 GPa, and ultimate strength of 155 MPa, under a maximum load of 28.6 kN. These values are close to that of cortical bone tissue estimated by Reilly and Burstein [74, 75] (11.5-17 GPa and 133-193 MPa, respectively), and by Wirtz *et al.* [76] (7.0-18.7 GPa and 175-265 MPa respectively). The flexural modulus and ultimate strength of the CF/PA12 cylinder was 16.4 GPa and 188 MPa respectively, which are close to cortical bone tissue properties published by Snyder and Schneider [173] (14.3-21.1 GPa and 178-250 MPa, respectively). The bending stiffness was calculated based on the product of the elastic modulus and moment of inertia. The bending stiffness of the composite cylinders (22 mm outer diameter) was 180-145 N-m^2, which is within range of the cortical bone (of 25-30 mm outer cortex diameter) bending stiffness of 170-500 N-m^2 [41].

	Specimen material	Maximum compressive load (kN)	Modulus (GPa)	Ultimate strength (MPa)
Campbell *et al.* [41]	CF/PA12	28.6 ± 3.8	12.2 ± 1.3	155 ± 27
Reilly and Burstein [74, 75]	Cortical bone	-	11.5-17	133-193
Wirtz *et al.* [76]	Cortical bone	-	7.0-18.7	178-250

Table 4.4 2008 compression test results of CF/PA12 cylinders by Campbell *et al.* [41] compared to cortical tissue

The cyclic fatigue tests indicated that the CF/PA12 cylinders failed at 10^6 cycles at a maximum fatigue stress of 101 MPa (load of 17 kN), and at 10^7 cycles for 95 MPa (18 kN). These results show fatigue limits of 10^6 or more for loads that are at least six times more than the 3000 N recommended by ASTM standards for hip arthroplasty femoral components. In view of these results, the all studies by Campbell and colleagues [38-41] provide convincing evidence proving CF/PA12 to be an excellent candidate material for orthopaedic appliances in general [41].

4.5 Applying CF/PA12 composite in knee implants

To date, no published work exists on the use of CF/PA12 in knee implants. While most of the published work on CF/PA12 (and there are only three, all by Campbell and colleagues [38-41]) studies the material performance when manufactured as hollow cylinders, the results strongly indicate that CF/PA12 will still

be suitable when manufactured to conform to knee implant geometries. Since CF/PA12 most closely resembles cortical bone, the author believes its use is more appropriate in the femoral knee components (which replace cortical regions), as opposed to use in tibial fixation stems (which are usually implanted in cancellous regions of the tibia). As described in the previous section, the CF/PA12 stems for hip arthroplasty were manufactured by inflatable bladder compression moulding. To manufacture a layer of CF/PA12 to conform with femoral implants, a different customised method of compression moulding may be necessary. This, though, is a topic for future work – since developing moulding techniques to manufacture CF/PA12-lined femoral structures would be an expensive endeavour and beyond the financial scope of this study. Meanwhile, the FE analysis conducted in this study will use the bulk compressive properties of this composite as published by Campbell *et al.* [41] in 2008 (shown in Table 4.4).

5 CURRENT STUDY

This study revolves around producing a validated finite element model to test stress characteristics in a prosthetic knee, and reducing stress shielding in the femoral implant which has been shown to cause detectable bone resorption and osteolysis in the surrounding femoral tissue (discussed in Section 4.3, p.28). The suggested remedy (which is the innovation in this study) is altering the structure of the femoral component to include a composite, *biomimetic* material as the interface layer. Carbon fibre reinforced polyamide-12 (CF/PA12) is a mouldable carbon-polymer composite that matches the properties of cortical bone tissue, and has shown promising potential for use in orthopaedic implants (discussed in Section 4.4.2, p.38). The broad goal of this thesis is to replicate the success of CF/PA12 in knee implants.

5.1 Problem statement

High stiffness metallic femoral components of knee prostheses are susceptible to stress shielding, which alters the usual loading environment of the distal femur by preventing the transfer of loads from the implant to the bone tissue – resulting in bone resorption and eventual failure of the prosthesis.

5.2 Research question

Can a hybrid metal-CF/PA12 femoral component be shown to reduce stress shielding observed in conventional metallic femoral components through finite element modelling?

5.3 Aims of this study

The distinct goals of this study are to:

1. Summarise relevant literature on knee joint anatomy, joint biomechanics, knee replacement procedures, and knee implants. Review literature on distal femoral bone loss, the prevention of stress shielding, *in vitro* experimental studies and finite element studies of stress distribution in knee implant systems.

2. Conduct an experimental study of the stresses generated in the bone-implant system under static axial loading using the Duracon TS™ implant system and synthetic composite bone replicas.

3. Develop a computer-aided, realistic geometry of the bone-implant knee prosthesis system.

4. Use the CAD geometry to generate a numerical model for static finite element analysis (FEA) of the bone-implant system. Validate the model by comparing the FEA results with the experimental results obtained earlier, and using published literature.
5. Modify the femoral component geometry to include a CF/PA12 layer, once the numerical model is validated.
6. Evaluate the performance of the hybrid prosthesis when compared with the conventional metallic one for three different flexion angles (0, 20, and 60 degrees).

6 EXPERIMENTAL STUDY

The goal for this experimental study is to validate the finite element (FE) model developed to predict stresses in the bone-implant system. The experiment involved measuring the surface strains on the distal end of the synthetic femur model. A good agreement between the strains measured on the surface and those predicted by the FE model can be considered a sufficient validation of the FE model. Experimental validation using cadaveric bones tend to be rare, due to problems with storage and preventing alterations in the skeletal material properties as the bone tissue ages and dries. This issue has already been discussed in Section 3.5, p.22. Synthetic analogue bone models have been used in several studies in validation experiments [42, 174, 175].

All studies in this thesis will be restricted to studying a static axial loading of the bone-implant system. Considering the estimates of the joint force during normal gait from previous studies discussed in Section 3.3.3 (p.15), this study will be structured around applying compressive forces of 2000 N and 3000 N, which is around 2 and 3 times a nominal body weight of 86.8 kg, respectively. This nominal weight of 86.8 kg is based on the reported mean body weight of the male adult (age 20-74 years) in the US, as per Ogden *et al.* [176].

Applied loads of 2000 N and 3000 N compare well with previous FEA studies conducted on bone-implant systems – 2200 N used by Chu [177] in uniformly distributed compression, two 1000 N compressive forces on the tibial surface used by Miyoshi *et al.* [178], 2200 N maximum axial force used by Godest *et al.* [179], 2300 N used by Halloran *et al.* [180], a maximum of 3000 N compressive force used by Liau *et al.* [181-183], 2200-3200 N used by Villa *et al.* [144] for contact force tests under knee flexion, and 3000 N used by Bartel *et al.* [162] on the tibial component to simulate bicondylar contact. In view of these studies on tibiofemoral contact, axial compressive test loads of 2000-3000 N is reasonably typical.

6.1 Synthetic bones in literature

There are numerous experiments that used cadaveric bones to deduce the mechanical properties of bone [74, 75, 77, 79-83, 88-92, 94-96, 184-190]. These experiments did not utilise complete femur or tibia bones, instead using convenient cut-out cubic or cylindrical portions from different sites on the femur or tibia. Experiments that did use *full* cadaveric specimens (or a substantial portion of a long bone) had been conducted to justify the use of synthetic analogue bones, such as those conducted by McNamara *et al.*

[114], Cristofolini *et al.* [110], and Papini *et al.* [107]. All synthetic composite bone models used in the following experiments were manufactured by Pacific Research Laboratories (Vashon, WA, USA).

McNamara *et al.* [114] conducted four-point bending tests on an embalmed cadaveric femur and four third generation composite femurs (Pacific Research Laboratories, Vashon, WA, USA). These tests were conducted to determine the bending stiffness of the diaphyses of the bones, using this to estimate the elastic modulus. The tests were done using an Instron 8502 (Instron Corporation, Canton, MA, USA) materials testing machine. The bending moment was applied such that compression was generated in the medial aspect, and the lateral fibres experienced tension, thus simulating the physiological bending plane during gait (Figure 6.1). The results of this study indicated that the experimentally determined elastic modulus of the synthetic femurs matched the manufacturer's published data sufficiently (4.2% error), but the estimated cadaveric bone modulus (11 GPa) was significantly different from documented values of cortical bone considered by the McNamara *et al.* (17-18GPa). This study showed that the use of synthetic bones will allow the reproduction of experimental results since their bending stiffness properties agree with the manufacturer's data, and do not vary significantly from specimen to specimen. The study also further indicated that it is not always possible to reproduce experimental results on cadaveric bone [114].

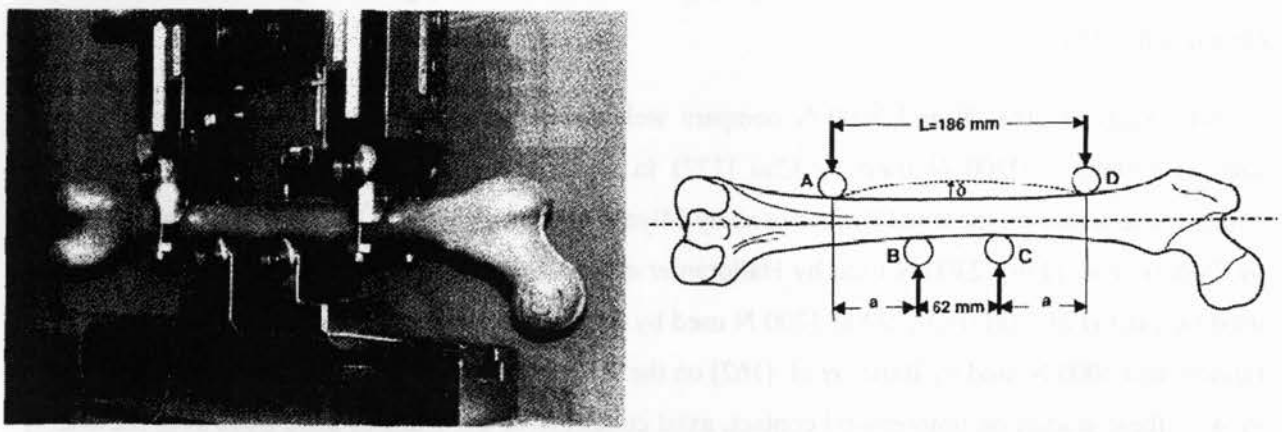

Figure 6.1 Experimental setup to obtain structural bending stiffness by McNamara *et al.* [114]

Cristofolini *et al.* [110] conducted experiments on fifteen composite femurs, four dried and rehydrated human femurs, and four fresh-frozen human femurs. Axial loading, torsion, and four-point bending tests were conducted, as shown in Figure 6.2. The results indicated no conditioning effects of cyclic loading on the composite femurs, with strains measured for repeated loads within ±1% of the mean strain value. The composite models were shown to behave linearly, with some viscoelastic effects observed. No significant difference was observed between the three groups of specimens in mean axial displacement results. The mean torsional stiffness, and bending stiffnesses in the anterior-posterior (A-P) and medial-lateral (M-P) directions for the composite bones were considered to be similar to that of the human cadaveric femurs

(see Table 6.1), though a high inter-specimen variability was observed amongst the cadaveric samples. The torsional stiffness of the composite group was comparable to that of the fresh-frozen samples, but differed significantly from the dried-rehydrated samples (attributed to the brittleness developed by dried cadaveric samples). One again, the composite models showed more reproducibility and repeatability of results when compared to both the cadaveric groups. Cristofolini *et al.* concluded that if one were to consider a standard test benchmark to remove well known obstacles in the use of cadaveric bones, the synthetic composite models can be extremely useful.

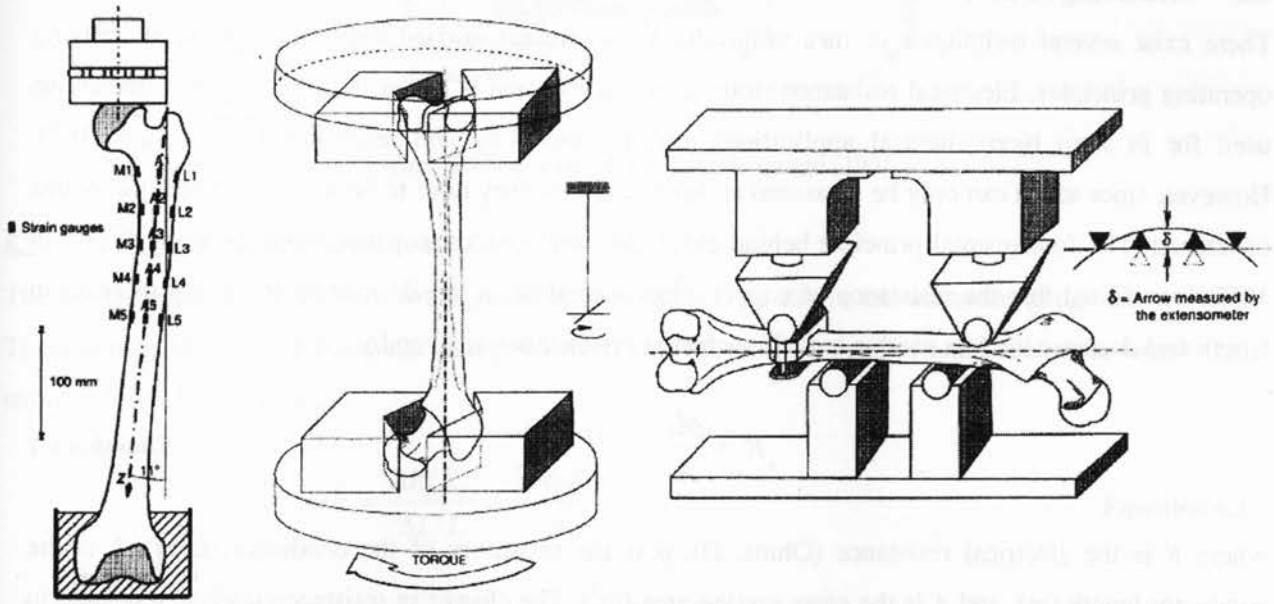

Figure 6.2 Left to right: axial compression, torsion, and four point bending experiments by Cristofolini *et al.* [110]

	Composite femur	Dried cadaveric specimens	Frozen cadaveric specimens
Mean A-P bending stiffness (N/mm)	2350	2550	3250
Mean M-L bending stiffness (N/mm)	2175	2425	2450
Mean torsional stiffness (N-m/degree)	8.4	4.8	6.6

Table 6.1 Approximate mean stiffness values of composite femurs, dried cadaveric femurs and frozen cadaveric femurs as published by Cristofolini *et al.* [110]

Papini *et al.* [107] conducted axial and torsional stiffness tests on cadaveric and third generation composite femurs, as well as an FE study using the geometry of a composite femur. These types of tests were chosen since the human femur was considered to mostly experience axial compression, bending, and torsion. The results of the study indicated that the torsional and axial rigidity of the composite femurs

showed good agreement with previous studies on similar synthetic models conducted by Cristofolini *et al.* [110] (described in the previous paragraph), and Heiner and Brown [191, 192] (not discussed in this report). The study also showed the cadaveric models used to be inferior in stiffness when compared to the synthetic models. Papini *et al.* attribute this to the poor quality of the bone stock due to the advanced age of the cadaveric bone donors, and eventually conclude that the composite bone models are most representative of young, healthy bone stock, rather than aged osteoporotic specimens [107].

6.2 Measuring strain on bone surfaces

There exist several techniques of measuring strain that are categorised depending on the underlying operating principles. Electrical resistance strain gauge application is by far the most common technique used for *in vitro* biomechanical applications, due to sensitivity and resistance to corrosion [193]. However, since strain can only be measured at discrete points, they have to be mounted at specific points of interest. The fundamental principle behind electrical strain gauges was discovered by Lord Kelvin in 1856, who found that the resistance of copper wires increased on tensile loading involving increase in length and decrease in cross section area. The change in resistance is given by

$$R = \frac{\rho L}{A} \qquad \textbf{Equation 6.1}$$

where R is the electrical resistance (Ohms, Ω), ρ is the resistivity of the conductor (Ω-m), L is the conductor length (m), and A is the cross section area (m^2). The change in resistance leads to a change in voltage across the conductor proportional to the current applied to the circuit, as per Ohm's law,

$$V = IR \qquad \textbf{Equation 6.2}$$

where V is the voltage (Volts, V) and I is the current (Amperes, A). The voltage change can be used to derive the actual strain on the gauge. This principle guides the strain measurement in electrical resistance gauges. The basic idea of the experimental use is that when a gauge is well bonded to the test surface, the gauge should perceive the same strain as the test surface under loading, neglecting small losses in the gauge-specimen interface [193].

The majority of strain gauges happen to be bonded foil types, and commercially available foil gauges have been used in this study. A typical foil resistance strain gauge is described by Szivek and Gharpuray [193], given in Figure 1.1. Foil gauges are so named because they consist of a pattern of resistive foil mounted on a backing material. The foil is the actual stress-sensing component and its resistance changes in a defined way when it is mounted on a surface under loading. In a uniaxial strain gauge, as used in this

study, tension in the foil causes the resistance to increase, and compression causes resistance to decrease. The grid pattern maximises the amount of foil subject to strain. The cross section area of the grid is minimised to reduce the effect of shear strain and Poisson strain. The solder tabs seen on the foil gauge in Figure 6.3 are where the wires leading to the data acquisition system are soldered [193, 194].

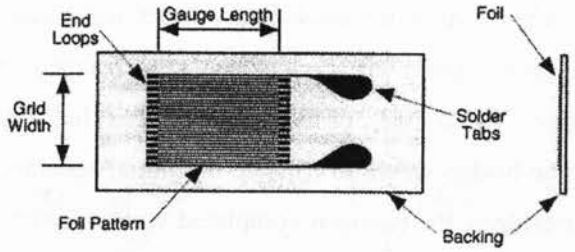

Figure 6.3 Diagram of a foil strain gauge [193]

6.2.1 Gauge factor and sensitivity

The fundamental parameter of a strain gauge is its sensitivity to strain, known as the gauge factor (GF). This factor is the ratio of fractional change in electrical resistance to the fractional change in length (i.e. strain), shown by the relation,

$$GF = \frac{\Delta R/R_G}{\Delta L/L} = \frac{\Delta R/R_G}{\varepsilon} \qquad \textbf{Equation 6.3}$$

where ε is the strain, R_G is the gauge resistance, and ΔR is the change in gauge resistance. As will be seen later (Section 6.2.4, p.52), the length, gauge resistance R_G, and GF of the gauge model selected for this study is 0.125 in (3.18 mm), 350 Ω, and 2.12, respectively. Ideally, the resistance of the strain gauge would change only in response to applied strain. However, the gauge material, as well as the specimen material to which the gauge is applied, will also respond to changes in temperature. Strain gauge manufacturers attempt to minimise sensitivity to temperature by processing the gauge material to compensate for the thermal expansion of the specimen material intended for the gauge. The gauge used in this study has been processed to operate at temperatures between -75°C to 175°C [195].

In practice, the strain measurements rarely involve quantities larger than a few millistrain ($\varepsilon \times 10^{-3}$). Such small magnitudes produce very small changes in resistance, which have to be measured accurately. While the GF provides a small amplification in the strain sensitivity, that in itself may not be sufficient for measurement. For example, suppose a test specimen undergoes a substantial strain of 500 με (microstrain, $\varepsilon \times 10^{-6}$). A strain gauge with a GF of 2 exhibits a change in electrical resistance of only $2 \times (500 \times 10^{-6})$ = 0.1%. For a 350 Ω gauge, this is a change of only 0.35 Ω. To measure such small changes in resistance,

and further compensate for the temperature sensitivity, strain gauges are almost always used in a Wheatstone bridge configuration with a voltage or current excitation source [195].

6.2.2 The Wheatstone quarter bridge circuit

In order to use the strain gauge as a practical instrument, extremely small changes in resistance need to be recorded with high accuracy. This sort of precision necessitates measurement through a Wheatstone bridge circuit. The strain gauge is connected to a Wheatstone bridge circuit, which may be in a combination of four active gauges (full bridge), or two active gauges (half bridge), or just the one gauge (quarter bridge). The Wheatstone bridge serves to balance the initial resistance of the gauge, wires, and connectors. In half and quarter bridges, the circuit is completed with precision resistors. In cases where a single strain gauge is used per channel, a quarter bridge is sufficient for balancing the system [196] (see Figure 6.4). As will be seen later, eight strain gauges are employed in this study; all connected to an eight-channel data acquisition system – therefore a quarter bridge circuit is used in obtaining strain data [193, 194].

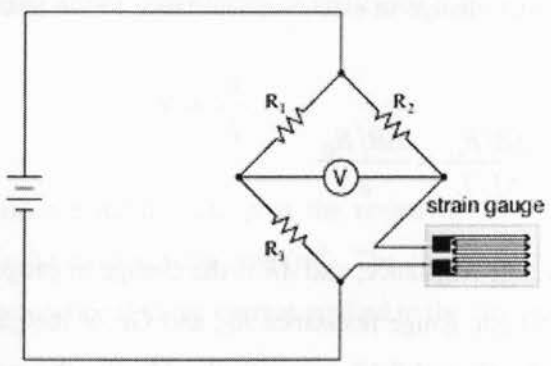

Figure 6.4 Strain gauge in a quarter bridge Wheatstone circuit [194]

The quarter bridge circuit works thus: Usually, the rheostat arm of the bridge (R_2 in Figure 6.4) is set at a value equal to the strain gauge resistance with no force applied. The two ratio arms of the bridge (R_1 and R_3 in Figure 6.4) are set equal to each other. As such, when no force is applied on the strain gauge, the bridge is considered symmetrically *balanced*. The voltmeter will indicate zero volts, representing the absence of applied forces on the gauge. Under compression or tension, the resistance of the gauge foil will decrease or increase, respectively, thereby unbalancing the bridge and prompting a change in the voltmeter output. This arrangement, with a single element of the bridge changing resistance in response to applied mechanical force, is known as a quarter bridge circuit [194].

6.2.3 Strain derived from voltage output

As discussed in the previous section, any changes in strain gauge resistance will unbalance the quarter bridge circuit. Strain is measured by the degree of imbalance, and uses a precision voltmeter in the centre of the bridge to provide an accurate measurement of that imbalance. The voltmeter output (V_o) in a Wheatstone bridge circuit is directly proportional to the source voltage excitation (V_{EX}).

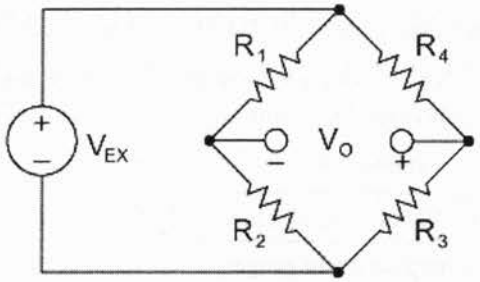

Figure 6.5 Regular Wheatstone bridge circuit [197]

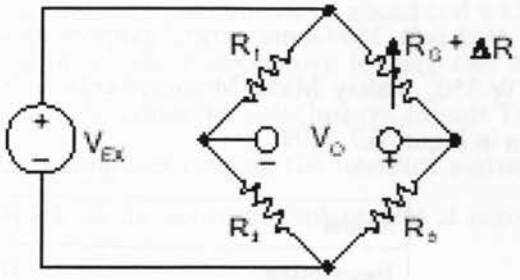

Figure 6.6 Quarter bridge circuit with one strain gauge [195]

In a regular Wheatstone bridge circuit (Figure 6.5), the source excitation and output voltages are related to the element resistances by:

$$\frac{V_o}{V_{EX}} = \frac{R_3}{R_3 + R_4} - \frac{R_2}{R_1 + R_2}$$

Equation 6.4 [197]

For a quarter bridge circuit (Figure 6.6, showing gauge resistance R_G and change in gauge resistance ΔR), this relation can be modified to relate source and output voltage to the gauge factor and strain observed by the gauge:

$$\frac{V_o}{V_{EX}} = \frac{-GF \cdot \varepsilon}{4}\left(\frac{1}{1 + GF \cdot \frac{\varepsilon}{2}}\right)$$

Equation 6.5 [195]

By setting an appropriate excitation voltage, the output voltage V_o can thus be used to calculate the strain ε observed by the gauge. As will be seen later (Section 6.4.3, p.59), the source voltage in this experimental study was set at 5 Volts. Selection of a minimum input voltage, in addition to a high resistance gauge, reduces the self-heating tendency of a gauge [198].

6.2.4 Strain gauge selection

Selecting an appropriate strain gauge depends upon the problem being studied, and the nature of the test materials on which the gauge will be mounted. Some important factors are temperature sensitivity, high

strain sensitivity, and electrical resistivity of the foil [193]. In this study, the *in vitro* experiments are conducted at room temperature, and the test materials have high enough moduli that large strains are not expected under the compressive loads applied (up to 3000 N). Also, due to the poor thermal conductivity of bone material (including simulated bone), Szivek and Gharpuray [193] recommend the use of high resistance gauges (ideally 350 Ω). Since the mode of loading in the experimental study is mainly axial, and the strain direction of interest lies in this direction, uniaxial gauges were considered sufficient. As such, Vishay® 350-Ohms general-purpose uniaxial linear-pattern gauges (125UW, model CEA-06-125UW-350, Vishay Micro-Measurements & SR-4, Raleigh, NC, USA) are employed in this study, shown in Figure 6.7. [199]

Model	CEA-06-125UW-350
Description	Universal general purpose strain gauges
Resistance	350.0 Ω ± 0.3%
Overall length and width	0.325×0.180 in (8.26×4.57 mm)
Strain range	±3%
Temperature range	-75°C to 175°C
Gauge factor, GF (at 24°C)	2.120 ± 0.5%
GF sensitivity	(1.2 ± 0.2) % /100°C
Transverse sensitivity	(0.7 ± 0.2) %

Table 6.2 Vishay® 350-Ohms strain gauge specifications [199]

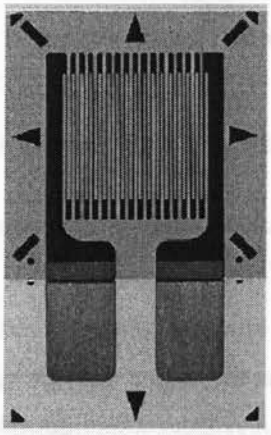

Figure 6.7 Vishay® 350-Ohms uniaxial linear-pattern strain gauge model CEA-06-125UW-350 [199]

6.3 Experiment overview

A medium left fourth generation composite femur supplied by Sawbones Worldwide (Item #3406, Sawbones Worldwide, Pacific Research Laboratories, Vashon, WA, USA) [200], and a Duracon™ knee

implant system manufactured by Stryker Corporation (Kalamazoo, MI, USA) [46] was used in the experiment. The femur model has been described earlier in Section 3.5.1 (p.23), and the Duracon system was introduced in Section 4.2 (p.27).

The mode of loading on the bone-implant system was static axial compression. Two load cases were studied – 2000 N and 3000 N. Axial loading tests were performed using a material testing instrument Instron® 8874 (Canton, MA, USA), shown in Figure 6.8. The Instron 8874 consists of a load cell with a capacity of ±25 kN, resolution of 0.1 N, and an accuracy of ±0.5%. Compressive loading rate and maximum load were input through FastTrack™ 8800 servohydraulic controller unit (Instron, Illinois Tool Works, Norwood, MA, USA) in conjunction with a desktop computer running the interface software FastTrack™ 2. The software is also able to display a feedback on the actuator displacement at regular intervals.

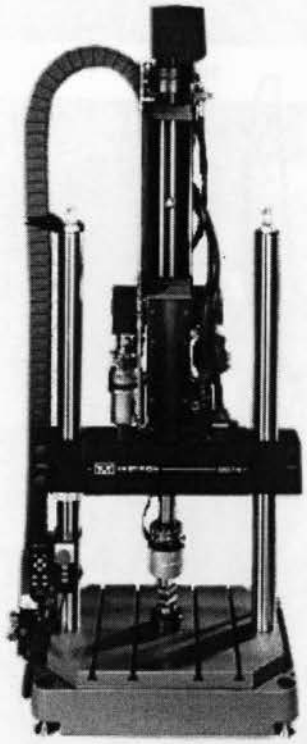

Figure 6.8 Instron® FastTrack™ 8874 [201]

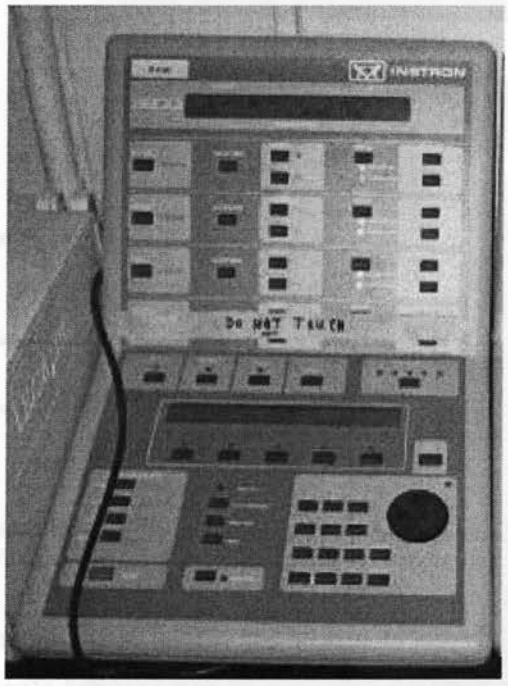

Figure 6.9 Instron® FastTrack™ 8800 controller panel

Surface strain was measured using Vishay® 125UW 350-Ohms general-purpose uniaxial linear-pattern gauges [199] (model CEA-06-125UW-350, Vishay Micro-Measurements, Raleigh, NC, USA) attached to the femoral surface. The gauge installation procedure is described later in Section 6.4.2, p.58. Wire leads were soldered to each gauge. The wires lead to an data acquisition unit CRONOS-PL2 (imc Meßsysteme GmbH, Berlin, Germany) through a UNI2-8 eight-channel all-purpose amplifier. The CRONOS-PL was

connected to data collection notebook computer running signal analysis software FAMOS 5.0 (imc Meßsysteme GmbH, Berlin, Germany).

6.4 Preparation

6.4.1 Femoral and tibial assembly preparation

A composite femur was sawed almost in half, and the portion with the distal-end was rigidly cemented in a block measuring 96×92×73 mm. Care was taken to ensure that the femur was aligned appropriately as the cement solidified. The visible femur portion measured about 100 mm in length. The femoral condyles were osteotomised to fit the inner profile of the Duracon implant (given in Figure 6.10). To facilitate implantation, polymethyl methacrylate (PMMA) was used as a cementing material. PMMA is the most widely used polymer biomaterial to cement prosthetic implants with bone in joint replacement surgeries [161, 202].

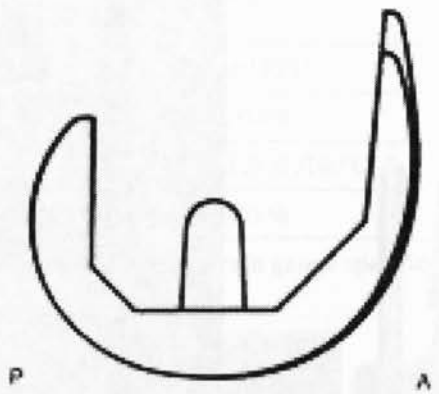

Figure 6.10 Profile of the Duracon system femoral component showing anterior (A) and posterior (P) sides [203]

Figure 6.11 shows the setup of the femoral component, and the rigid cementing of the femur in the cement block. The strain gauges were oriented along the femoral long axis, numbered as indicated in Figure 6.11. Four strain gauges were mounted on the posterior face (shown later in Figure 6.11c), one on each condylar surface of the implant, one in the middle of the metaphyseal region, and another further towards the diaphysis of the femur. Two were mounted on the anterior side: one in the diaphyseal region of the simulated bone, and one on the intercondylar region of the anterior femoral implant (both shown in Figure 6.11a). One strain gauge each was mounted on the lateral and medial side as indicated in Figure 6.11b and Figure 6.11d, respectively.

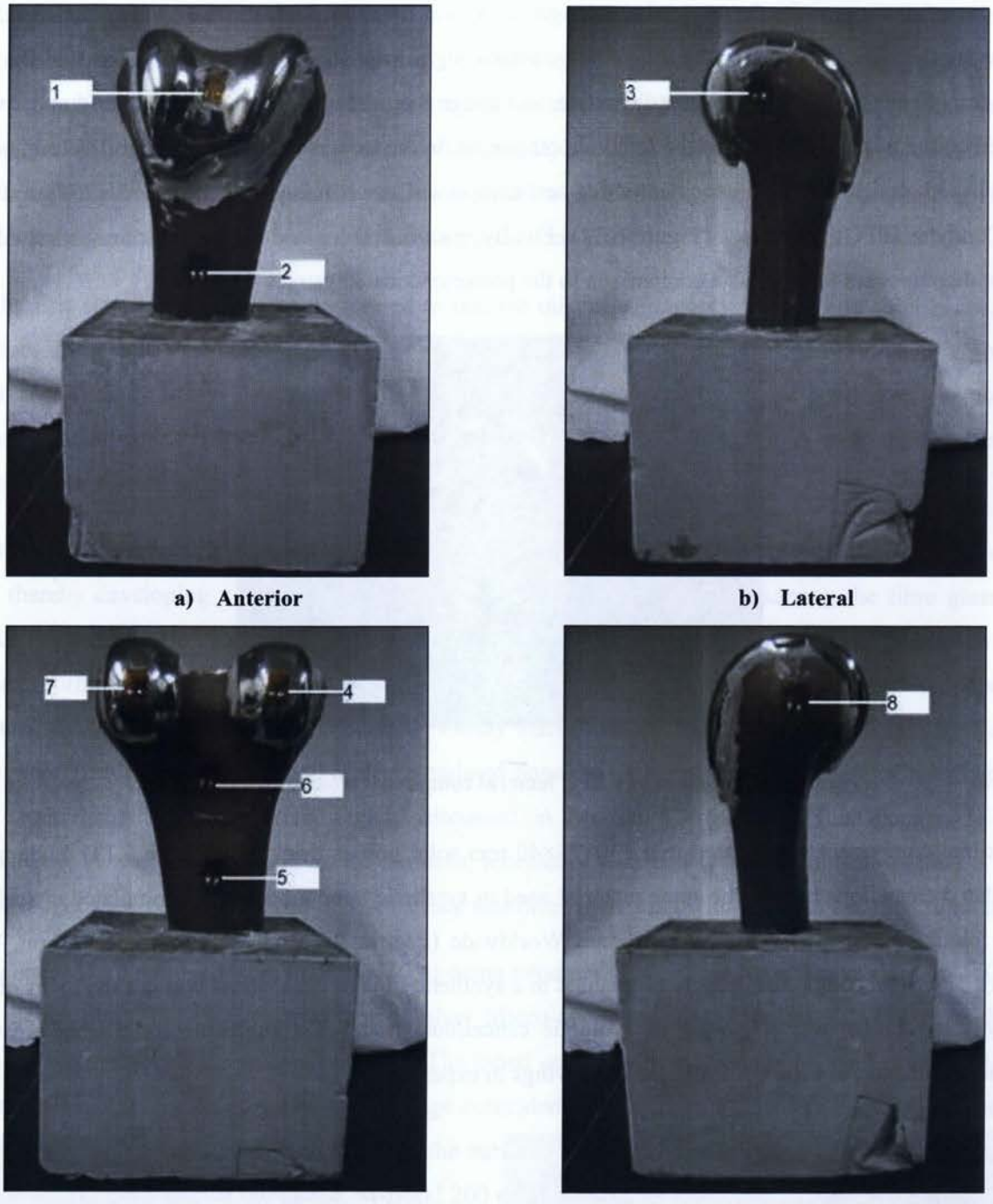

a) Anterior b) Lateral

c) Posterior d) Medial

Figure 6.11 Left femur setup showing strain gauge locations in the bone-implant system rigidly fixed in a cement block

The gauge locations were chosen based on two considerations: (1) highest possibility of measurable strain distribution, and (2) known critical locations of possible failure based on published studies. Considering the femoral setup geometry, an applied compressive load on the femur would produce a bending moment in the anterior-posterior direction. As such, significant strain was expected in the anterior and posterior

surfaces of the composite femur – where gauges 2, 5, and 6 are located. As the condyles of the distal femur are the closest regions to the articulating surface, significant strain is also expected on the condylar surfaces – hence gauge 3 on the lateral condyle, and gauge 8 on the medial condyle. Gauges 4 and 7 were placed on the posterior flanges of the femoral component, in the location possibly prone to fracture, as per a published clinical study on uncemented femoral component survivorship by Duffy *et al.* [204] on Press Fit Condylar (PFC) prostheses (Figure 6.12). Finally, gauge 1 is located in the anterior surface of the femoral component to serve as a comparison to the posterior-located gauges 4 and 7.

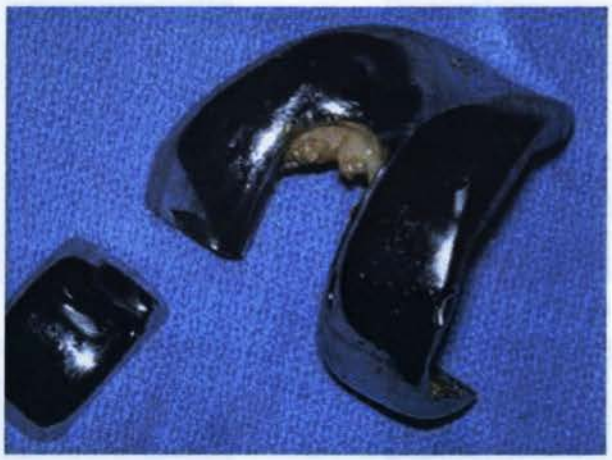

Figure 6.12 Fracture of a PFC femoral component from Duffy *et al.* [204]

The tibial component was fixated in a 130×78×40 mm solid porous brick (see Figure 6.13) made up of simulated cancellous bone – the same material used in synthetic bone models. This simulated cancellous bone block was also supplied by Sawbones Worldwide (Pacific Research Laboratories, Vashon, WA, USA). The tibial component was not implanted in a synthetic tibia as tibial stress was not the focus of this study. The choice to use a brick of synthetic cancellous tissue as a substitute for a tibia provided considerable experimental convenience and savings in expenses.

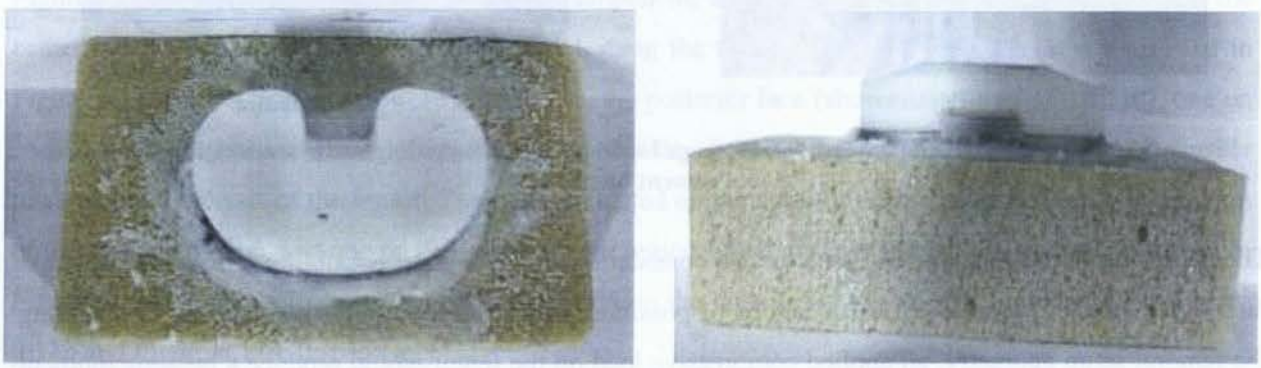

Figure 6.13 Superior (left) and anterior (right) view of the tibial components implanted in a brick of synthetic cancellous bone tissue

6.4.2 Strain gauge installation

The application of strain gauges, or 'gauging', involves a strict protocol in preparing the gauge and test surface to ensure proper bonding. Surface preparation is required (1) to ensure a chemically clean surface having an ideal roughness for strain gauge application, (2) to obtain a neutral surface pH of around 7, and (3) to draw visible layout lines on the surface to locate and orient the strain gauge. Surface preparation was done as per the strain gauge manufacturer's instructions [205].

As the first step, degreasing was performed to remove oils, organic contaminants, and soluble chemical residues from each test location. The femoral and implant surfaces were degreased using CSM-1A Degreaser (Vishay Micro-Measurements, Raleigh, NC, USA). The aerosol type applicator was used to ensure contaminants could not enter the degreaser container. Wiping was done with sterilised cotton gauze, in one direction only so that contaminants are not re-applied.

Next, the surfaces were abraded to remove debris and any loosely bonded adherents such as rust, scale, etc., thereby developing a surface texture suitable for gauge bonding. Considering the fibre glass and epoxy make-up of the synthetic femur, a 320-grit silicon carbide paper was used for dry abrasion. The implant surfaces were dry abraded, followed by final abrading using 320-grit silicon carbide paper on surfaces wetted with M-Prep Conditioner A (Vishay Micro-Measurements, Raleigh, NC, USA). Layout lines were burnished using a pencil on the simulated bone, and a ballpoint pen on the CoCrMo implant. The strain gauge locations were already discussed in Section 6.3 (p.53) of this chapter. M-Prep Conditioner A was applied again on the surfaces, repeatedly with cotton tipped applicators until a fresh tip no longer showed any traces on it. The surface was dried by wiping with gauze in one direction only.

The gauges were removed from their envelopes using tweezers. The gauges were then centred on 100-150 mm pieces of PCT-2A cellophane tape (Vishay Micro-Measurements, Raleigh, NC, USA), with the outside-facing sides of the gauges taped on. The taped gauges were positioned on the test surface such that the triangular alignment marks on the gauge coincided with the layout lines. For each gauge, one end of the tape was allowed to remain stuck to the surface, while another end was slowly pulled back to expose the bonding side of the gauge. M-Bond 200 catalyst (Vishay Micro-Measurements, Raleigh, NC, USA) was applied to the bonding side of the gauge, followed by a careful application of a few drops of M-Bond 200 (Vishay Micro-Measurements, Raleigh, NC, USA) at the junction of the tape and the test surface, as per the manufacturer's instructions [205]. The tape was then rotated back while held taut, and the gauge was carefully replaced over the layout lines by one firm stroke on the outer surface using gauze to attach the gauge/tape assembly on the test surface. Firm thumb pressure was applied on the gauge for at

least a minute to ensure that the M-Bond 200 adhesive bonded well. The tape was left on the gauge until it was time to wire the gauge.

6.4.3 Data acquisition and Signal analysis

Insulated, three-conductor, stranded tinned-copper lead wiring was used to connect the strain gauges to the CRONOS-PL data acquisition unit (imc Meßsysteme GmbH, Berlin, Germany). The three conductors of the wiring were colour coded (black, white and red). The conductors were separated, and each was stripped of at least half an inch of insulation. The black and white parts of the wiring were entwined and soldered onto one strain gauge terminal, and the red part of the wiring was soldered to the other terminal. This procedure was repeated for all eight strain gauges.

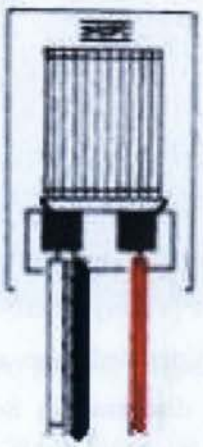

Figure 6.14 Three lead wire conductors separated and soldered to a strain gauge

The three-wire attachment to the strain gauge is part of the quarter bridge circuit as shown in Figure 6.15b. As opposed to a two-wire connection shown in Figure 6.15a, a three-wire circuit is always recommended for static experiments – since this greatly reduces the effect of lead wire resistance (R_L) in the static strain gauge readings [197].

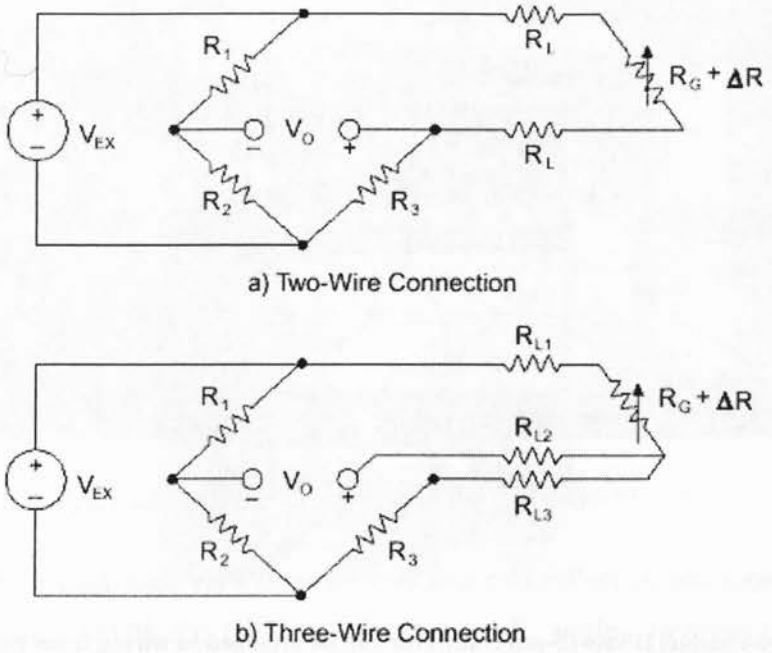

Figure 6.15 Illustration of circuit options to connect a strain gauge to the quarter bridge circuit [197]

Wiring from every two strain gauges was connected to one DSub-15-pin connector (ACC/DSUB-UNI2, imc Meßsysteme GmbH, Berlin, Germany) shown in Figure 6.16. A DSub-15 connector provides two channels that can connect with the CRONOS-PL data acquisition unit through a UNI2-8 eight-channel amplifier. This completes the Wheatstone bridge for strain measurements. Both the connector, and the amplifier are provided by the supplier of the CRONOS-PL unit. The gauge wiring connects to a DSub-15 thus: The connector has several labelled 'slots' into which the wiring from the gauges can be inserted (see Figure 6.16). First the free end of the colour-coded lead wire running from a strain gage is separated into three separate wires, and around half an inch of the insulation is stripped from each coloured connector wire. The red wire connects to the +VB1 slot (note that there are two slots for each label, e.g. +VB1 and +VB2, each representing one channel of the bi-channel connector). The black wire connects to I1_1/4B1. A small piece of free wire (not from the strain gauge) is inserted to the SENSE1 slot, and the other end of this free wire is entwined with the white wire from the strain gauge and inserted into +IN1. This completes the quarter bridge for one strain gauge.

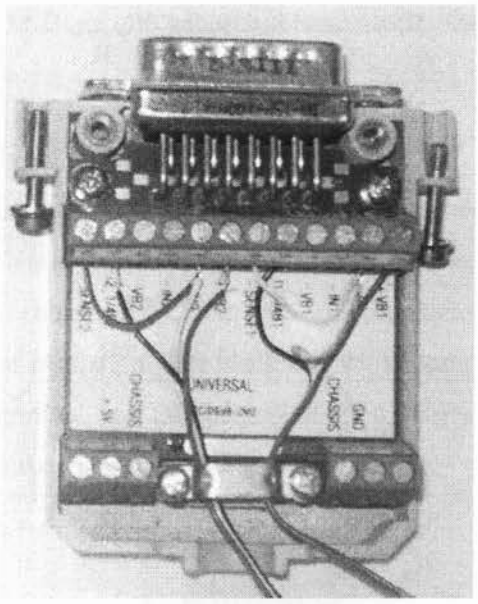

Figure 6.16 A two-channel DSub-15-pin connector can be attached to wiring from two strain gauges

The same procedure follows for each strain gauge, thereby connecting the wiring from every two gauges to one DSub-15 connector (four connectors required in total). The CRONOS-PL is outfitted with a UNI2-8 eight-channel amplifier (imc Meßsysteme GmbH, Berlin, Germany) installed in one of its posterior slots, which serves as the interface to connect the four DSub-15 connectors.

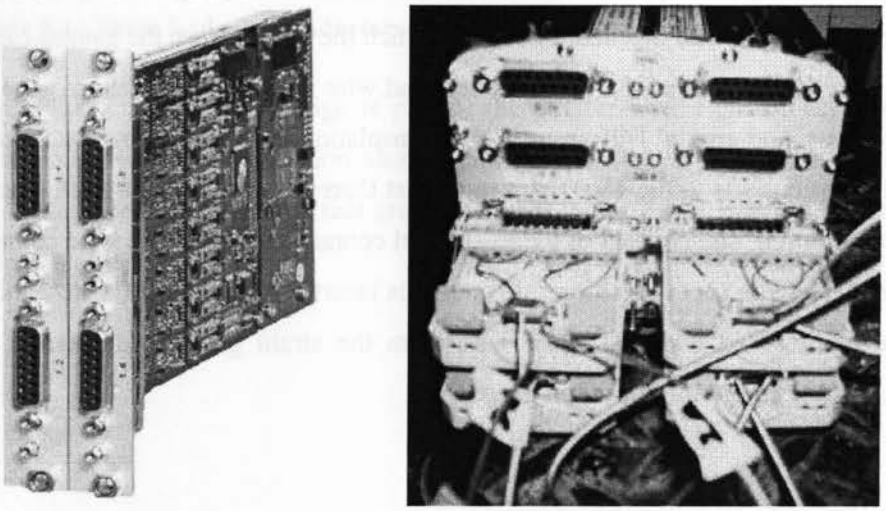

6.17 UNI2-8 all-purpose eight-channel amplifier (left, from [206]) is installed in the CRONOS-PL unit to accept the four DSub-15 connectors (right)

Figure 6.18 DSub-15s connected to the CRONOS-PL unit

The CRONOS-PL unit is connected via a LAN network to a data collection notebook computer running signal analysis software FAMOS 5.0 (imc Meßsysteme GmbH, Berlin, Germany). The strain gauge setting in FAMOS 5.0 was configured to the quarter bridge option, and a supply of 5 Volts was selected. The gauge factor and resistance was set to the manufacturer's specifications of 2.12 and 350 Ω, respectively. The sampling frequency was set to 1.0 millisecond. All strain gauge circuits were balanced using a built-in option provided in FAMOS 5.0. The measured strains from all strain gauges as displayed in microstrain (με) plotted against time.

6.5 Setup and alignment

The experimental setup simulated the left knee joint in zero-degree flexion (upright standing, unbent knee). The femoral and tibial component were setup as shown in Figure 6.19 – instead of having the femoral component press down on the tibial one (as it is in reality), the femoral component was held rigidly, and the tibial component was pressed on top of it by the actuator. The femoral assembly was fixated firmly with a vice on the baseplate of the Instron 8874. The tibial assembly was fastened to the actuator using two C-clamps.

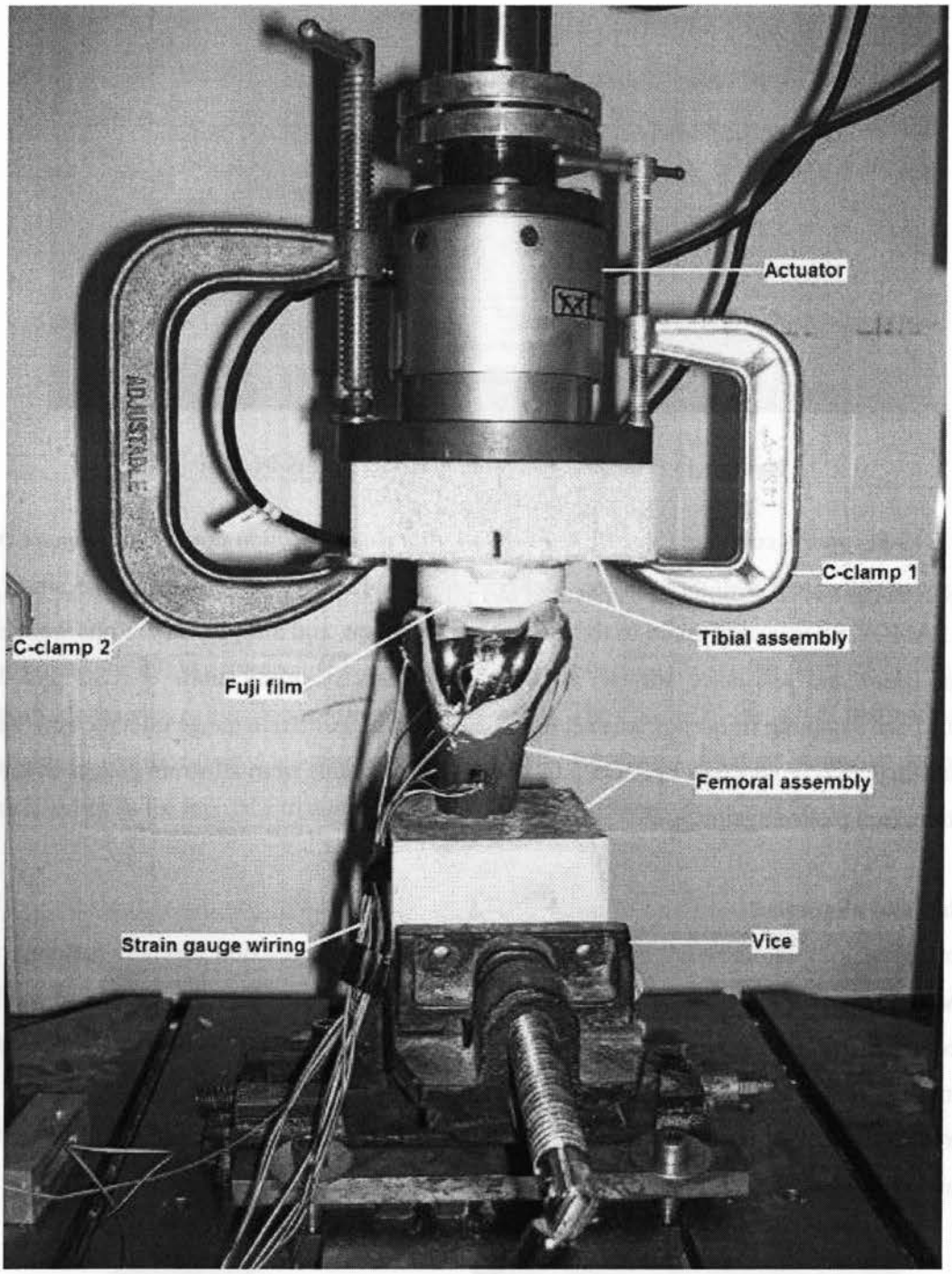

Figure 6.19 Experimental setup

6.5.1 Medial-lateral alignment

To obtain reliable results, it is important to ensure that the components are aligned – that the femoral and tibial component surfaces come into contact correctly to mimic *in vivo* physiologic contact. The importance of correct alignment in *in vitro* biomechanical testing was shown in a study by Liau *et al.*

[207]. Initially, when clamping the femoral and tibial assemblies, care was taken in aligning them to contact as accurately as possible by trial and error. Due to the concave conforming profile of the tibial UHMWPE surface, medial-lateral alignment was a simple task of fitting the convex femoral condyles in the tibial surface depressions (see Figure 6.20).

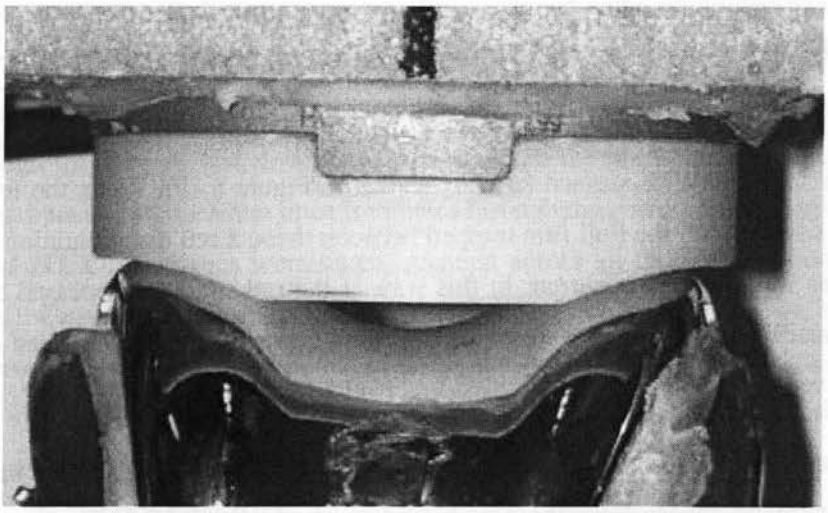

Figure 6.20 Close-up showing the relative ease of medial-lateral alignment due to the complementary tibial (concave) and femoral (convex) surfaces

6.5.2 Anterior-posterior alignment using Fuji Prescale™ Film

In the anterior-posterior direction, correct alignment was verified by testing for the contact location using pressure sensitive Fuji Prescale™ film (Low pressure grade, two-sheet type, FUJIFILM NDT Systems, Inc., Hanover Park, IL, USA). Fuji film is a widely used pressure sensitive material in contact analyses in knee joints [144, 181, 182, 207, 208], measuring about 0.2 mm in total thickness for both layers. The two-sheet type Fuji film (shown in Figure 6.21) is composed of an A-film, which is coated with a micro-encapsulated colour-forming material, and a C-film, which is coated with a colour-developing material. Both A and C films have a polyester base on which the colour forming and colour developing material is present. When pressure is applied, the microcapsules are broken and the colour-forming material that is released reacts with the colour-developing material to generate a red colour. The microcapsules are designed to react to various degrees of pressure, releasing their colour-forming material at a density that corresponds to the pressure [209].

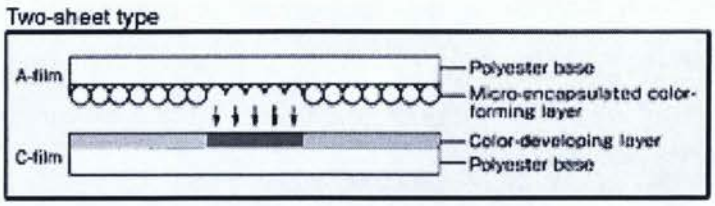

Figure 6.21 Two-sheet type pressure sensitive Fuji Prescale™ film [209]

Fuji film strips were cut out to in the shape of the tibial surface profile, and were taped to the femoral condyles and the tibial UHMWPE surface (already shown in Figure 6.19). When the femoral and tibial surfaces came into contact with the Fuji film trapped between them, a red discolouration appeared on the film in the locations were contact occurred. In this way, if the red smudges appeared to be dislocated, adjustments were made until the discoloured area appeared correctly aligned. Images of the Fuji film discoloration are given in the 'Results and Discussion' chapter (Section 9.1.1, p.92).

While Liau and colleagues [181, 182] showed that the Fuji film discoloration area may overestimate contact area in tibiofemoral experiments, there is no evidence in the literature indicating any effect on the load transfer between the femoral and tibial surfaces when Fuji film is placed between them. Given the relative softness of the polyester-based Fuji film strips compared to the CoCrMo femoral compnent and UHMWPE tibial bearing [182], and the low relative thickness (0.2 mm), there is no indication that their presence will affect the strain gauge readings – especially under loads of 2000-3000 N.

6.6 Methodology

Two load cases were tested; 2000 N and 3000 N. Using the software interface of the FastTrack 8800, loading rate was set to 100 N/s, followed by a maximum force hold time of 90 seconds. As mentioned earlier, in addition to controlling the loading rate and maximum load, the FastTrack 2 software also obtained feedback from the actuator on its displacement every 0.01 second. The data of actual applied load over time on the test specimens could then be plotted. The actuator applied compressive loads up to the preset maximum of 2000 N or 3000 N, which was then held in place for 90 seconds. This was done so that strain measurements were obtained for a duration of 90 seconds under maximum load. After this the actuator lifted and released pressure on the test assembly. Meanwhile, the FAMOS 5.0 software generated plots of the strain measurements, which were then saved for analysis. The Fuji film strips were analysed to confirm that satisfactory contact occurred. At least 3 runs were conducted for each loading case, and the strain readings for each reading was averaged over the 3 runs. The results are discussed later in Section 9.1, p.92. Representative load-displacement curves for the bone-implant system for both load cases are given in Appendix A, p.115.

7 GEOMETRY MODELLING

7.1 Femur

The fourth generation composite femur model was fully scanned using computed tomography (CT). CT scanning is a non-desctructive imaging technique, whereby focused X-ray beams are projected on the target object. Detectors situated around the test subject measure the instensity of these beams once they have passed through the subject, and develop an image where the pixel intensity of a region is directly proportional to the intensity of the beam once it radiates through the corresponding location on the subject [210]. A series of 2D X-ray images were taken, scanned across all three of the body planes (coronal, sagittal, and axial). Cross sectional images across each plane (such as those shown in Figure 7.1) were thus obtained at every 0.5 mm along the length of the femur model. A total of 789 images were obtained. The images are stored in the DICOM format (Digital Imaging and Communications in Medicine). 'Stacking' these cross sectional images reveals a complete 3D internal and external geometry. The cross section images in the DICOM format were imported into Mimics® Medical Imaging Software (The Materialise Group, Leuven, Belgium), which can produce a 3D image from the CT images.

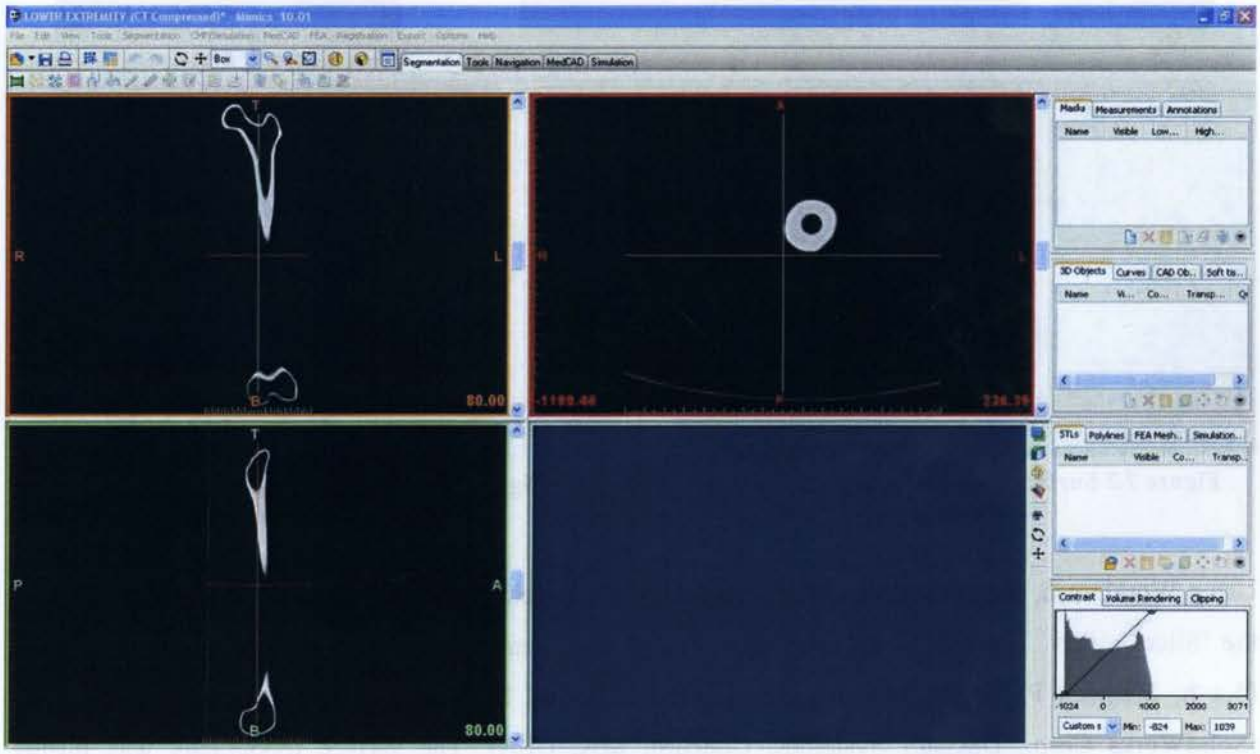

Figure 7.1 Mimics™ screenshot showing CT images in the coronal, axial, and sagittal planes (clockwise from top left) at a particular point location on the femur

Mimics was used for image segmentation, whereby each image 'slice' was stacked according to shared boundaries between bones and cavities. A connectivity algorithm ensured that the geometry of adjacent slices were free of discontinuities, and a subsequent 3D model was developed. The model is then saved in its triangulated surface geometry version as an STL (*.stl, stereolithography) file. The file contained geometry data for both the outer cortical layer and inner cancellous bone surfaces. The model was imported into Geomagic Studio (Geomagic, Inc., Research Triangle Parck, NC, USA), where the polygon surface model was optimised. The model contained a few 'holes' or cavities in places where the CT scanning or the subsequent segmentation phase could not obtain sufficient surface detail (shown in Figure 7.2). These holes were manually healed on both cortical and cancellous surfaces (external and internal surfaces).

At this point, the surfaces were rough, populated with small 'ridges and bumps', visible in Figure 7.2. Surface smoothening was performed in the software by alternately using a 'Relaxation' utility and an inbuilt surface curvature curing algorithm, which resulted in an improvement in the surface finish. Surface grid patterns were generated (Figure 7.3) and checked for errors which were corrected. The model was then saved as an IGES (*.igs, Initial Graphics Exchange Specification), and imported into ANSYS Workbench 11.0 (ANSYS, Inc., Canonsburg, PA, USA).

Figure 7.2 Surface roughness, and cavity in the geometry

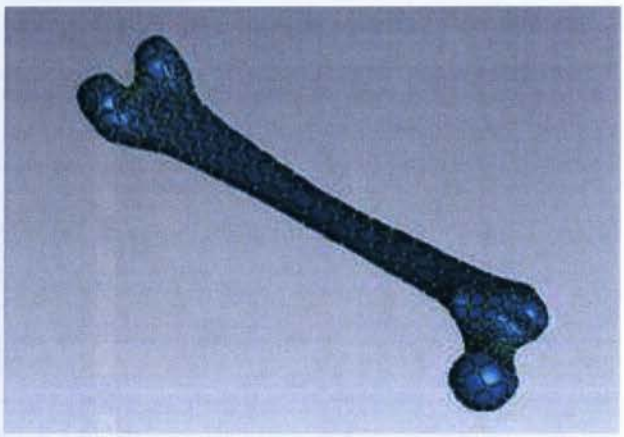

Figure 7.3 Grid generated and improved

Using Workbench, the cortical-cancellous geometry was processed to produce two separate solids using the 'Slice' utility. The compound solid thus created was then exported in the Parasolid Binary format (*.x_b; Siemens PLM Software, Siemens AG, Berlin and Munich, Germany) to SolidWorks 2008 (SolidWorks Corp., Dassault Systèmes, Concord, MA, USA). The surface topography was further improved in SolidWorks. The final femur geometry (Figure 7.4) was then cut slightly below the diaphysis midsection, and the condyles were resected (as shown in Figure 7.5) to conform to the implant surface. As

the following sections describe, the implant geometries were also developed using SolidWorks. The implant components and the bone geometry were assembled to replicate the experimental setup, and exported to ANSYS Workbench for finite element analysis.

Figure 7.4 Full femur final CAD model

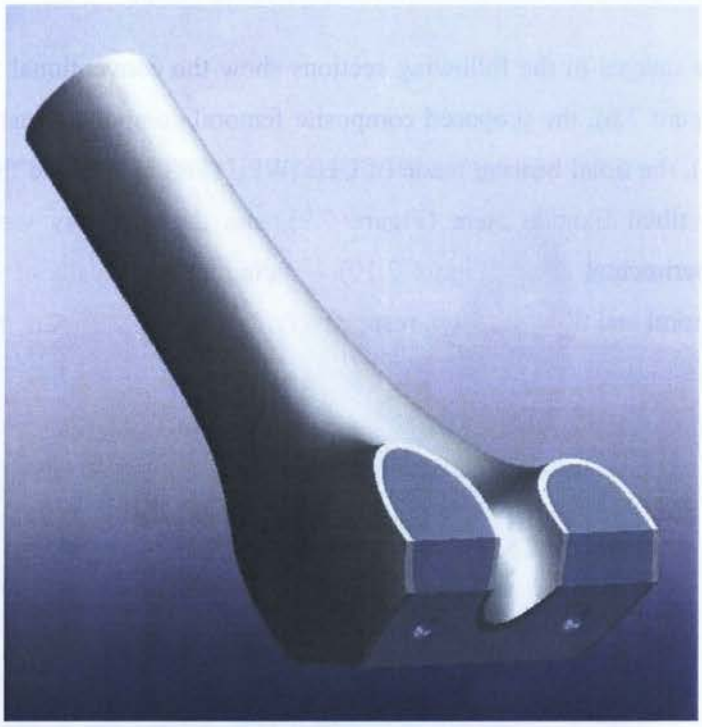

Figure 7.5 Resected distal femur showing cancellous (darker core) and cortical (lighter outer layer) tissue

7.2 Implant components

The implant components were developed via the CAD software SolidWorks, and were designed to imitate the commercial Duracon knee implant system (Stryker Corp., Kalamazoo, MI, USA) used in the experimental portion of this study. Models of the femoral and tibial components were created to scale, and assembled exactly as in the experimental setup.

The images in the following sections show the conventional femoral component of the Duracon design (Figure 7.6), the proposed composite femoral component that incorporates a layer of CF/PA-12 (Figure 7.7), the tibial bearing made of UHMWPE (Figure 7.8) and the metal tray on which it rests (Figure 7.9), the tibial fixation stem (Figure 7.9), and the assembly view of all the components as used in the experimental setup (Figure 7.10) – including the blocks of cement and synthetic cancellous bone for femoral and tibial fixation, respectively.

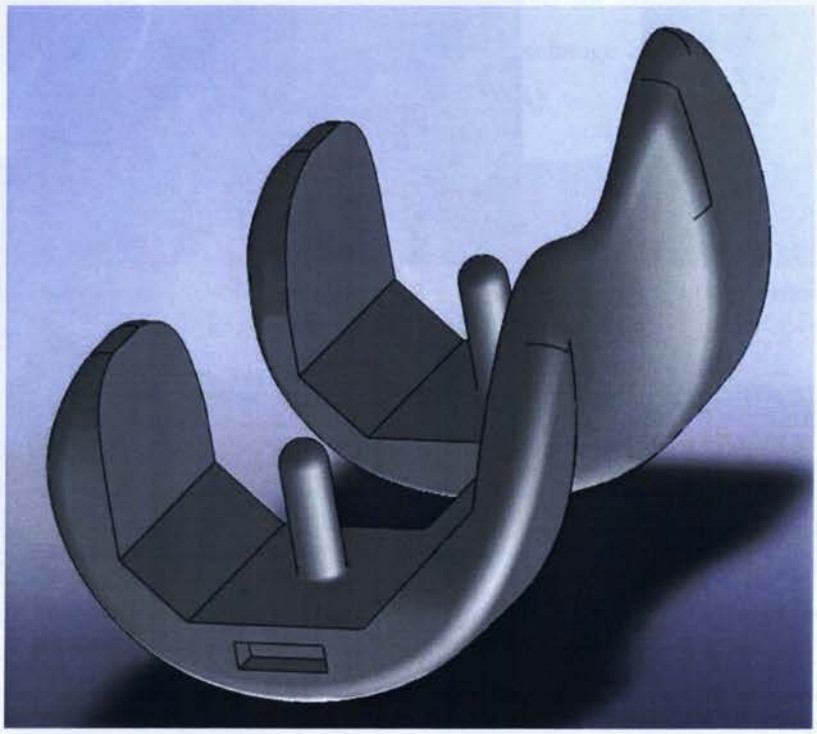

Figure 7.6 Femoral component CAD model

The approach of this thesis study will be to develop a nearly isoelastic implant design for the distal femur along the lines of those attempted in hip arthroplasty – specifically, a design that will incorporate a lining

of biomimetic carbon-polymer composite around a conventional metallic implant (cobalt-based alloy) as an interface with the adjacent bone tissue. The proposed carbon-polymer composite is a polyamide 12 matrix reinforced by carbon fibres, (discussed earlier in detail in Sections 4.4.2 and 4.5, p.38 and p.42, respectively). The hybrid implant is envisaged to constitute a 3 mm-thick shell of CoCrMo alloy enclosing a CF/PA12 layer moulded for a good fit. The overall outer dimensions are meant to be exactly the same as the conventional design.

Figure 7.7 Exploded view of the hybrid femoral component, showing the CF/PA12 layer

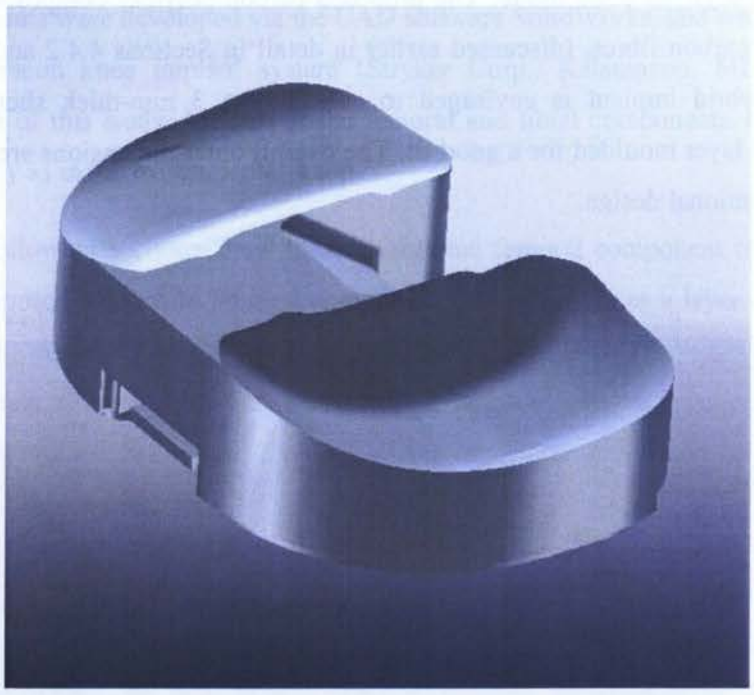

Figure 7.8 UHMWPE tibial bearing CAD model

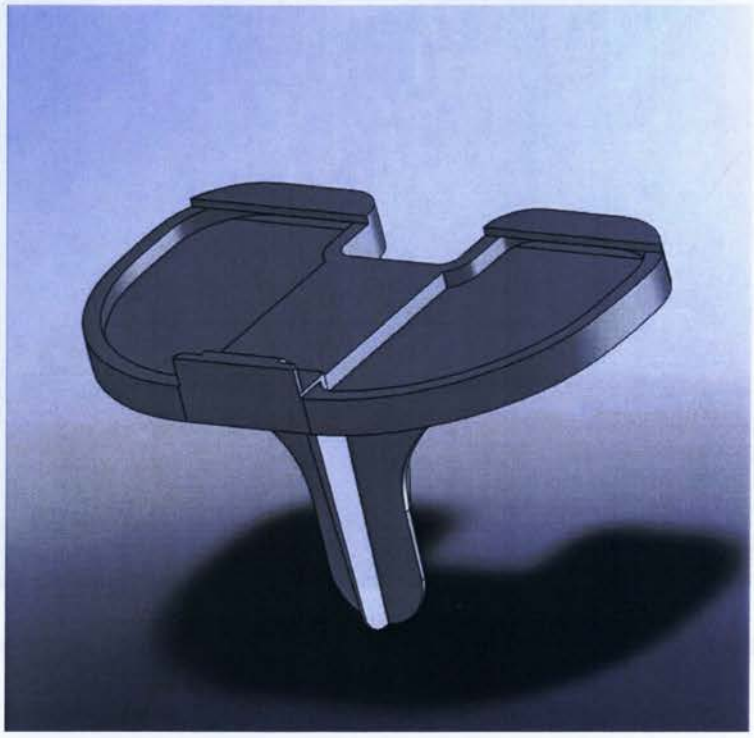

Figure 7.9 Tibial tray and fixation stem CAD model

Figure 7.10 displays an exploded view of the experimental assembly recreated via CAD. This particular assembly is for the conventional implant. The overall assembly using the hybrid implant is similar, except that there is an additional part body – the CF/PA12 layer. The assembly was exported to ANSYS Workbench 11.0 for finite element analysis.

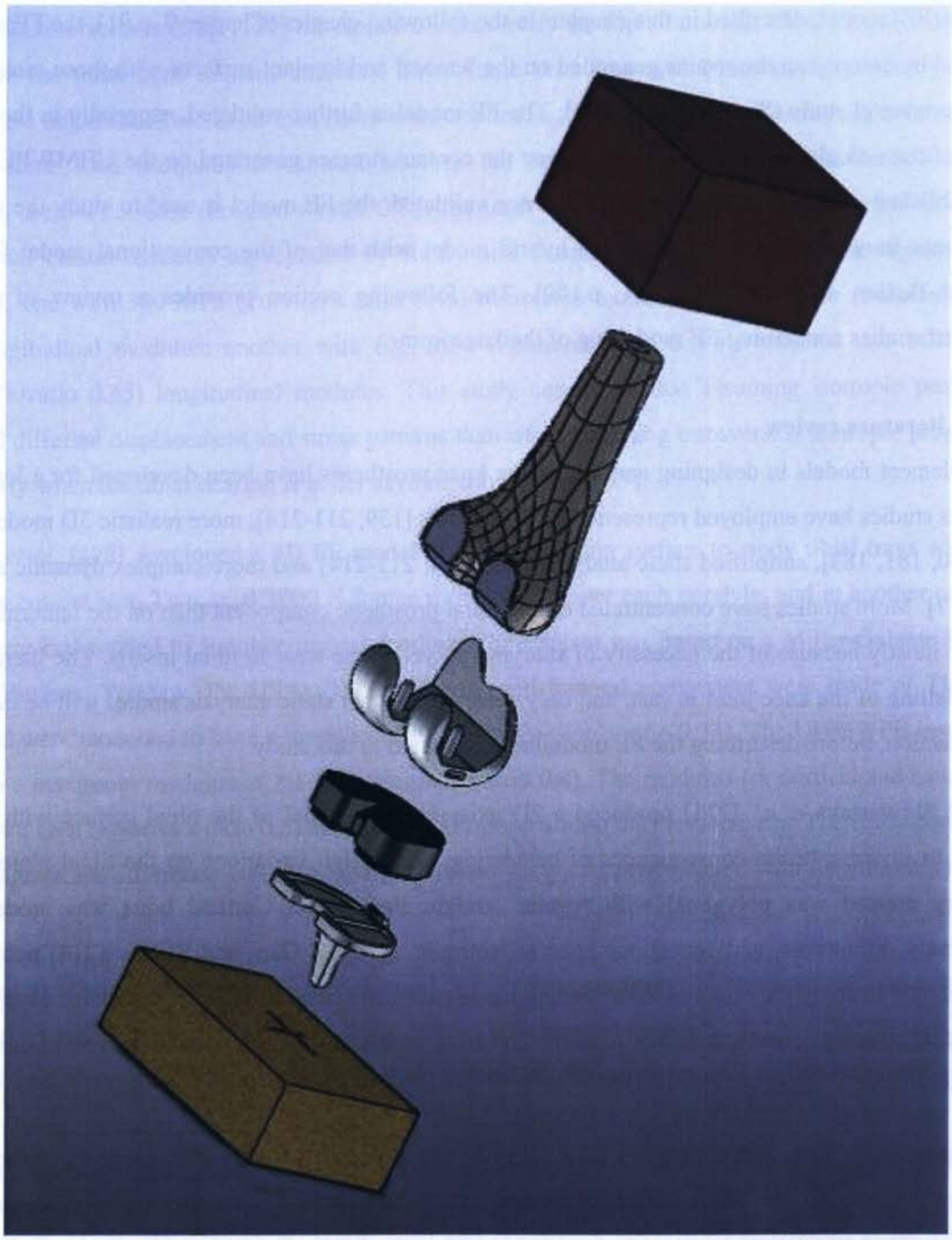

Figure 7.10 Exploded view of the conventional bone-implant assembly

8 FINITE ELEMENT MODELLING

8.1 Overview

The geometry modelled and assembled as described in the previous section was used to develop a finite element (FE) model, described in this chapter. In the following chapter (Chapter 9, p.91), the FE model is validated by comparing the strains generated on the femoral and implant surfaces with those measured in the experimental study (Section 9.3.1, p.95). The FE model is further validated, especially in the contact region of the articulating surface, by comparing the contact stresses generated on the UHMWPE surface with published studies (Section 9.3.2, p.99). Once validated, the FE model is used to study the implant-bone stress transfer characterisitics of the hybrid model with that of the conventional model for three different flexion angles (Section 9.4, p.100). The following section provides a review of relevant published studies concerning FE modelling of the knee joint.

8.2 Literature review

Finite element models in designing and improving knee prostheses have been developed for a long time. Previous studies have employed representative 2D models [139, 211-214], more realistic 3D models [144, 162, 180, 181, 183], simplified static analyses [139, 178, 211-214] and more complex dynamic analyses [215-217]. More studies have concentrated on the tibial prosthetic component than on the femoral portion – this is mostly because of the necessity of studying polyethylene wear in tibial inserts. The literature on FE modelling of the knee joint is vast, and only selected relevant static analysis studies will be discussed in this section, before describing the FE modelling conducted in this study.

In 1982 Shrivastava *et al.* [211] produced a 2D axisymmetric model of the tibial surface with Fourier loading to investigate the consequences of cementing, and design variations on the tibial plateau. The geometry created was polygonal with regular straight line edges. Cortical bone was modelled as transversely orthotropic, and cancellous bone as isotropic. In 1986, Garg and Walker [214] published a 2D FE model to study the effect of axial loading mode (from 100 N up to 2500 N distributed over varying lengths) on stresses beneath the tibial plateau. The bone modulus was modelled to vary with the density as measured by CT scans.

In the same year, Vasu and colleagues [212, 213] developed models of tibial components in the frontal and sagittal planes to analyse the effect of loading and prosthesis design features on interface and bone stresses. Instead of a 3D model, two 2D models (one for each plane) of well representative geometry were developed. Axial load cases were based on "three times body weight" equivalent of 2000 N. Bone

properties were varied in different 'regions' in the model, with elastic modulus ranging from 100 MPa (Poisson's ratio 0.18) in cancellous areas to 5 GPa (Poisson's ratio 0.31) in cortical regions. The polyethylene tibial bearing was assigned a modulus of 500 MPa (Poisson's ratio 0.4), and the CoCrMo alloy material was modelled with an elastic modulus of 200 GPa (Poisson's ratio 0.29). [212, 213]

In 1992, Rakotomanana *et al.* [139] developed a transversely isotropic bone 2D FE model to study load transfer in the tibial bone-implant interface. Since static behaviour was being studied, bone viscosity effects were neglected. Two axial load cases were applied; a 2000 N distributed evenly on the condyles, and the same load unequally distributed between the condyles. Cortical bone transverse isotropic properties were 11.5 GPa (Poisson's ratio 0.58) for transverse and 17 GPa (Poisson's ratio 0.46) for longitudinal elastic modulus as reported by Reilly and Burstein [74]. Two cancellous regions were modelled, one with 300 MPa (Poisson's ratio 0.45) transverse modulus and 900 MPa (Poisson's ratio 0.53) longitudinal modulus; another with 630 MPa (Poisson's ratio 0.39) transverse and 1100 MPa (Poisson's ratio 0.35) longitudinal modulus. This study concluded that assuming isotropic properties produced different displacement and stress patterns than when assuming transversely isotropic properties, particularly when the tibial bearing is under asymmetric loading [139].

Miyoshi *et al.* [178] developed a 3D FE model of the articulating surface to study tibial trays with and without a cut-out slot. Two axial 1000 N forces were applied over each condyle, and in another case the forces were mal-rotated to simulate uneven loading. The implant was based on a Miller-Galante II knee system (Zimmer, Warsaw, IN, USA). The tibial base and femoral component were made of Titanium alloy, and were modelled to have a modulus of 112 GPa (Poisson's ratio 0.34). The UHMWPE insert was varied to a maximum modulus of 8.1 GPa (Poisson's ratio 0.4). The modulus for cortical and cancellous bone was 8 GPa (Poisson's ratio 0.3) and 1.5 GPa (Poisson's ratio 0.2) respectively. The study concluded that no significant difference was observed in tibial polyethylene performance with or without a cut-out slot.

Villa *et al.* [144] developed a 3D FE model based on a rotating platform tibial component, and conducted three contact and three fatigue tests. The static contact tests applied loads of 2200 N, 3200 N, and 2800 N at 15, 45, and 60 degrees knee flexion, respectively. The CoCrMo alloy femoral component and tibial tray had an elastic modulus of 200 GPa (Poisson's ratio 0.3), and the UHMWPE modulus was varied according to a power law (Poisson's ratio 0.45). No information is given on the modulus of bone tissue.

Godest *et al.* [179], Halloran *et al.* [180], Liau and colleagues [181-183], and Bartel *et al.* [162] all developed FE models where the femoral component was simply modelled as a rigid body. This was because their focus of study was the tibial component, and the metallic femoral component has a modulus

a few orders of magnitude higher than that of the tibial polyethylene component. None of them have reported their elastic modulus for bone tissue. Nearly all of these studies assumed a Poisson's ratio of 0.46 for UHMWPE material, with the modulus ranging from 0.50 to 1.016 GPa.

In 2009, Completo *et al.* [30] studied stress shielding generated in the fixation stems of tibial components after TKA using a finite element model developed from a CT scanned geometry of a synthetic tibia manufactured by Pacific Research Laboratories (model #3302, left tibia, Vashon, WA, USA). The idea is similar to that used in this study, except Completo *et al.* developed a proximal tibia model and the present study concerns the distal femur. Stress shielding and stress concentration related to end-of-stem pain were the subject of study for different tibial press-fit stem designs. Four configurations of the PFC Sigma (DePuy, Johnson & Johnson, Warsaw, IN, USA) tibial component were analysed – cemented, uncemented, CoCr or Ti-6Al-4V alloy, and tibial stem with 15 mm polyethylene tip. For each model a force of 1440 N and 880 N were applied on the medial and lateral condyles, respectively. The bone tissue and implant materials were all modelled to be linearly elastic, homogeneous and isotropic. The modulus of cancellous bone, cortical bone, CoCr alloy, and polyethylene was 104 MPa, 14.2 GPa, 210 GPa, and 500 MPa, respectively. Coulomb friction model was applied, and the coefficient of friction (μ) between the bone tissue and the implant was 0.3, whereas between bone tissue and PMMA cement was 0.25. All materials were assumed to have a Poisson's ratio of 0.3. Stress concentrations were determined considering the relative minimal principal stress in the cancellous bone between an implanted tibia and an intact tibia under the same load. The results indicated that long stems induced pain-causing high stress concentrations in the distal tibia, which could be theoretically reduced by the using a flexible polymeric tip.

As already mentioned, majority of the FE models in literature have been generated to study tibial components and tibial bone tissue, and there is comparatively little work done on femoral component stress analysis. To the author's knowledge, there has not been any study on femoral surface strains that may serve as a relevant comparison to the FEA conducted in this study. Therefore most of the validation will be conducted by comparing the experimental study with the FE results, and comparing stresses generated in the tibial UHMWPE component with published work. The following sections in this chapter will describe the FEA conducted for this study.

8.3 Material properties

Since published literature tends to have some variety in modelled material properties for the same components, a short commentary is given for each material describing the reasoning and validity of the

material properties chosen. Note that for materials modelled to be isotropic, the shear modulus is calculated from the relation,

$$G = \frac{E}{2(1+\nu)}$$ **Equation 8.1**

where G is shear modulus of the isotropic material, E is elastic modulus, and ν is Poisson's ratio.

8.3.1 Synthetic analogue bone models

As discussed in Section 3.4.2 (p.18), experimental investigations in the past have shown that cortical bones can be assumed to possess transverse isotropy at the continuum level, as shown by Reilly *et al.* [75, 186], while the cancellous spongy bone may be assumed to have orthotropic symmetry as considered by Williams *et al.* [91], Turner *et al.* [218], Ashman *et al.* [95]. However, since the experimental study was conducted using synthetic bone which possesses linear elastic behaviour at the continuum level [111], the elastic properties used are those of the manufacturer. Other properties applied in this study have been taken from the manufacturer's properties of synthetic composite models (listed in Section 3.5.1, p.23), and previous studies that used synthetic bones [42, 175] (indicated in the footnotes).

These simplifications are not without precedent. Both types of simulated bone have been modelled as linear elastic homogeneous materials in several studies [106, 107, 114, 175], with some studies modelling the cortical bone as transversely isotropic [42, 139]. These simplifications serve three reasons: (1) the goal of this study is to obtain a comparative understanding of bone-implant systems, as opposed to studying the absolute performance of bone tissue, (2) the high degree of variance even within tissues of the same type in the same region makes it inconvenient and unnecessary to replicate for the scope of this study, and (3) to maintain comparability between the results of the current FE study, the experimental study, and other studies conducted using synthetic composite bones.

Property (units)	Simulated cortical bone	Simulated cancellous bone
Density (g/cc)	1.64[1]	0.27[1]
Elastic modulus (GPa)	16.7[1]	0.155[1]
Ultimate strength (MPa)	130[1]	6.0[1]
Poisson's ratio	0.46[2]	0.3[3]
Shear modulus (GPa)	5.72 (from Equation 8.1)	0.060 (from Equation 8.1)
Material elasticity model	Linear elastic[2,3]	Linear elastic[3]
Isotropy	Isotropic[3]	Isotropic[3]

Table 8.1 Simulated cortical and cancellous bone properties

8.3.2 CoCrMo alloy

The femoral component and the tibial fixation tray (stemmed tray) of the Duracon knee system are made of cobalt-chromium-molybdenum (CoCrMo) alloy [46]. CoCrMo alloys are cobalt based metal alloys, and the medical grade alloys frequently used in joint arthroplasty contain around 27-30% chromium and 5-7% molybdenum. The specifications for CoCrMo medical grade alloys (cast, wrought, and forged) are covered in the American Society for Testing and Materials (ASTM) standards F75, F799, and F1537, as reported by Kurtz [219].

As the exact properties of the CoCrMo alloy used in the Duracon system is not listed by the manufacturers, but it is expected to follow the ASTM standards for medical grade alloy closely. This study will use ASTM F1537 minimum specifications for wrought and warm worked CoCrMo medical grade alloys with a tensile yield strength of 827 MPa, and ultimate tensile strength of 1172 MPa (ultimate elongation of 12%), as reported by Kurtz [219]. The alloy density used is 8.28 g/cc, which is of the commercially available CoCrMo alloy BioDur® CCM Plus® (Carpenter Technology Corporation, Reading, PA) manufactured as per ASTM F1537 (28% chromium and 6% molybdenum) [220]. The Poisson's ratio used is 0.31, which is the same for all the individual constituent metals (cobalt, chromium, and molybdenum) [221]. The elastic modulus used is 210 GPa, which approximates those used in a previous FE knee implant studies [30, 35, 144], and in studies comparing CoCrMo alloys with other medical alloys [222, 223].

---

[1] Synthetic composite bone manufacturer's properties [111]

[2] Reilly and Burstein [74, 75]

[3] Bougherara and colleagues [42, 175]

Density [220]	8.28 g/cc
Elastic modulus [222, 223]	210 GPa
Yield strength [219]	827 MPa
Ultimate strength [219]	1172 MPa
Ultimate elongation (tensile) [219]	12%
Poisson's ratio [221]	0.31
Shear modulus	84 GPa (from Equation 8.1)
Elasticity model	Linear elastic, homogeneous
Isotropy	Isotropic

Table 8.2 Cobalt-chromium alloy properties

8.3.3 UHMWPE

Ultra high molecular weight polyethylene was introduced and discussed in Section 4.4.1, p.35. The density and strength information of the UHMWPE used in the Duracon system has been obtained from the manufacturer [171]. The elastic modulus of UHMWPE varies depending on the polymer crosslinking (or gamma ray sterilisation). Since the manufacturer did not indicate any information on the modulus, a value of 900 MPa for GUR-1050 resin, 30 kGy (kilogrey units) irradiated highly crosslinked UHMWPE is used (as reported by Kurtz *et al.* [164]). Published literature indicates that the most commonly used Poisson's ratio for UHMWPE is 0.45 [144] or 0.46 [181-183], but Bergström [165] noted that Poisson's ratio of UHMWPE in knee implant assemblies have only a weak influence on material response, and suggested that a value of 0.4 is quite sufficient.

Though true stress-strain curves of UHMWPE show that the material has a complex behavioiur under high strains in loading and unloading, Bergström reports that it is adequate to assume a linear elastic behaviour if the UHMWPE component is part of a larger system and its performance is not the specific focus of study (see Section 4.4.1). Also, the equivalent (von Mises) strain in the UHMWPE component under an applied load of 3000 N is expected to be around 0.05 – in which case the modulus behaviour has been shown to be approximately linear [130, 167]. This fact is clearly displayed by the strain distribution contours obtained after the FE simulation (see Appendix C, p.119).

Density [171]	0.9392 g/cc
Elastic modulus [164]	900 MPa
Yield strength [171]	23.2 MPa
Ultimate strength [171]	54.8 MPa
Poisson's ratio [165]	0.4
Shear modulus	321.43 MPa (from Equation 8.1)
Elasticity model [130, 167]	Linear elastic
Isotropy	Isotropic

Table 8.3 UHMWPE properties

8.3.4 CF/PA12

The manufacturing and compression testing of CF/PA12 was conducted by Campbell and colleagues [38-41], already described in Section 4.4.2, p.38. For FE modelling, the CF/PA12 layer is modelled to be isotropic but using the bulk compressive properties as tested and published reliably by Campbell *et al.* [41].

Density [38, 39]	1.43 g/cc
Bulk compressive modulus [41]	12.2 GPa
Bulk compressive ultimate strength [41]	155 MPa
Bulk flexural modulus (not used in FEA) [41]	16.4 GPa
Bulk flexural ultimate strength (not used in FEA) [41]	188 GPa
Poisson's ratio [42]	0.3
Elasticity model	Linear elastic
Isotropy	Isotropic, using bulk compressive modulus as elastic modulus

Table 8.4 CF/PA12 properties

8.3.5 Cement block

The femur model used in the experiment was osteotomised and rigidly fixed in a block of cement/concrete. While it is convenient to model the base of the femur to be rigidly constrained, such a model may not be able to reproduce the experimental measurements. To err on the safe side, the cement block was also modelled to be flexible with properties provided by the material library in the ANSYS Workbench software package itself.

Density	2.3 g/cc
Elastic modulus	30 GPa
Yield strength	0 MPa
Ultimate compressive strength	41 MPa
Poisson's ratio	0.18
Shear modulus	8.47 MPa (from Equation 8.1)
Elasticity model	Linear elastic
Isotropy	Isotropic

Table 8.5 Concrete properties[4]

8.3.6 Summary

Property (Units)	Simulated cortical bone	Simulated cancellous bone	CoCrMo	UHMWPE	CF/PA12	Cement block
Density (g/cc)	1.64	0.27	8.28	0.9392	1.43	2.3
Elastic modulus (GPa)	16.7	0.155	210	0.900	12.2	30
Poisson's ratio	0.46	0.3	0.31	0.4	0.3	0.18
Elasticity model	Linear elastic	Linear elastic	Linear elastic	Linear elastic	Linear elastic	Linear elastic
Isotropy	Isotropic	Isotropic	Isotropic	Isotropic	Isotropic, using bulk compressive modulus as elastic modulus	Isotropic

Table 8.6 Material properties used in the FE model of the bone-implant system

8.4 Finite elements

8.4.1 SOLID187 3-D 10-Node Tetrahedral Structural Solid

SOLID187 is a higher order 3D tetrahedral solid element included in ANSYS Workbench. All the solid bodies were modelled with this element. The element has 10 nodes, with three degrees of freedom at each node – translations in the nodal x, y, and z directions. SOLID187 has a quadratic displacement behaviour, and is well suited to modelling irregular meshes – such as those imported from CAD software. It is for

[4] Obtained from ANSYS® Workbench Release 11.0 material library

this particular reason that SOLID187 has been used to model the highly curvaceous geometry of the femur and implant components. Though not required for the purposes of this study, the reader is informed that this element also has plasticity, hyperelasticity, creep, stress stiffening, large deflection, and large strain capabilities. In addition, it has mixed formulation capability for simulating deformations of nearly incompressible elastoplastic materials, and fully incompressible hyperelastic materials. In the future, should the FE model of this study be used for further analysis which include the more complex material behaviour, this element would be ideal. The element input data includes the orthotropic or anisotropic material properties. Orthotropic and anisotropic material directions correspond to the element coordinate directions. The geometry, node locations, and the coordinate system for this element are shown in Figure 8.1. The element stress directions are parallel to the element coordinate system, shown in Figure 8.2. The surface stress outputs are in the surface coordinate system – as shown in Figure 8.2 for face JIK [224].

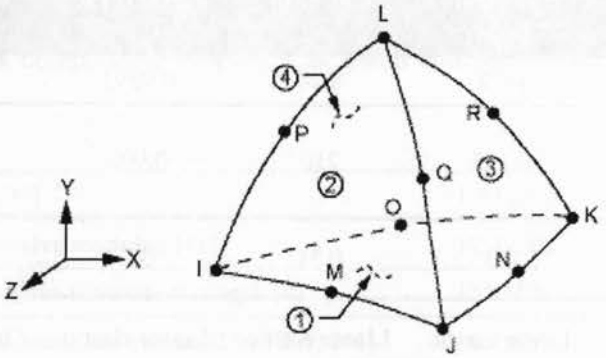

Figure 8.1 SOLID187 element description [224]

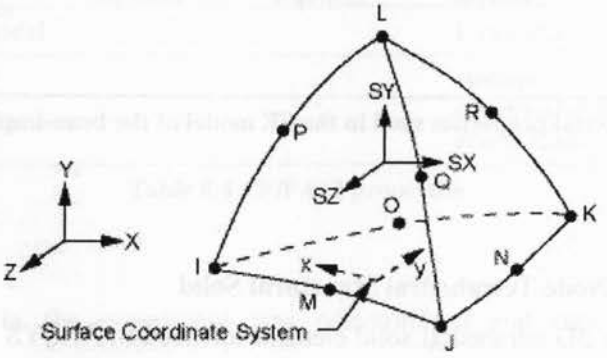

Figure 8.2 SOLID187 stress output directions [224]

8.4.2 CONTA174 3D 8-node Surface-to-surface contact

For flexible-flexible contact problems, such as that between the CoCrMo (E = 220 GPa) femoral implant and the tibial UHMWPE (E = 900 MPa), at least one of the deformable surfaces must be represented by a

contact element. CONTA174 is used in this study to model the contact between the tibial UHMWPE bearing and the CoCrMo femoral component. CONTA174 is a contact modelling element included in ANSYS. CONTA174 is usually located on a deformable surface (of a 3D solid or shell element) that contacts and slides on a target surface (in this study modelled by the TARGE170 element described in the next section). This element has three degrees of freedom at each node – translations in the nodal x, y, and z directions. It has the same geometric characteristics as the solid or shell element face with which it is connected. Contact occurs when the element surface penetrates a target element (such as TARGE170) on a specified target surface. The element geometry, node locations, and co-ordinate system is shown in Figure 8.3 [225].

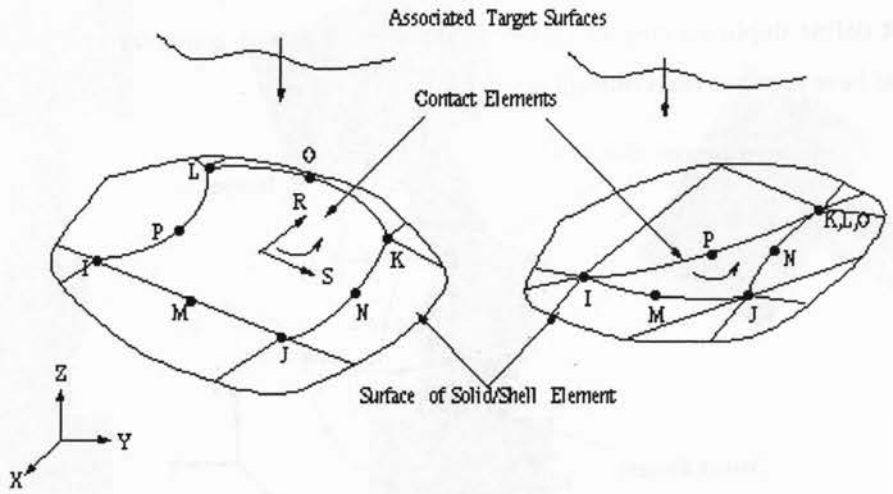

Figure 8.3 CONTA174 element description [225]

CONTA174 and the associated target element (e.g. TARGE170) share the same real constants. All contact elements in this study is set to be fully bonded, except for the contact between the femoral component and the UHMWPE surface which was simulated to be frictional (discussed later in Section 8.7, p.85). The only material property used for this element is the interface coefficient of friction for the Coulomb friction model.

8.4.3 TARGE170 3D Target segment

TARGE170 is used to represent various 3-D "target" surfaces for the associated contact elements such as CONTA174. The contact elements themselves overlay the solid, shell, or line elements describing the boundary of a deformable body and are potentially in contact with the target surface, defined by TARGE170. The target surface is discretised by a set of target segment elements (TARGE170) and is paired with its associated contact surface via a shared real constant set. For rigid target surfaces, these

elements can easily model complex target shapes. For flexible targets, these elements will overlay the solid, shell, or line elements describing the boundary of the deformable target body [226].

Each target surface can be associated with only one contact surface, and vice-versa. However, several contact elements could make up the contact surface and thus come in contact with the same target surface. Likewise, several target elements could make up the target surface and thus come in contact with the same contact surface. For either the target or contact surfaces, many elements may be applied in a single target or contact surface, but doing so may increase computational cost. For a more efficient model, localize the contact and target surfaces by splitting the large surfaces into smaller target and contact surfaces, each of which contain fewer elements. If a contact surface may contact more than one target surface, you must define duplicate contact surfaces that share the same geometry but relate to separate targets, that is, that have separate real constant set numbers [226].

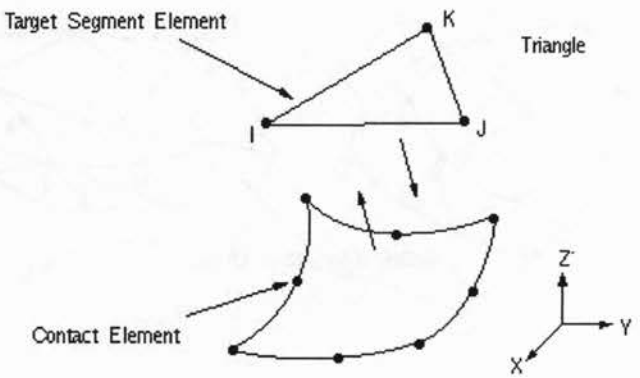

Figure 8.4 TARGE170 element description [227]

8.5 Assemblies

In comparing the performance of the hybrid implant with the conventional one, three different flexion angles were tested – 0°, 20°, and 60°. All three are shown in Figure 8.5. These angles were chosen to (1) simulate a variety of load transfer characteristics in testing the hybrid model, (2) to include the two peak flexion angles of the knee joint during the gait cyle – around 20° and 60° at around 15% and 70% of the gait cycle, as shown by Murray *et al.* [228].

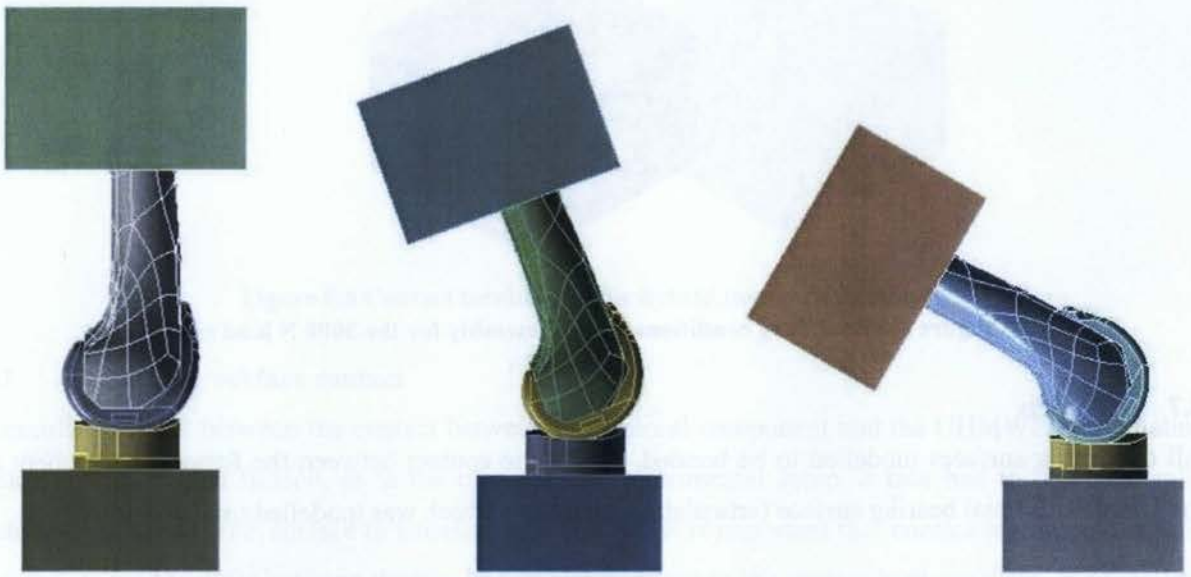

Figure 8.5 From left to right, assemblies representing 0°, 20°, and 60° flexion

8.6 Boundary conditions

The cement block is placed under fixed support (dark blue surfaces in Figure 8.6), and four faces on the cancellous bone brick were constrained to zero displacement (yellow surfaces in Figure 8.6). The applied axial force in all cases was applied on the top-facing surface the cancellous bone brick (Figure 8.6), replicating the experimental study where the actuator presses down on the tibial setup. Note that, for the cancellous brick of the tibial setup and the concrete block of the femoral setup.

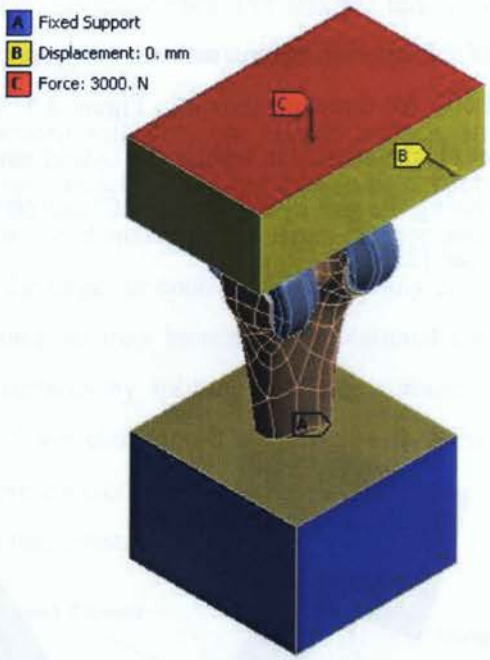

Figure 8.6 Boundary conditions on the assembly for the 3000 N load case

8.7 Contacts

All contacting surfaces modelled to be bonded, except the contact between the femoral component and the UHMWPE tibial bearing surface (articulating surface) – which was modelled to be frictional.

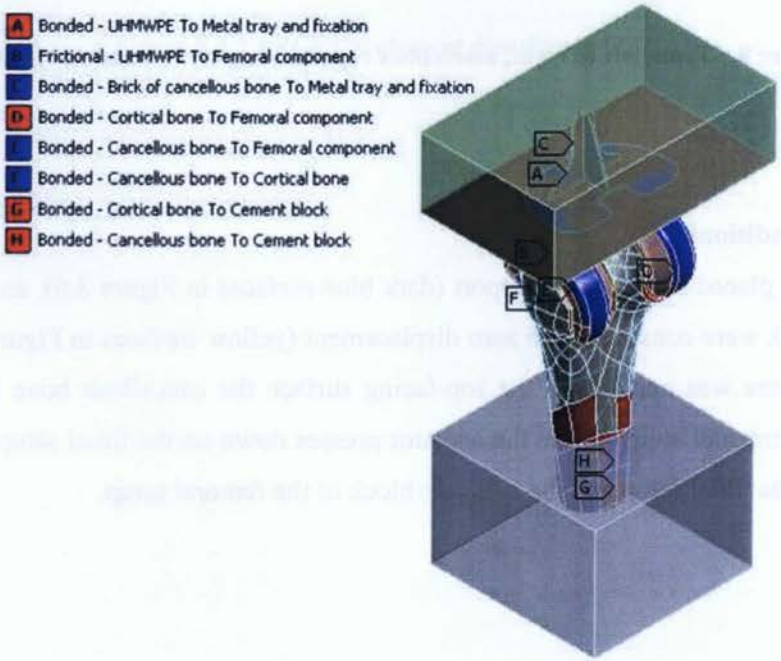

Figure 8.7 Contact locations in the conventional implant assembly

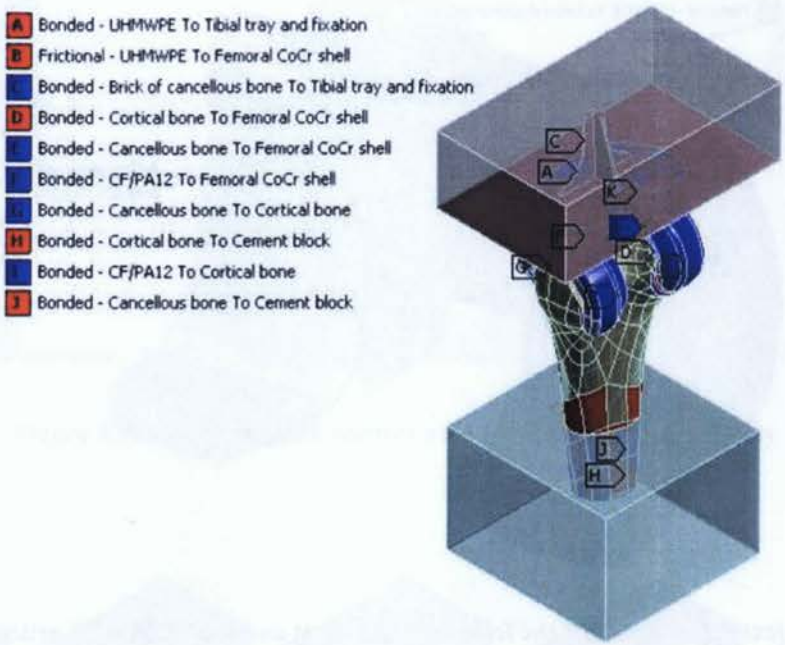

Figure 8.8 Contact locations in the hybrid implant assembly

8.7.1 Articulating surface contact

To simulate contact between the contact between the femoral component and the UHMWPE articulating surface at zero degree flexion, as is the case for the experimental setup, a face had to be specifically created on the UHMWPE surface to simulate area contact. It is important that contact region be carefully specified, as load transfer between the two bodies is dependent on the contact between them. In modelling *in* vivo contact, two previous published studies will be followed. This contact is modelled to be frictional to simulate *in vivo* contact, and a friction coefficient of 0.04 was used as per Godest *et al.* [179] in their FEA study. As will be seen in the next section, the surface mesh for the contact area was refined further. The contact regions on the articulating surface are indicated in Figure 8.9.

Figure 8.9 Contact region between the femoral component and the UHMWPE articulating surface

8.8 Mesh sensitivity and Convergence

As mentioned earlier, a tetrahedral mesh was used to model the entire assembly. A hex-dominant meshing was attempted, which failed to successfully mesh the curvaceous solid geometries in ANSYS Workbench. However, a tetrahedral mesh has been shown to model long bones with sufficient accuracy to produce meaningful numerical results by Papini *et al.* [107]. The ANSYS Workbench meshing utility allowed automatic rearrangement of the elements so that the element Jacobian, which measures the deviation from an ideally shaped element, was always above 0.7 throughout the mesh. A test to gauge the mesh sensitivity in was conducted by studying the response of a series of meshes of increasing refinement under the same applied load. Three nodes or vertices were chosen from the assembly geometry, as shown in Figure 8.10. Vertex 1 was chosen from the posterior side on the cancellous bone surface. Vertex 2 was chosen from the anterior side of the cortical bone surface. Vertex 3 was a point on the articulating surface. The chosen vertices are shown in Figure 8.10.

An axial load of 2000 N was applied, and the total displacement of the node was recorded after each refinement. The refinement was performed using the 'Relevance' utility in ANSYS Workbench, which is a global mesh control utility that allows control of the mesh *fineness*. The control options range from high speed meshing (-100 setting) to high accuracy (+100 setting). Five meshes thus created by changing the Relevance setting were tested (Figure 8.11). Mesh 4 was chosen, since an increase in the number of nodes to Mesh 5 (102%) provided only marginal changes in vertex displacements – 0.3%, 1.3%, and 0.5% for Vertices 1, 2, and 3 respectively (see Table 8.7).

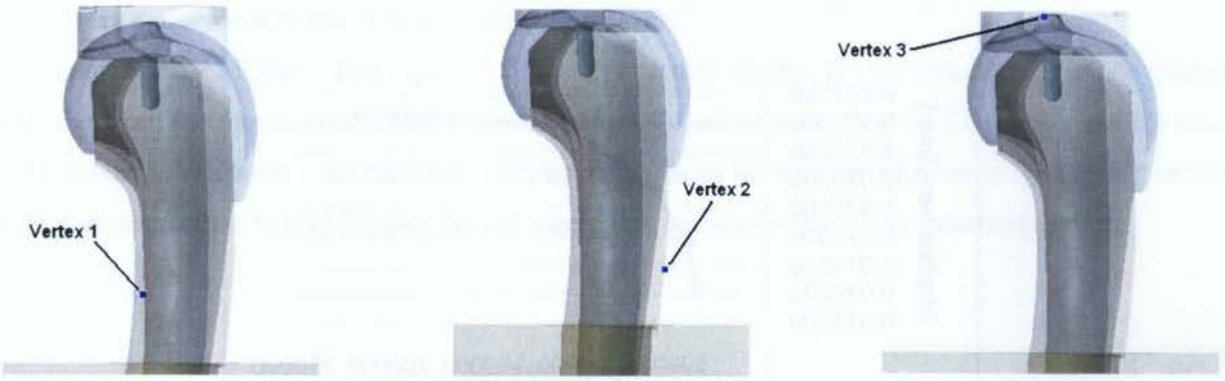

Figure 8.10 Location of the vertices used to test for mesh sensitivity

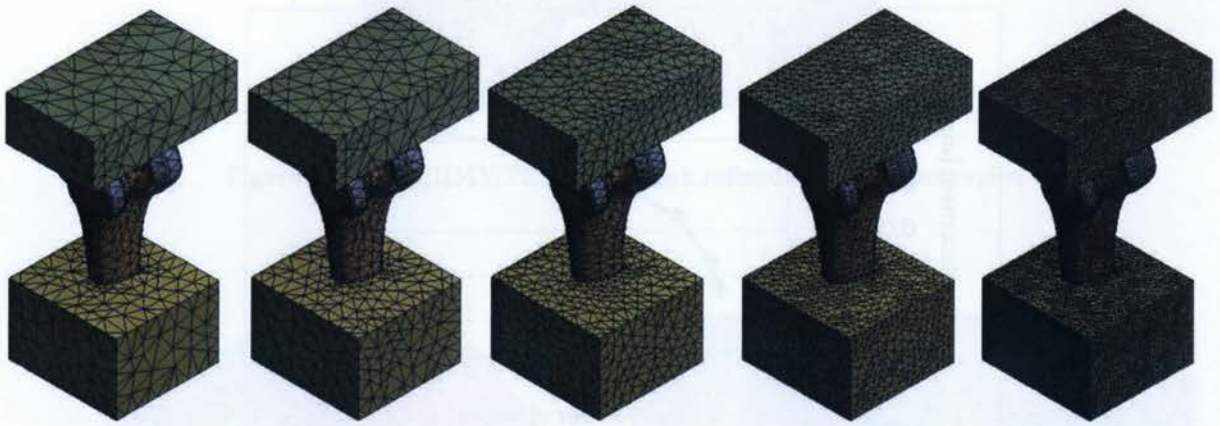

Figure 8.11 From left to right, Mesh 1 to Mesh 5, successively refined. Mesh 4 was chosen.

Format: Corresponding value (%difference from previous value)					
Mesh	Number of nodes	Number of elements	Vertex 1 displacement [mm]	Vertex 2 displacement [mm]	Vertex 3 displacement [mm]
1	36678	18904	0.074089	0.079689	0.095127
2	41834 (14.05%)	21884	0.074892 (1.08%)	0.080360 (0.84%)	0.097433 (2.42%)
3	58776 (40.50%)	31435	0.075820 (1.24%)	0.081325 (1.20%)	0.098978 (1.59%)
4	105795 (80.00%)	58945	0.076963 (1.51%)	0.082424 (1.35%)	0.100790 (1.83%)
5	213566 (101.87%)	125039	0.077201 (0.31%)	0.083532 (1.34%)	0.101320 (0.53%)

Table 8.7 Mesh characteristics and associated vertex displacements

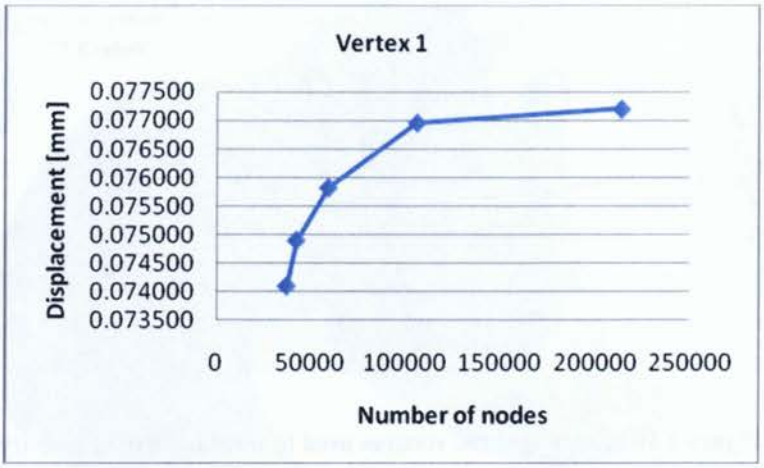

Figure 8.12 Change in displacement for Vertex 1

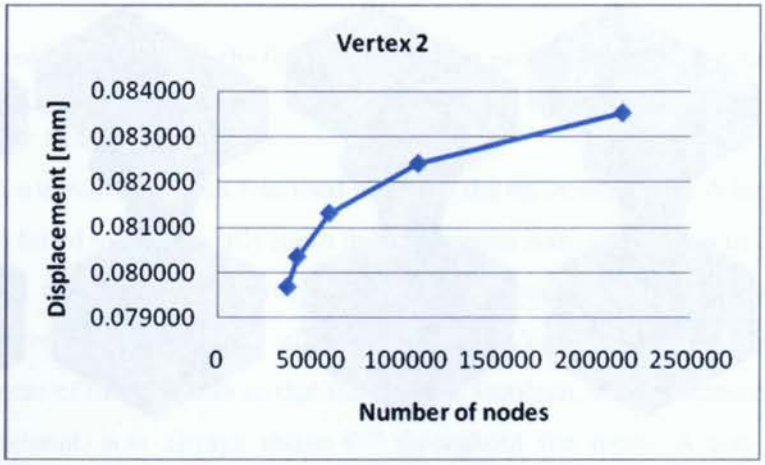

Figure 8.13 Change in displacement for Vertex 2

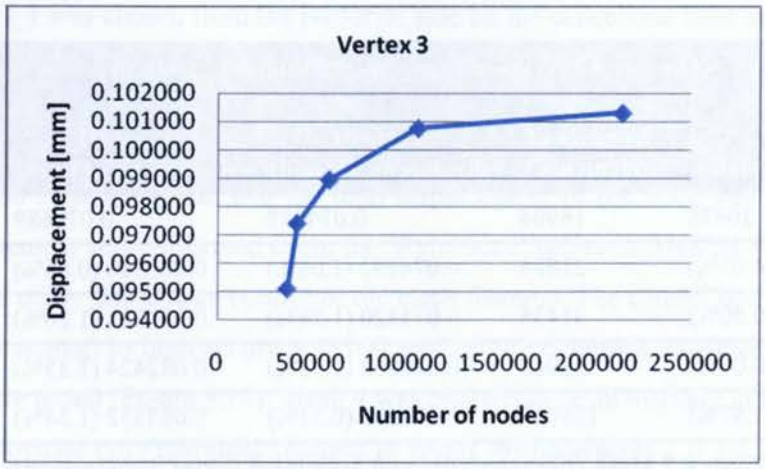

Figure 8.14 Change in displacement for Vertex 3

8.9 Mesh refinement in the critical regions of interest

In the course of the FE study, two regions will be of particular interest: (1) the articulating surface contact region between the femoral and UHMWPE components to aid in validating the FE model, and (2) once the FE model is validated – the resected condylar and anterior bone tissue adjacent to the implant to test the performance of the hybrid implant. In both cases, the region of interest was specifically refined.

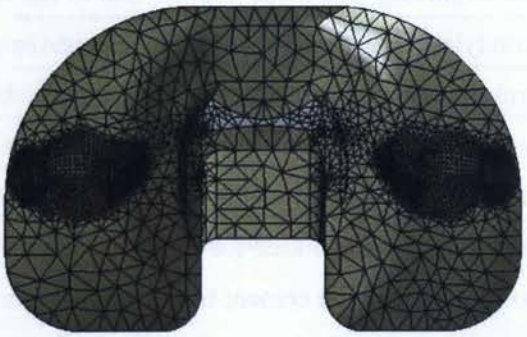

Figure 8.15 The UHMWPE surface mesh refined at the contact region

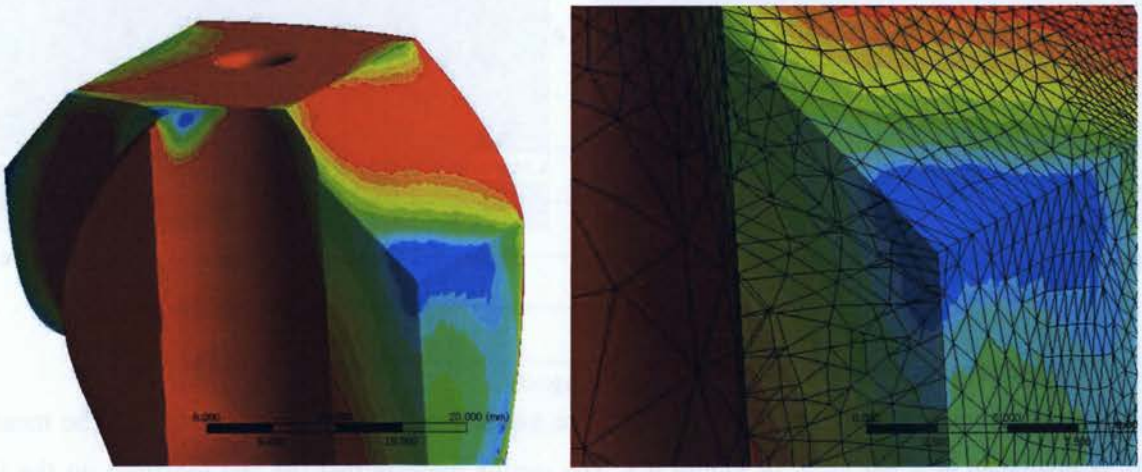

Figure 8.16 The anterior region of the distal femur showing mesh refinement at the surfaces

9 RESULTS AND DISCUSSION

9.1 Experimental study

9.1.1 Contact area and alignment

As discussed in Section 6.5 (p.64 onwards), the proper alignment of the contact surfaces was conducted by trial and error. Medial-lateral alignment was made simpler due to the conforming articular surface of the UHMWPE. The femoral condyles were designed to complement the depressions in the UHMWPE surface, where the medial-lateral motion is restricted by the 'eminence' between the medial and lateral surfaces. Obtaining proper anterior-posterior alignment required successive trials using Fuji Prescale film to verify the contact location. On obtaining correct overall alignment, it was also noticed that the film on the lateral side always observed a larger contact area for both load cases. This is probably caused by an error in the 'potting' the composite femur in the cement block producing a varus offset, due to which the lateral condyle of the femur protrudes slightly farther out than the medial condyle.

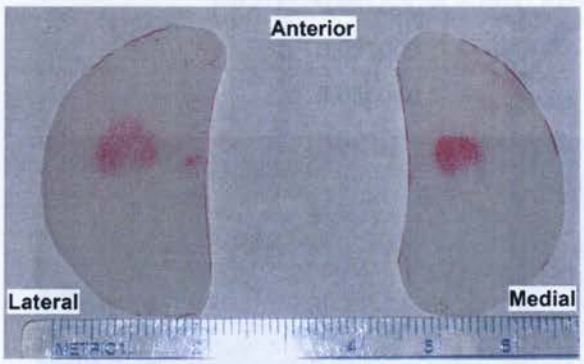

Figure 9.1 Contact location and area, 2000 N case

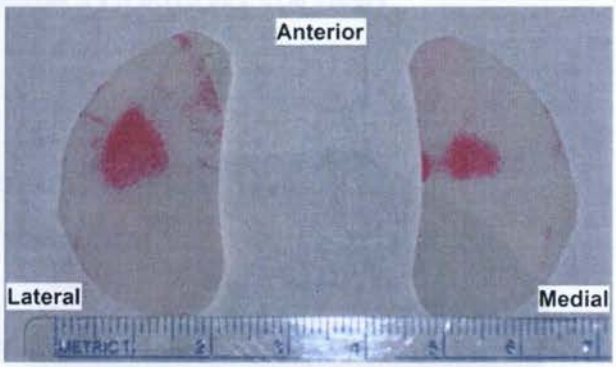

Figure 9.2 Contact location and area, 3000 N case

9.1.2 Gauge measurements

The gauge readings are tabulated in Table 9.1. The gauge locations are also identified. The measured strain is displayed as a bar chart in Figure 9.3. The results indicate that the test locations on the femur surface are under compression, whereas those on the implant surface are under tension. As expected, the measured strains are higher for the 3000 N load case than the 2000 N.

Strain gauge	Location	Strain readings (με) for load case:		State of load experienced
		2000 N	3000 N	
1	Anterior flange, femoral component	9.235	10.95	Tension
2	Anterior, diaphyseal region	-225	-413.4	Compression
3	Lateral side of lateral condyle	-238	-386	Compression
4	Posterior lateral flange	5.76	12.89	Tension
5	Posterior, diaphyseal region	-829	-1284.12	Compression
6	Posterior, metaphyseal region	-563	-847.63	Compression
7	Posterior medial flange	2.88	3.5	Tension
8	Medial side of medial condyle	-99.62	-172.75	Compression

Table 9.1 Gauge locations and strain measurements

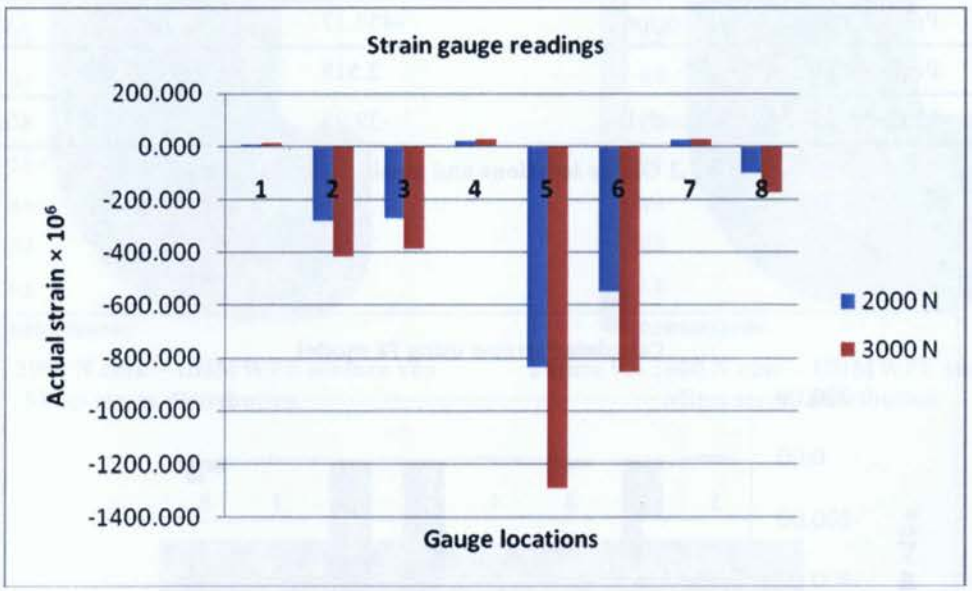

Figure 9.3 Experimental strain measurements for each load case

9.2 Finite element study: Conventional design

9.2.1 FEA calculated surface strains

The calculated strains from the corresponding gauge locations on the FE model are tabulated in Table 9.4. The gauge locations are also identified. The calculated strain is displayed as a bar chart in Table 9.4. As in the experimental case, the results indicate that locations on the femur surface are under compression, whereas those on the implant surface are under tension.

Strain gauge	Location	Calculated strain (με) for load case:		State of load experienced
		2000 N	3000 N	
1	Anterior flange, femoral component	7.928	8.772	Tension
2	Anterior, diaphyseal region	-191.29	-347.58	Compression
3	Lateral side of lateral condyle	-26.625	-43.11	Compression
4	Posterior lateral flange	5.104	9.988	Tension
5	Posterior, diaphyseal region	-749.49	-1007.3	Compression
6	Posterior, metaphyseal region	-454.17	-679.22	Compression
7	Posterior medial flange	2.518	4.01	Tension
8	Medial side of medial condyle	-39.95	-76.701	Compression

Table 9.2 Gauge locations and strain measurements

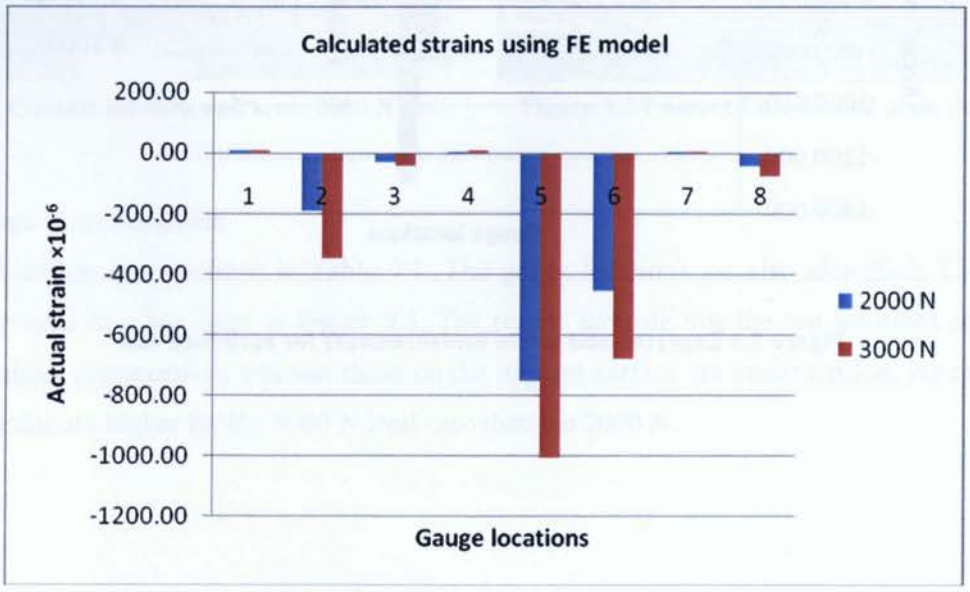

Figure 9.4 Calculated strains for each load case using the FE model

9.2.2 Stresses on the UHMWPE surface

Another validation of the FE model is conducted using the surface stress distribution generated on the UHMWPE component. As there are several published FE studies on the behaviour of the UHMWPE tibial component *in vitro*, this is a suitable measure of comparison that will indicate if contact characteristics are within expected limits. As expected, the maximum stress increases with increased compression load. In this case, for an increase of 50% between from 2000 to 3000 N, there is a nearly 100% increase in maximum von Mises stress (shown in Table 9.3). These results are in excellent agreement with published literature, as will be discussed in the next section.

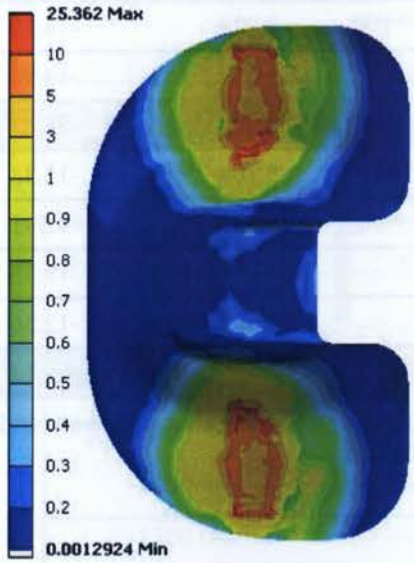

Figure 9.5 2000 N case – UHMWPE surface von Mises stress distribution

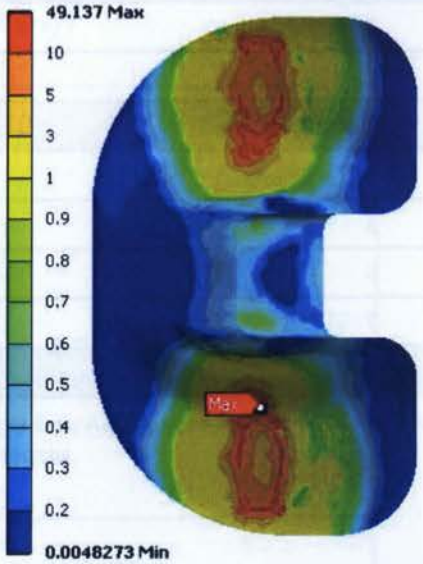

Figure 9.6 3000 N case – UHMWPE surface von Mises stress distribution

Load case	von Mises stress
2000 N	25.362 MPa
3000 N	49.137 MPa

Table 9.3 FEA results of the UHMWPE surface stress

9.3 Validation of the FE model

9.3.1 Comparing the experimental and FEA strain measurements

The FEA strain calculations for 2000 N load case are given in Table 9.4, and compared with the corresponding strain gauge readings. The same is done for the 3000 N case in Table 9.5. A visual interpretation is provided for both load cases in the bar charts of Figure 9.7 and Figure 9.8. The actual strain distribution plots labelling the strain value at each location are given in the Appendix B (p.115 onwards). As can be seen, the FE model consistently underestimates the surface strain in both load cases.

Gauge location	Experimentally measured strain (με)	FEA calculated strain (με)	Difference (%)
1	9.235	7.928	-14.15
2	-225	-191.29	-14.98
3	-238	-26.625	-88.81
4	5.76	5.104	-11.38
5	-829	-749.49	-9.591
6	-563	-454.17	-19.33
7	2.88	2.518	-12.56
8	-99.62	-39.95	-59.89

Table 9.4 2000 N load case – FEA and experimental surface strain results (location of gauge readings suspected of error shaded grey)

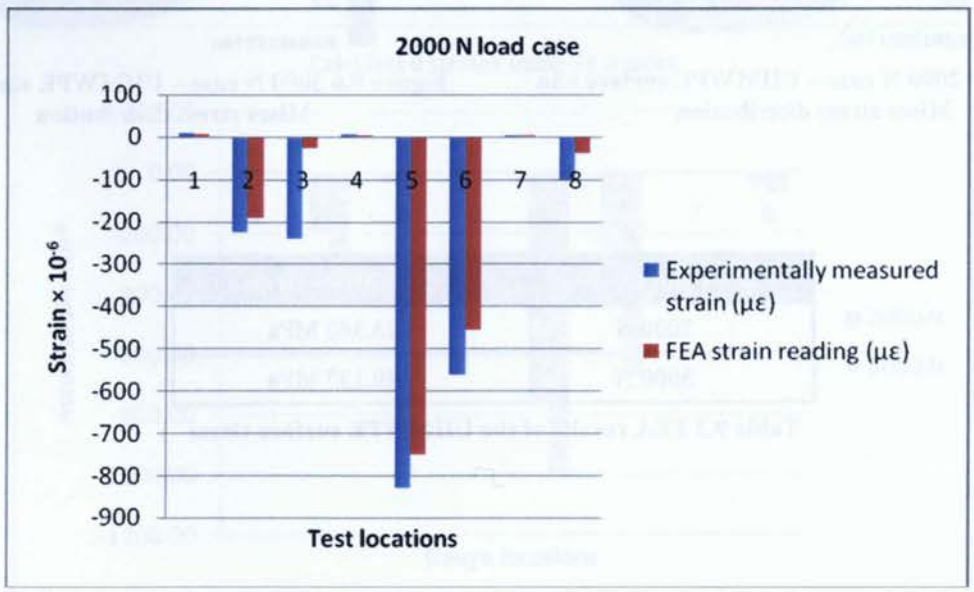

Figure 9.7 2000 N load case – Comparing experimental and FE-calculated strains

Gauge location	Experimentally measured strain (με)	FEA strain reading (με)	Difference (%)
1	10.95	8.772	-19.89
2	-413.4	-347.58	-15.92
3	-386	-43.11	-88.83
4	12.89	9.988	-22.51
5	-1284.12	-1007.3	-21.55
6	-847.63	-679.22	-19.86
7	3.5	4.01	14.57
8	-172.75	-76.701	-55.60

Table 9.5 3000 N load case – FEA and experimental surface strain results (location of gauge readings suspected of error shaded grey)

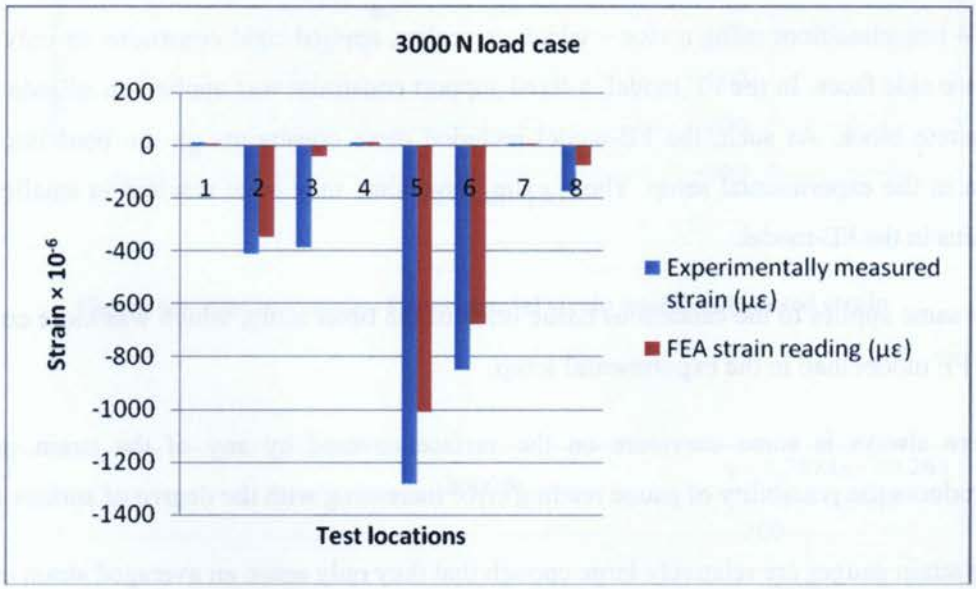

Figure 9.8 3000 N load case – Comparing experimental and FE-calculated strains

Six of the eight gauge readings agree well with the FEA calculated results (within 10-15% for the 2000 N case; 15-23% for the 3000 N load case), while the readings for locations 3 and 8 have unusually high disagreement (shaded rows in Table 9.4 and Table 9.5). This unusual observation is most probably due to unreliable gauge readings at these locations – while all other chosen locations are relatively flat, the bone surface at locations 3 and 8 is highly curvaceous, along which the strain gradients can be expected to vary rapidly. The gauge foil size is larger than the expected strains by at least four orders of magnitude. Considering the relatively large size of the foil in the strain gauges used (3.18 mm in length), it would be difficult to obtain reliable uniaxial readings over a curved surface.

Also, it can be seen that the experimental readings from location 3 (lateral condyle) are much higher than those from location 8 (medial condyle) for both load cases. The percentage difference between the measured and calculated readings is also larger for location 3 than location 8. This is consistent with the varus-valgus alignment characteristics displayed by the Fuji Prescale film tests discussed in Section 9.1.1, p.91. The film discolouration showed evidence of contact asymmetry due to a varus rotation offset – the lateral contact area was larger than the medial one. It follows that under a constant axial compressive force, the strain recorded on the lateral condylar surface would exceed that on the medial condylar surface.

In the remaining 6 locations, the up to 23% difference in FEA calculated results can be explained as follows:

1. In the experimental study, the concrete block of the femoral setup was held fixed to the Instron 8874 baseplate/floor using a vice – which, in reality, applied rigid constrains on only small areas of *two* side faces. In the FE model, a fixed-support constraint was applied on *all* side faces of the concrete block. As such, the FE-model included more constraints on the bone-implant system than in the experimental setup. These extra constraints may have resulted in smaller calculated strains in the FE-model.

2. The same applies to the cancellous tissue brick of the tibial setup, which was more constrained in the FE model than in the experimental setup.

3. There always is some curvature on the surface covered by any of the strain gauges. This introduces the possibility of gauge reading error increasing with the degree of surface curvature.

4. The strain gauges are relatively large enough that they only sense an averaged strain over the area they cover. In comparison, selecting the same point on the FE model provides the precise calculated nodal strain value at the particular location.

5. A careful attempt was made to ensure that all gauges would be oriented along the vertical axis. The strain gauge orientation on the surface plane, however carefully applied, may still slightly be off-axis with respect to the vertical and therefore differ from the FE-calculated measurements.

Barring locations 3 and 8, all FEA results can be considered to represent the experimental study well. At the level of micro-strains, a similarity within 23% is a convincing validation of the FE model. For further evidence of the FE model's viability, the experimental strain measurements are plotted against the FE-calculated strains. Figure 9.9 and Figure 9.10 plot the strain correlations for the 2000 N case and 3000 N

case, respectively. As can be seen from both plots, the correlation coefficients for both load cases are above 0.94. This is indicative of a strong correlation between both sets of strain measurements. It is also observed that the FE model shows more accuracy for the 2000 N case.

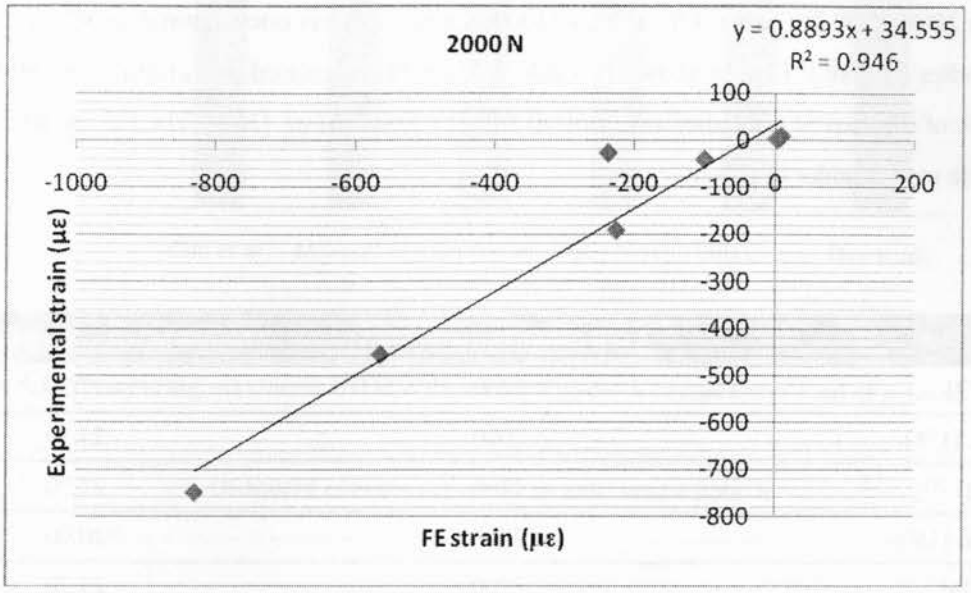

Figure 9.9 2000 load case – Experimental strain vs. FE-calculated strain

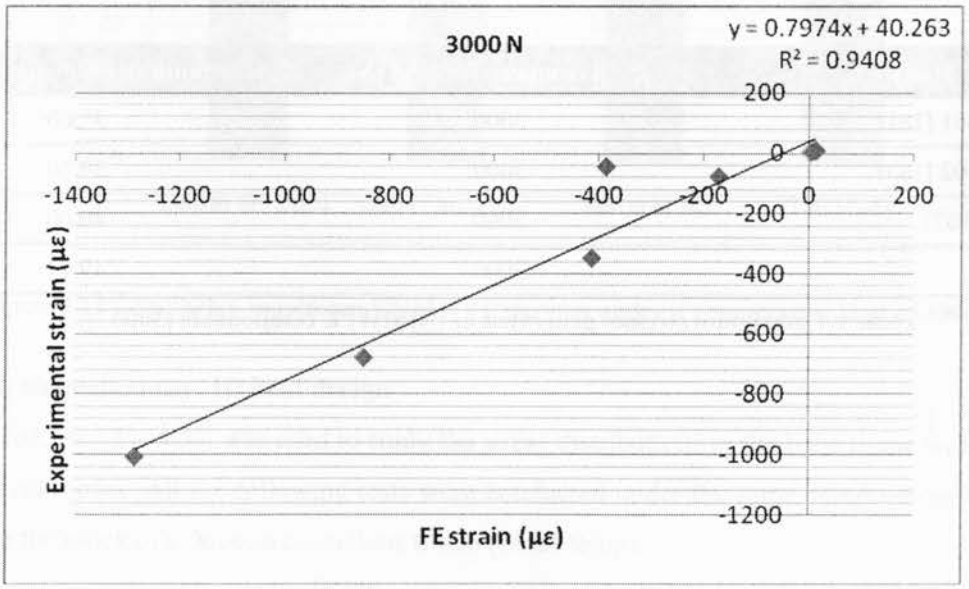

Figure 9.10 3000 N load case – Experimental strain vs. FE-calculated strain

9.3.2 Comparing UHMWPE surface stress results with literature

As mentioned earlier, the stress generated in the UHMWPE component is a good indicator of the contact characteristics and load transfer in the tibiofemoral joint. For the 2000 N load case, the is excellent agreement between published results and the FE-calculated UHMWPE stress values of 23.36 MPa (Figure 9.11). While each study has a different method of loading, the magnitude of axial compression was between 2000-2300 N (Table 9.6). For the 3000 N case, there is once again a good agreement with published studies (Figure 9.12). As shown in Table 9.7, the FE-calculated maximum stress of 49.14 MPa is within 23% of the closest published result of 40 MPa by Bartel *et al.* [162]. The FE model thus proves to be a reliable model under both load cases.

Study	Axial compressive load (N)	Maximum stress generated (MPa)
Chu *et al.* [177]	2200	17.20
Miyoshi *et al.* [178]	2000	23.30
Godest *et al.* [179]	2200	23.90
Halloran *et al.* [180]	2300	20.00
Villa *et al.* [144]	2200	27.70
This study	2000	23.36

Table 9.6 Published maximum stresses generated in UHMWPE components (~2000 N)

Study	Axial compressive load (N)	Maximum stress generated (MPa)
Liau *et al.*, 2001 [181]	3000	32.00
Liau *et al.*, 2002 [183]	3000	39.50
Bartel *et al.* [162]	3000	40.00
This study	3000	49.14

Table 9.7 maximum stresses generated in UHMWPE components (3000 N)

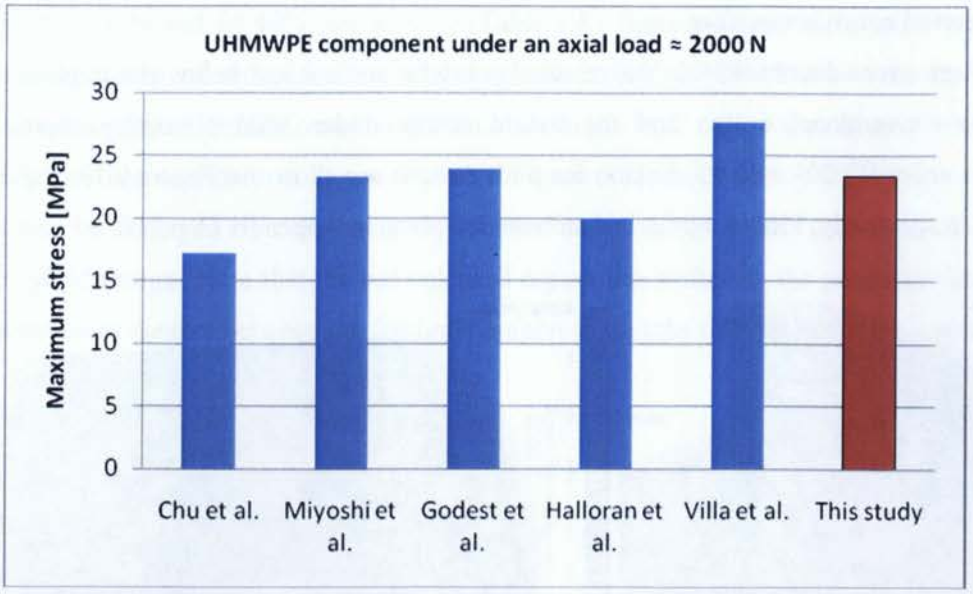

Figure 9.11 Comparing maximum UHMWPE stresses under a compressive load of around 2000 N

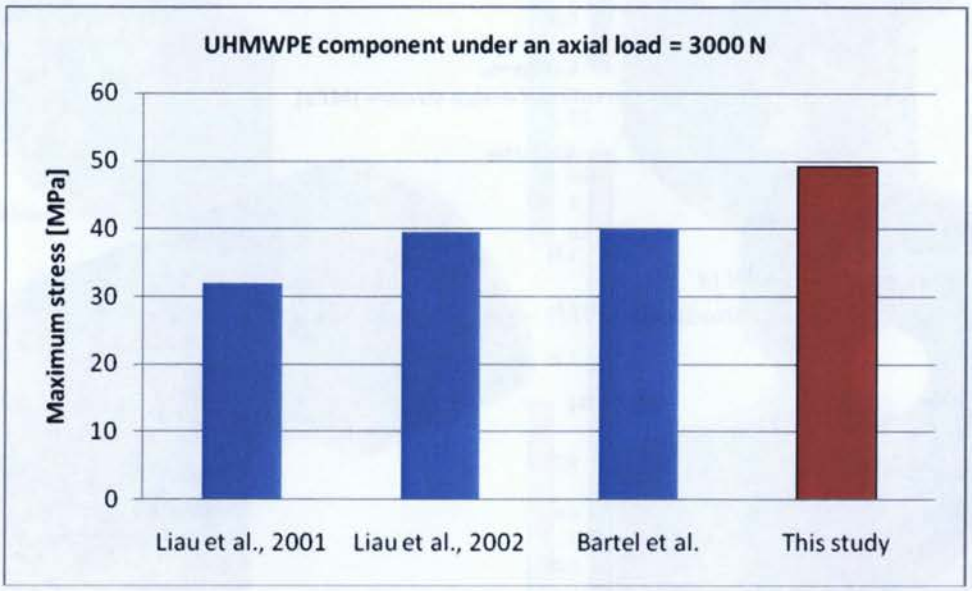

Figure 9.12 Comparing maximum UHMWPE stresses under a compressive load of 3000 N

9.4 Finite element study: Hybrid design

Once validated, the FE model was used to study the stress distributions in the bone tissue when implanted with the hybrid model. All the following tests were conducted under the same compressive load of 3000 N applied on the block of synthetic cancellous tissue (tibial setup).

9.4.1 Resected condylar surface

The von Mises stress distribution on the resected condylar surface just below the implant is compared between the conventional design and the hybrid design under 3000 N axial compression. Stress distributions under 0°, 20°, and 60° flexion for both designs are shown in Figure 9.13, Figure 9.14, and Figure 9.15, respectively. Plots for principal stresses are given in Appendix C, p.118.

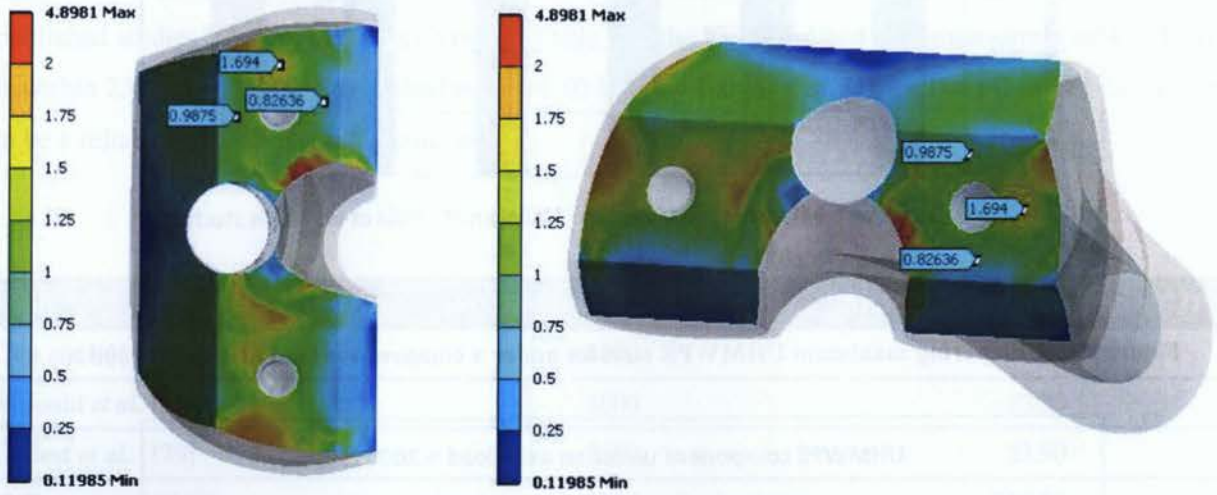

a) Conventional design stresses [MPa]

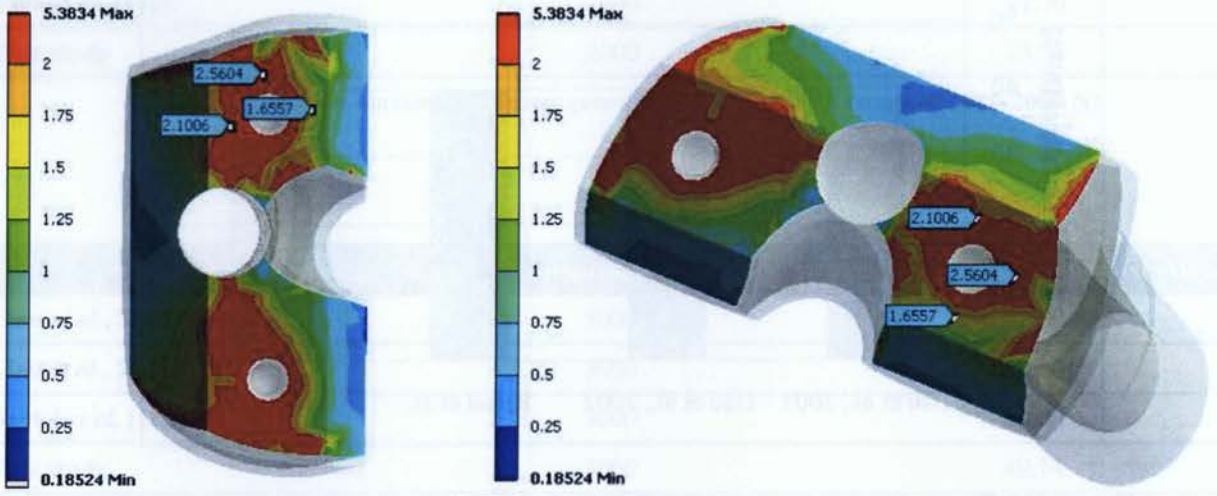

b) Hybrid design stresses [MPa]

Figure 9.13 Zero-degree flexion – Equivalent von Mises stress distribution on the condylar surfaces below the implant

The stress distribution plots provide a visual representation of the change in stress on the condylar surface. Comparing the contours, one can observe the 'red' colour region (2 MPa and above) covering a larger area in the hybrid design case – indicating that a hybrid design transfers more stress to the bone tissue than a conventional one. The maximum and minimum equivalent von Mises stress is higher for the

hybrid design by 9.91% and 54.46% respectively (Table 9.8). Since an increase in stress transfer to the bone tissue is indicative of reduced stress shielding, the hybrid CF/PA12 shows strong potential in preserving bone integrity. A similar considerable increase in the 'red' region area is also observed for the 20° and 60° flexion cases, shown in Figure 9.14 and Figure 9.15, respectively. This increase in surface stresses can also be observed by comparing the labelled stress values of the conventional design with those of the hybrid design. Note that the red coloured region has shifted to the posterior side, reflecting the shift in location of contact between the femoral component and the tibial articulating surface.

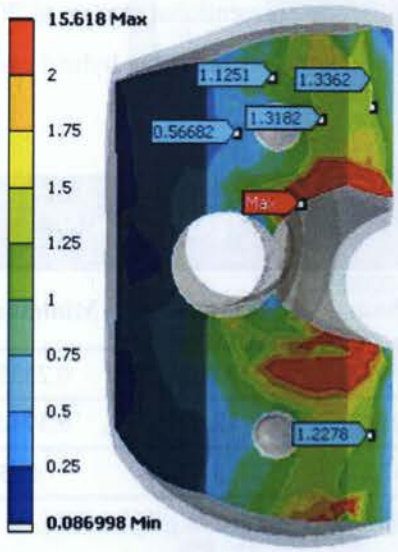

a) Conventional design case

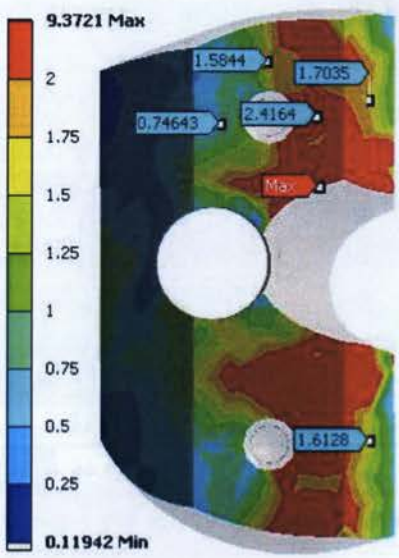

b) Hybrid design case

Figure 9.14 20° flexion – Equivalent von Mises stress [MPa] distribution on the condylar surface

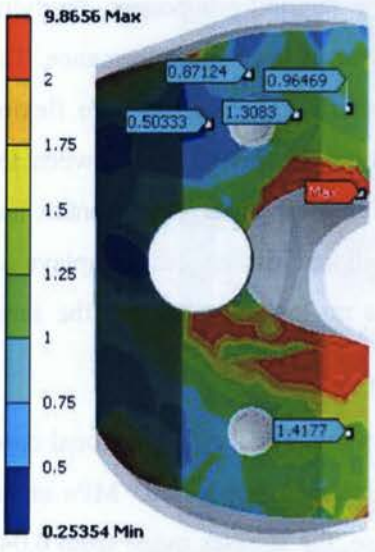

a) Conventional design case

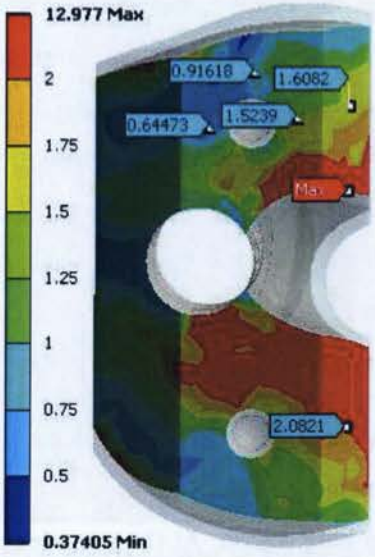

b) Hybrid design case

Figure 9.15 60° flexion – Equivalent von Mises stress [MPa] distribution on the condylar surface

As seen in Table 9.8, the maximum and minimum equivalent von Mises stress 60° flexion is higher for the hybrid design by 31.74% and 47.53% respectively. The high-stress 'red' region is much higher in the hybrid case than in the conventional case (Figure 9.15). The labelled annotations in Figure 9.15 also show that the stress distribution on the condylar surface is higher for the hybrid design.

At 20° flexion, an anomaly is observed – the maximum von Mises stress is higher for the conventional design. However, the labelled annotations, and the larger predominance of the 'red' region in the hybrid case indicates that more stress is being transferred to the bone tissue when a hybrid femoral component is applied (Figure 9.14). The unusually high maximum von Mises stress for the conventional design at 20° may be a localised nodal anomaly. At the same time, the minimum von Mises stress is for the hybrid case is 37.27% larger than that in the conventional case.

	0° flexion		20° flexion		60° flexion	
von Mises stress	**Maximum**	**Minimum**	**Maximum**	**Minimum**	**Maximum**	**Minimum**
Conventional	4.8981	0.1199	15.618	0.086998	9.8656	0.25354
Hybrid	5.3834	0.1852	9.3721	0.11942	12.997	0.37405
Increase (%)	**9.91**	**54.46**	**-39.99**	**37.27**	**31.74**	**47.53**

Table 9.8 Condylar surface von Mises stresses under 3000 N (anomaly shaded in grey)

9.4.2 Resected anterior distal femur

As discussed earlier in an earlier chapter (Section 4.3.3, p.30), a critical region where stress shielding is thought to occur in the distal femur is behind the anterior flange of the femoral component. Studying stresses generated in the cancellous tissue in this region is a good indicator of implant performance. The anterior region is always a low-stress region in the distal femur, especially under zero-degree flexion (straight standing). The following figures compare the stress distributions in this region between the conventional and hybrid knee implant case. Figure 9.16 displays a section view of the distal femur, and the FE-calculated stress distributions through the tissue. The conventional design case displays an obvious low stress region (0.006–0.4 MPa) coloured in blue, which is no longer present in the same section view of the hybrid design case.

Figure 9.17 shows the stress distribution along the edges of the section view. For the conventional case, the von Mises stresses vary from around 0.0247 MPa in the edge junction to nearly 0.03 MPa at the fringes of the deep blue region. At the same locations for the hybrid case, the stresses range from 0.046 MPa upto 0.05667 MPa. The stress contours and the annotated nodal distributions show higher stresses

being generated in the bone tissue with a hybrid implant. These results further validate the applicability of the hybrid CF/PA-12/metal implant in reducing stress shielding in this region.

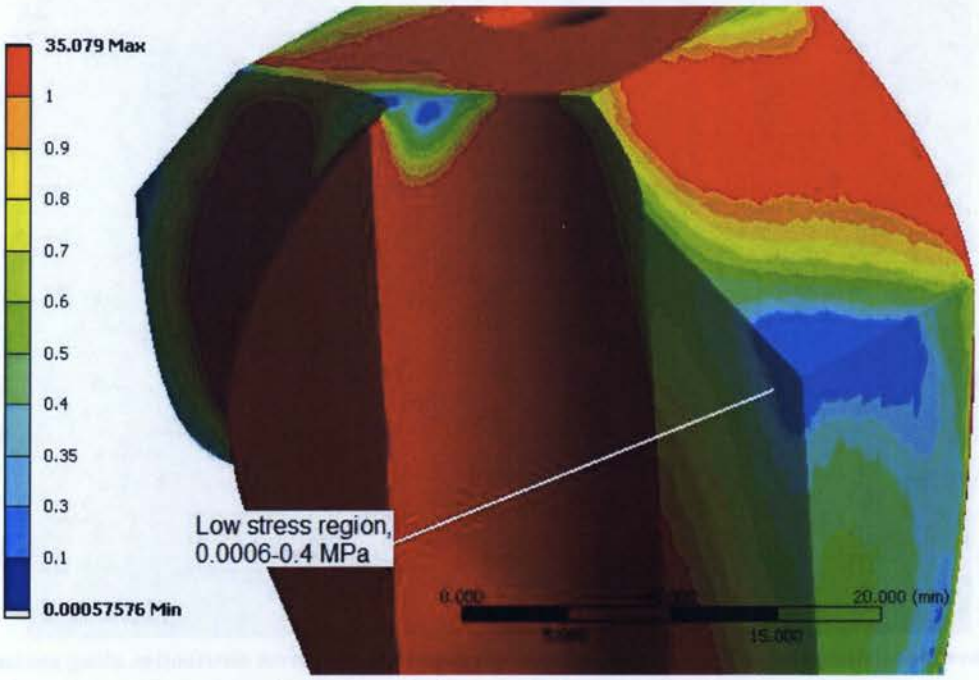

a) Conventional design case: Section view in the sagittal plane showing low stress 'deep blue' region

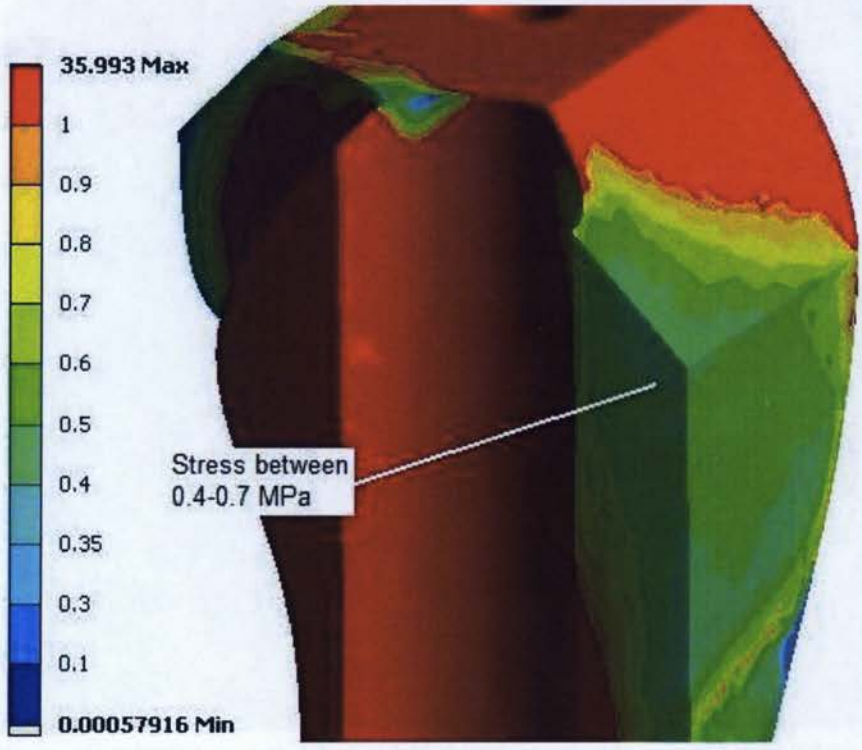

b) Hybrid design case: Same section view in the sagittal plane showing almost no low-stress 'blue' region

Figure 9.16 0° flexion – Equivalent von Mises stress [MPa] distribution contours in the anterior distal femur

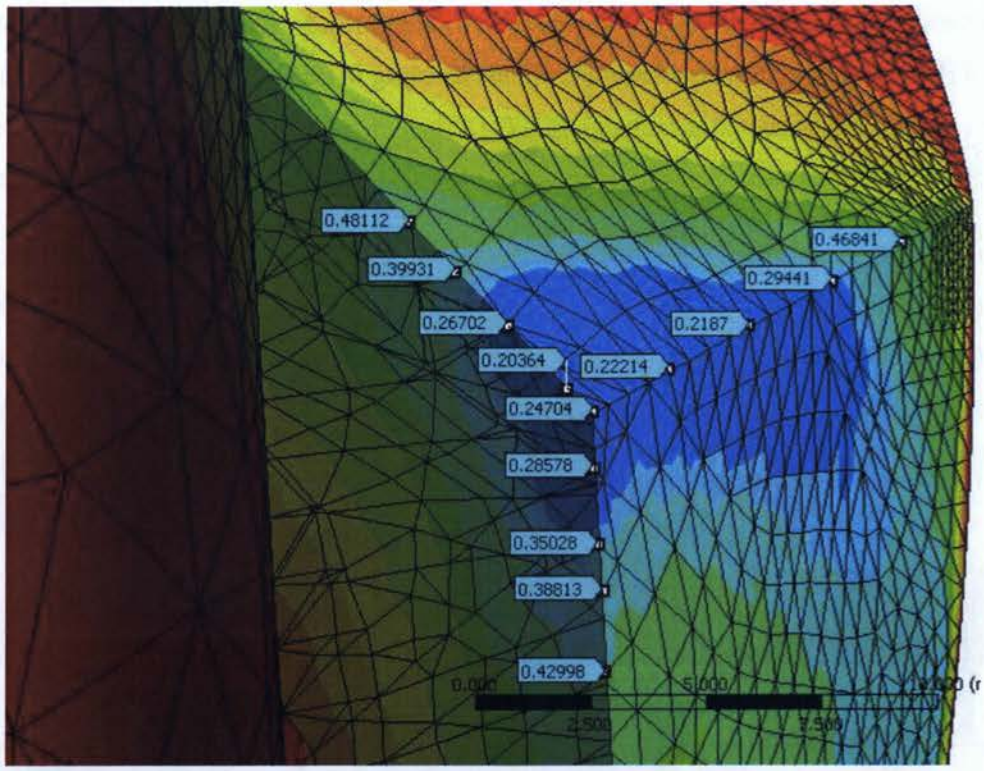

a) Conventional design case: Close-up with annotations showing nodal stress distribution along section edges

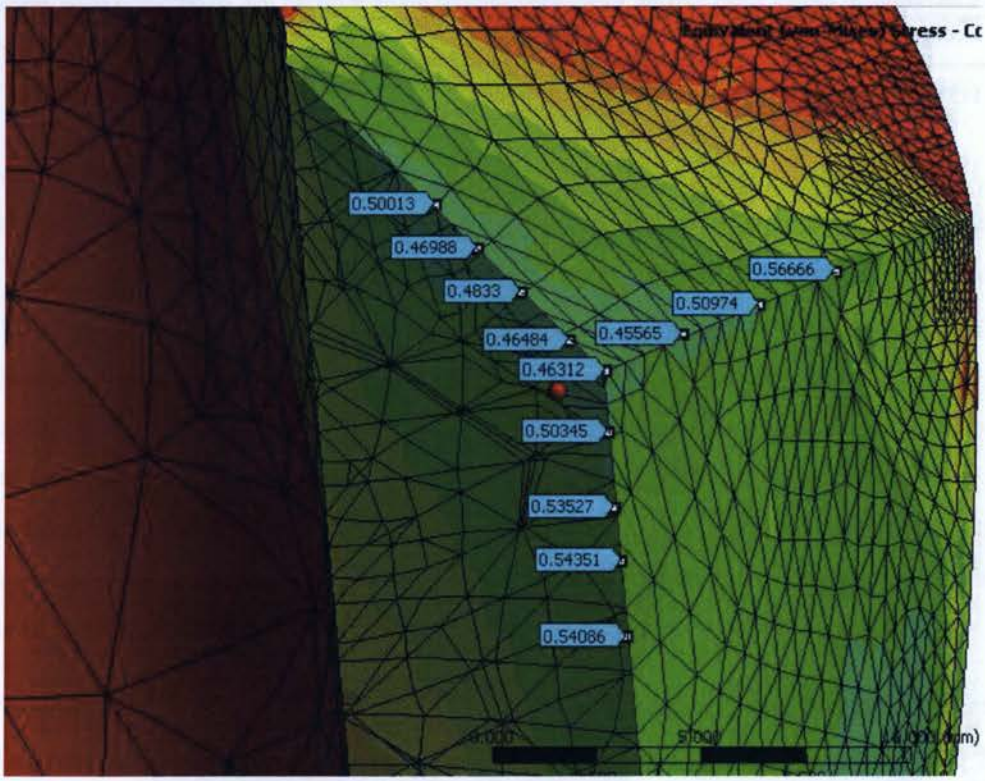

b) Hybrid design case: Close-up showing noticeably higher nodal stress distribution along section edges

Figure 9.17 Equivalent von Mises stress [MPa] distribution in the anterior distal femur

Similar increases in anterior distal femur stress distribution for the hybrid design case can be seen for the 20° and 60° flexion, though the increase is less prominent in the 60° case. Figure 9.18 shows the contours and nodal stress distribution along the resected edges for 20° flexion. The conventional case shows a predominance of the low stress 'blue' region, which is not the case for the hybrid case. The labelled annotations show that, once again, there is an increase in the nodal stress when a hybrid design is applied. It can be safely inferred, therefore, that stress transfer from the implant to the bone in the anterior distal femur is improved even at a flexion angle of 20°.

Figure 9.19 shows the stress distribution for the 60° flexion case. Again, there is a discernable increase in the high stress 'red' region along the edges of the hybrid case, further proving that the hybrid design facilitates increased stress transfer from the femoral component to the bone tissue. However, it is observed that the difference between the conventional and hybrid cases is much less at 60° flexion.

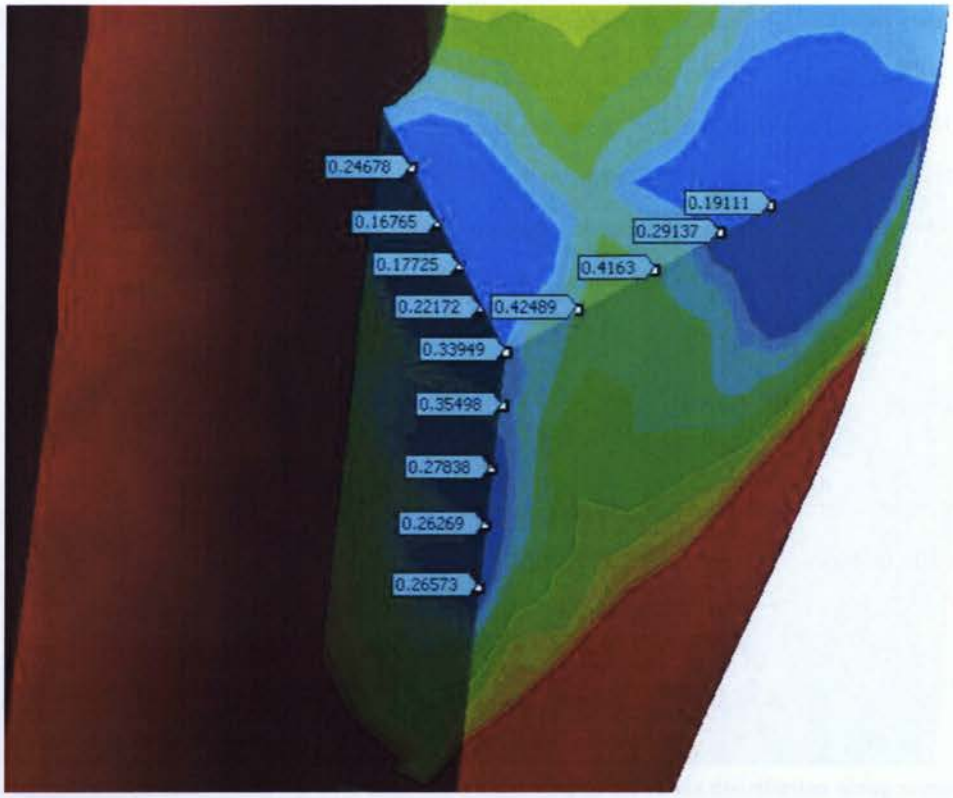

a) Conventional design case: Low stress 'blue' regions visible on the resected edges

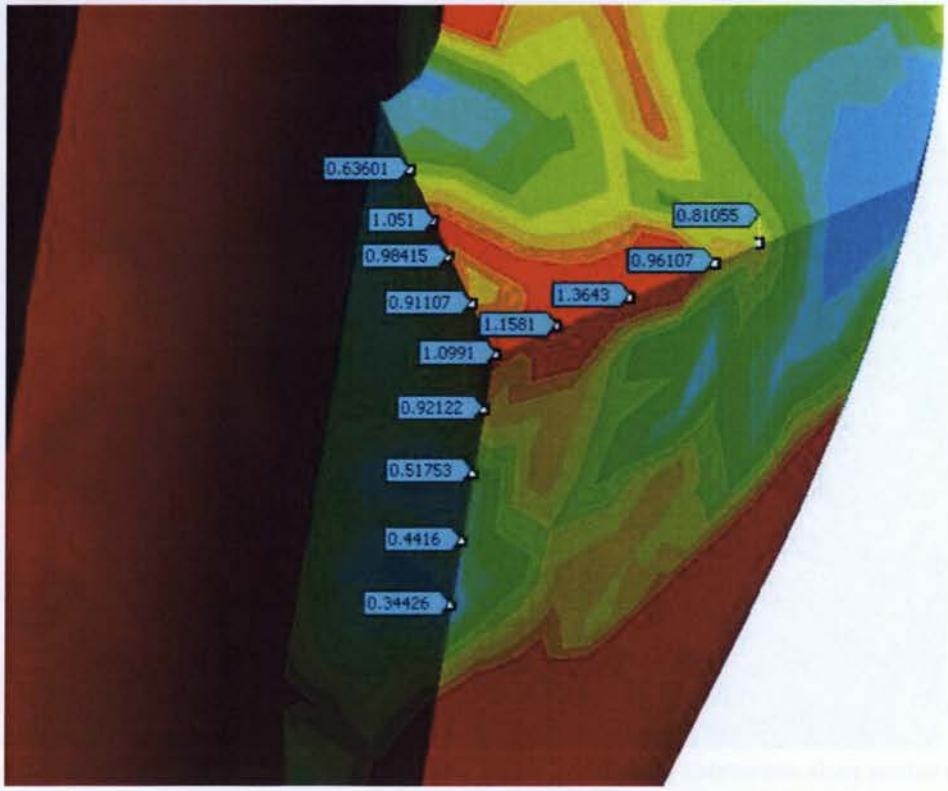

b) Hybrid design case: Higher nodal stresses along the edges, with larger distribution of high stress 'red' regions

Figure 9.18 20° flexion – Equivalent von Mises stress [MPa] distribution in the anterior distal femur

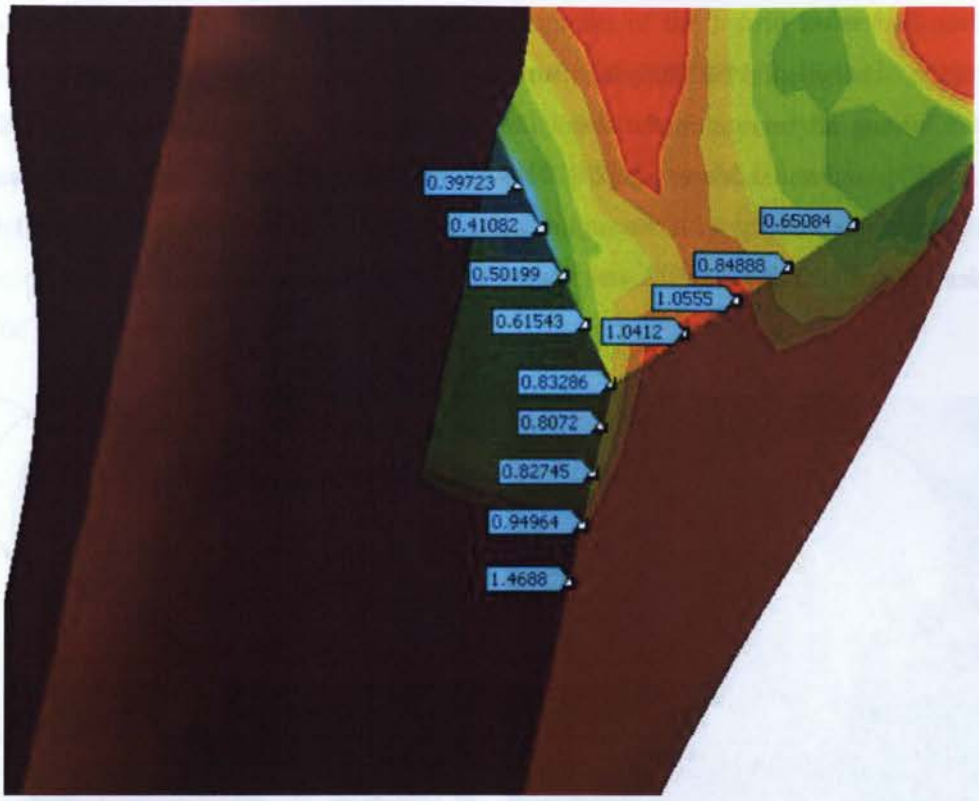

a) Conventional design case

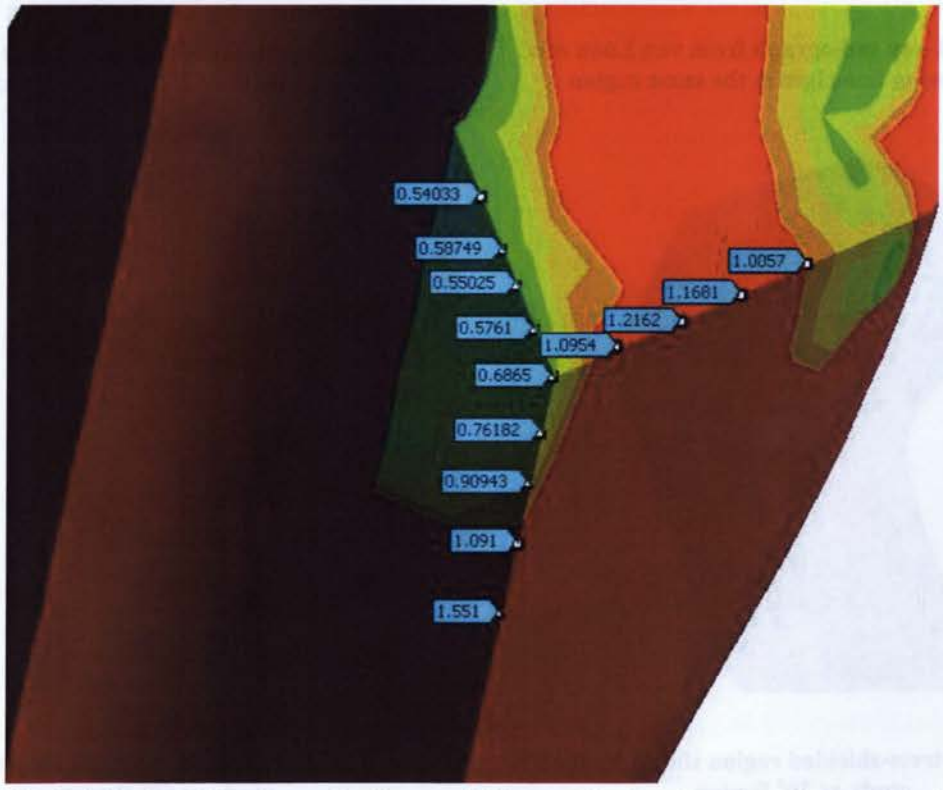

b) Hybrid design case: Broader predominance of high stress 'red' regions along the resected edges

Figure 9.19 60° flexion – Equivalent von Mises stress [MPa] distribution in the anterior distal femur

9.5 Further discussion

From the results obtained, the FE study confirms that the anterior region indeed experiences the least loading under among all regions in the distal femur – as observed by Cameron and Cameron [151], Mintzer *et al.* [23], and van Loon *et al.* [24]. This study confirms that the region of femoral bone loss (Figure 9.22).coincides exactly with the region most shielded from loading stresses at all three tested flexion angles (Figure 9.23, Figure 9.22, and Figure 9.23 for 0°, 20°, and 60°, respectively).

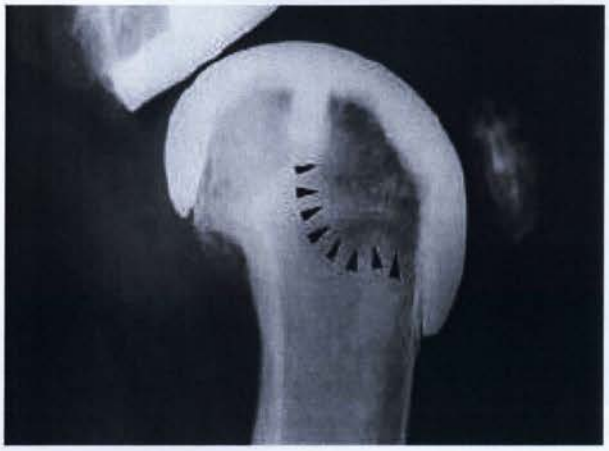

Figure 9.20 X-ray radiograph from van Loon *et al.* [24] showing bone loss in the same region

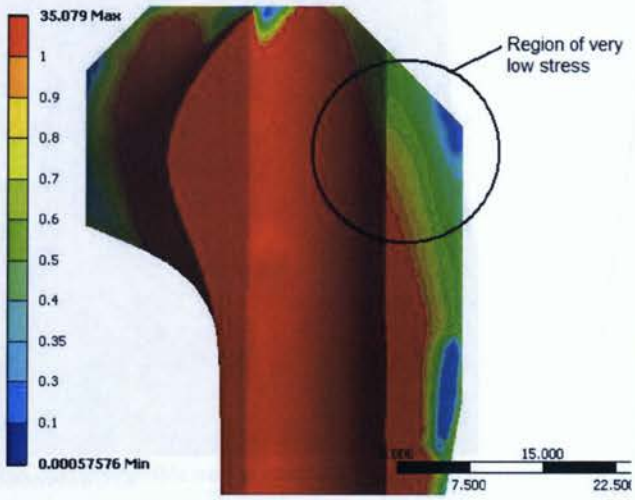

Figure 9.21 Stress-shielded region in the bone tissue shown by the FE study at 0° flexion

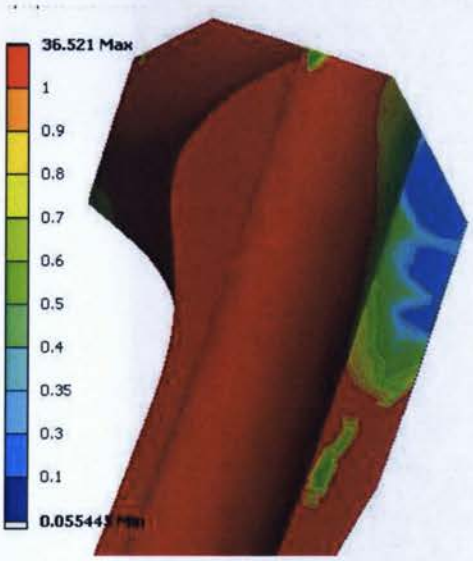

Figure 9.22 Stress-shielded region shown by the FE study at 20° flexion

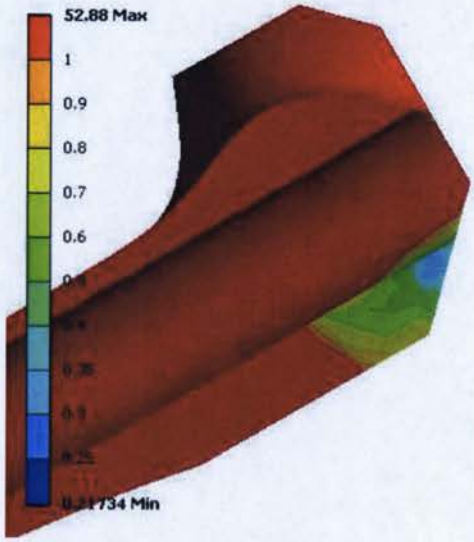

Figure 9.23 Stress-shielded region shown by the FE study at 60° flexion

As shown in Section 9.4.1 (p.101), there is a definite impact of the hybrid knee design on the stress transfer between the implant and the bone. Under the same load of 3000 N, the hybrid design case shows 9.91-31.74% increase in the maximum von Mises stress generated on the condylar surface over the three test flexion angles, and around 37-55% increase in the minimum von Mises stress (refer back to Table 9.8). This, in conjunction with the stress plots discussed in Section 9.4.2 (p.103), show convincingly that the presence of a CF/PA12 layer in the femoral component has definite advantages in promoting stress transfer to the bone tissue.

10 CONCLUDING STATEMENTS AND FUTURE CONSIDERATIONS

The hybrid implant is envisaged to be a compound structure comprising of a layer of CF/PA12 material enclosed by a CoCrMo shell, with the overall dimensions of a conventional femoral component. The inspiration for this innovation is the hip implant designed entirely out of CF/PA12 by Campbell and colleagues [38-41], which has been shown to provide excellent biomimetic properties. While these implants have only been tested *in vitro*, and have not yet been introduced into mainstream orthopaedic care, clinical proof of this material's viability has yet to be obtained. The history of orthopaedics has shown that prosthetic knees have always incorporated the success of prosthetic hips [3], and this study has attempted to emulate the same through a finite element study. However, it is yet to be seen how such an implant will be fabricated, and whether its practical use will result in improved implant longevity. To answer the research question posed in Chapter 5 (p.44), it appears that the proposed hybrid design offers noticeable benefits in transferring more stress to the adjacent bone tissue.

In conducting all portions of this study, several obvious limitations are recognised. A limitation of this study is that only one design of the hybrid component was studied (3.0 mm-thick CoCrMo femoral shell). Lower thicknesses would reduce the overall elastic modulus of the hybrid femoral component, and theoretically would provide higher implant-to-bone stress transfer. However, reducing the CoCrMo thickness will adversely affect the rigidity of the femoral component, making it prone to fracture. To resolve this issue and obtain an 'optimum' thickness, a wide range of short-term and cyclic tests (both experimental and numerical) need to be conducted on designs with varying CoCrMo and CF/PA12 thicknesses.

As already discussed in the previous chapter, the FE model used in this study overestimated the constraints on the bone-implant system when compared to the experimental setup. A possible result of this would be an underestimation of surface strains by the FE-model, which is what the results have indicated. However, since the FE model *consistently* underestimates the experimental study, it follows that comparative studies conducted by the FE model are still able to indicate any improvement in stress shielding.

Uniaxial strain gauges were used in the experimental study to obtain surface strains. Further accuracy in strain measurement is possible using biaxial, or rosette gauges. In any future study, using rosettes is highly advisable as it can be used to directly measure the principal strains on the test location.

Considering the fact that strain gauges of any kind will always have relative dimensions much larger than the strains generated on bone geometry, any improvement in measurement accuracy would be prudent.

The experimental study is performed using a commercially available knee prosthesis implanted on *simulated* bone. Cadaveric bone specimens for the femur and tibia were not used. The simulated bones are fourth-generation composite models to simulate natural human bones in shape and compression behaviour for use in experimental studies. The experimental analysis in this study was conducted to serve as means for comparison, to ensure that the numerical finite element model was viable. As reported by Papini *et al.* [107], third generation composite bone models are most representative of young, healthy bone stock. Since the fourth generation bone models *improve* on the fatigue and fracture characterisites of third generation models [108, 109], it follows that the fourth generation models also represent healthy bone. Had cadaveric or osteoporotic bone samples been used in this experiment, the experimentally recorded strains may have been higher – since overall bone modulus would have been lower.

Both the experimental and numerical studies are based on static analyses of the bone-implant system. This thesis does not include any dynamic analysis of the models to determine implant performance during motion (flexion and extension). This study limited itself to comparing peak stresses under a load representative of the maximum axial force transmitted through the knee joint during regular gait. A static analysis applying the maximum axial force with relevant constraints is quite sufficient to address the problem statement and research question of this thesis, i.e. to investigate if a hybrid implant reduces the incidence of stress shielding. Certainly, a dynamic study of the bone-implant system that incorporates all ligament and muscle force inputs on the joint would be useful, but unnecessary for the purposes of this study.

In the future, before dynamic study is performed, a quasi-static analysis may be attempted. This study, while using three different flexion angles, applied the same 3000 N compressive force on the knee joint. This does not completely respresent the realistic loading of the distal femur at the tested flexion angles, as the tibiofemoral compressive force changes with flexion angle. Also, at angles other than zero degrees, the distal femur is affected by patellofemoral contact in addition to the tibiofemoral forces. For a realistic quasi-static analysis, several flexion angles my be tested statically, but realistic forces on the distal femur in the form of patellofemoral and ligament forces have to be simulated. While a dynamic or quasi-static analysis would provide a realistic distribution of stresses in the distal femur, the inference of this thesis study is not expected to be affected – i.e. the 'isoelastic' hybrid model incorporating a biomimetic CF/PA12 interface layer should still exhibit improved stress transfer characteristics. Whether this

improvement results in relevant savings in bone loss and implant failure cannot be confirmed until at least a simulation of bone remodelling is performed.

This study does not predict the incidence of osteolysis or bone density changes due to alterations in the stress distribution of the femoral component. This study has restricted itself to studying whether the presence of a CF/PA12 layer will result in lower peak stresses in the hybrid femoral component. Any increase in peak stresses in the femoral bone will indicate that more of the load is being transferred to the bone, thereby reducing the potential for bone resorption in the distal femur. While models of bone adaptation to loading environments exist in published literature [19, 140], the results produced in this study will not be extrapolated for expected changes in the surrounding bone tissue. Despite this, the fact remains that any increase in bone tissue stresses provides an argument in favour of hybrid metal-CF/PA12 prosthetics. No doubt, a favourable prediction of bone adaptation will further establish the potential for CF/PA12 in hybrid femoral components – and this may well be an area of further research.

At the outset of this study, limits were imposed on the scope of this project to conduct an analysis that is well representative of *in vivo* biomechanics and yet possible to conduct within the anticipated timeline. Much of this study has been devoted producing an error-free CAD model of the femur, conducting and improving the experimental procedure, followed by developing a representative finite element model that will negate the need to conduct the same experiment repeatedly. Considering that the knee joint function is more complex than other synovial joints, this study has been performed on a rather idealised static scenario incorporating only three knee flexion angle. However, within the confines of the goals of this study outlined in Chapter 5 (p.44), sufficient details have been incorporated through the modelling of realistic bone and implant geometry to produce reliable results. The fact that the finite element model has matched the experimental strain results (barring two locations) within a 23% error indicates the success of the model. It is the author's hope that this finite element model will well serve the needs of a variety of future parallel knee joint researches such as those outlined in the preceding paragraphs: dynamic analysis including all aspects of the gait cycle, prosthetic joint function including soft tissue in the modelling, extreme loading conditions such as running up a ramp or squatting, etc.

APPENDIX A LOAD-DISPLACEMENT CURVES OF THE EXPERIMENTAL STUDY

Displacement readings are obtained as feedback displayed on the FastTrack™ 8800 load control system interface every 0.01 seconds. The actuator arm displacement is plotted against the compressive axial load applied on the bone-implant assembly. At least 3 runs were conducted for each load case. Figure A.1 and Figure A.2 show the plots for the one run each of the 2000 N and 3000 N load cases, respectively.

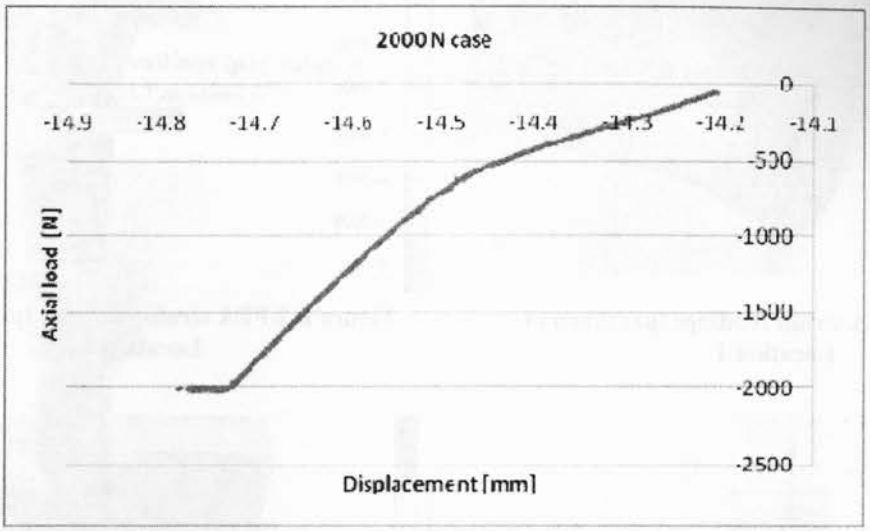

Figure A.1 Axial load vs. Displacement, 2000 N case

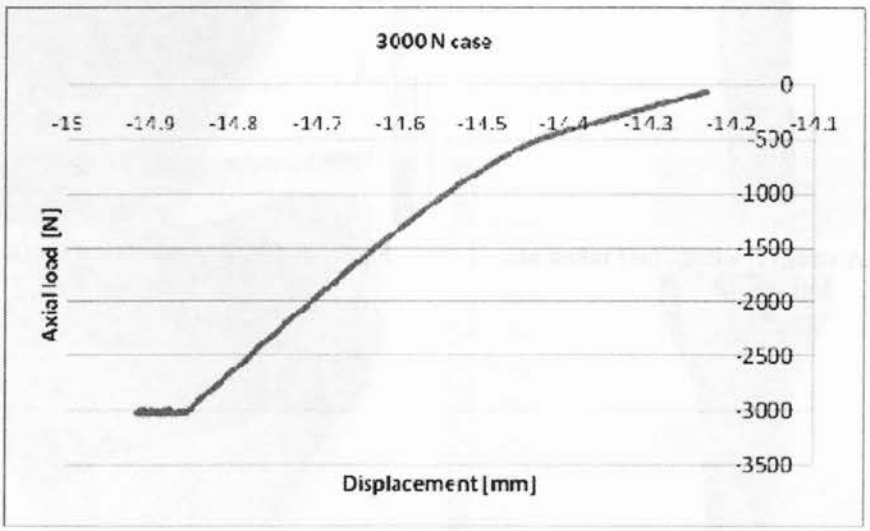

Figure A.2 Axial load vs. Displacement, 3000 N case

APPENDIX B SURFACE STRAIN READINGS ON THE FE MODEL

B.1 2000 N load case

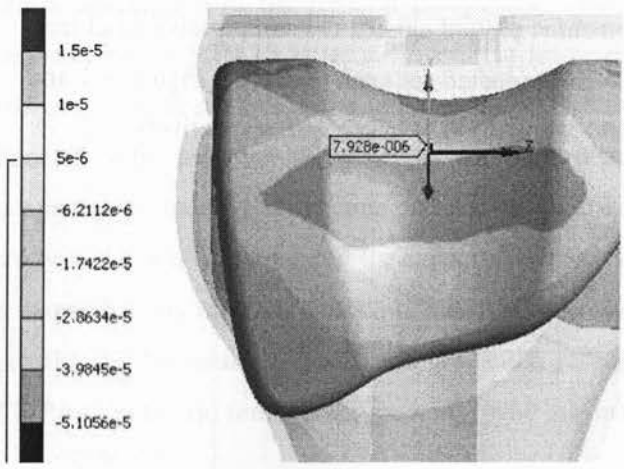

Figure B.1 FEA strain readings (με) taken at Location 1

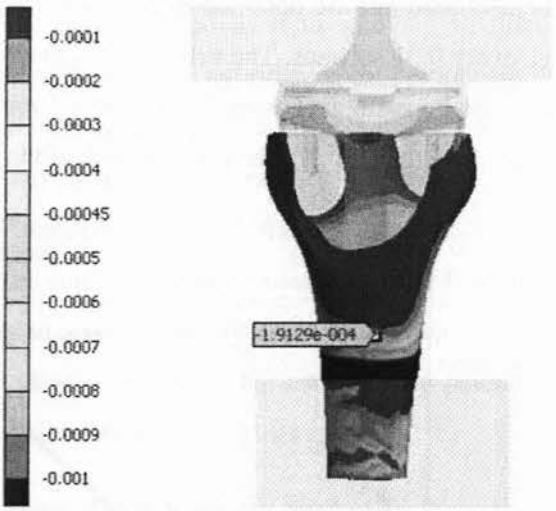

Figure B.2 FEA strain readings (με) taken at Location 2

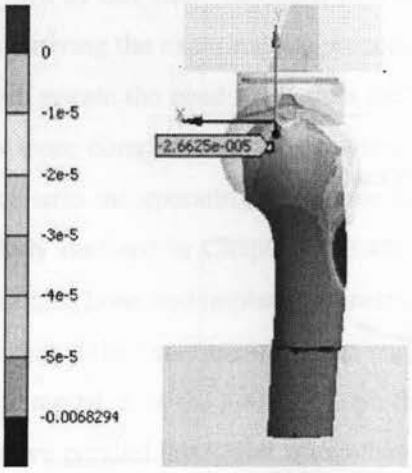

Figure B.3 FEA strain readings (με) taken at Location 3

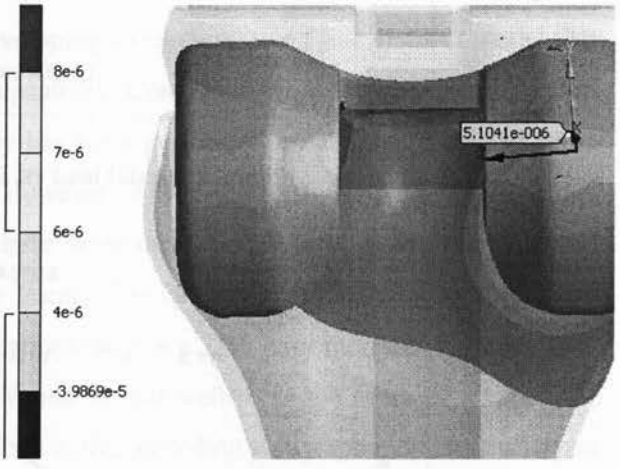

Figure B.4 FEA strain readings (με) taken at Location 4

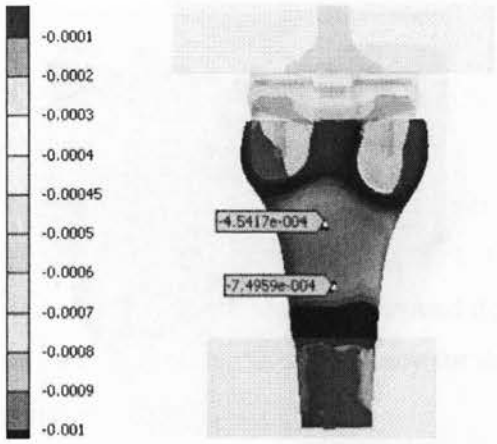

Figure B.5 FEA strain readings (με) taken at Location 5 and Location 6

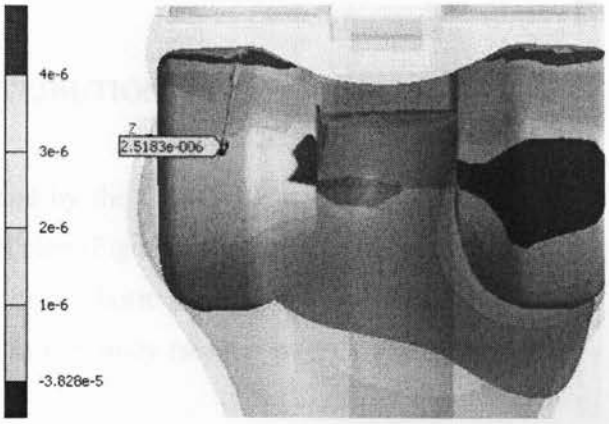

Figure B.6 FEA strain readings (με) taken at Location 7

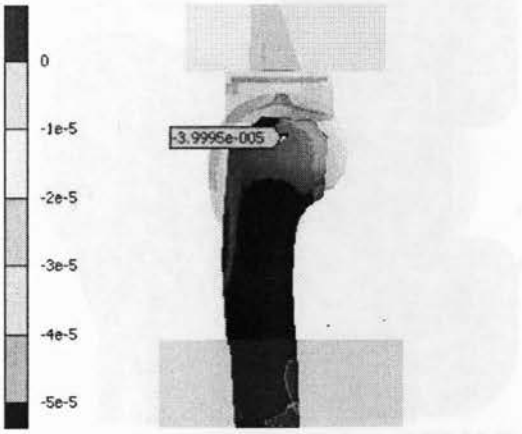

Figure B.7 FEA strain readings (με) taken at Location 8

B.2 3000 N load case

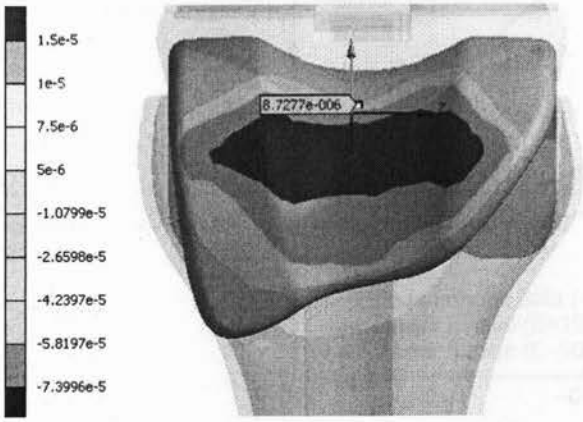

Figure B.8 FEA strain readings (με) taken at Location 1

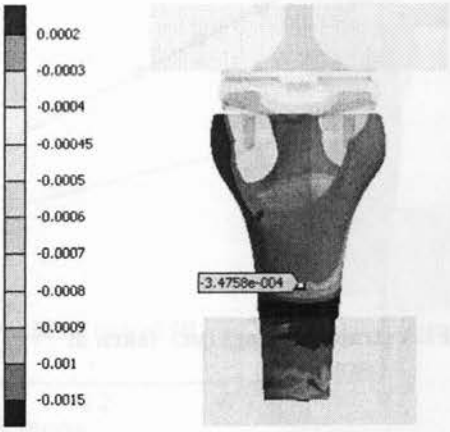

Figure B.9 FEA strain readings (με) taken at Location 2

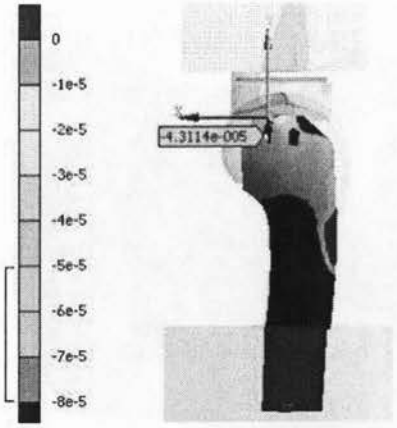

Figure B.10 FEA strain readings (με) taken at Location 3

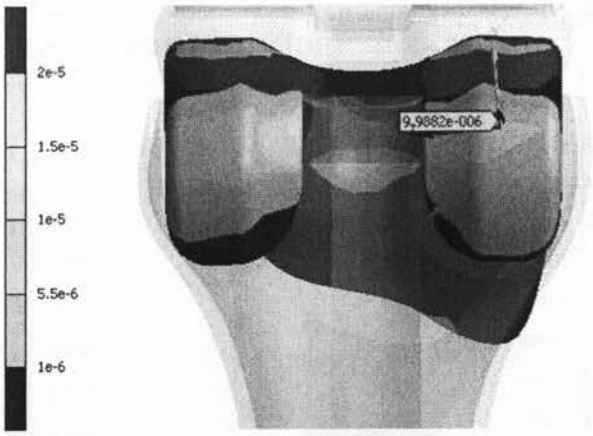

Figure B.11 FEA strain readings (με) taken at Location 4

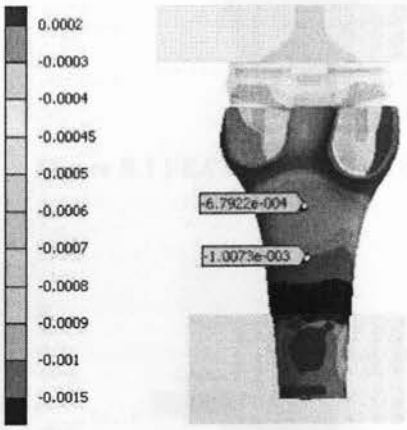

Figure B.12 FEA strain readings (με) taken at Location 5 and Location 6

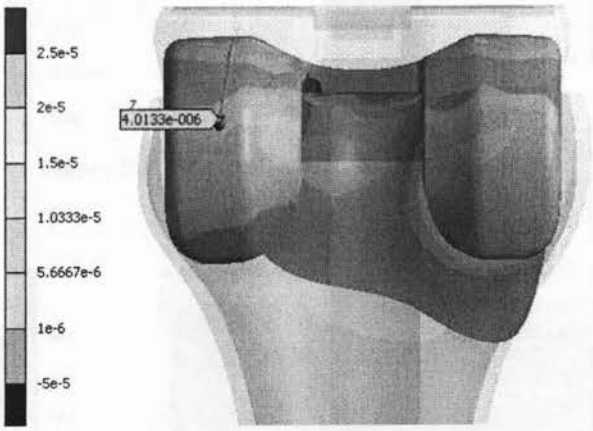

Figure B.13 FEA strain readings (με) taken at Location 7

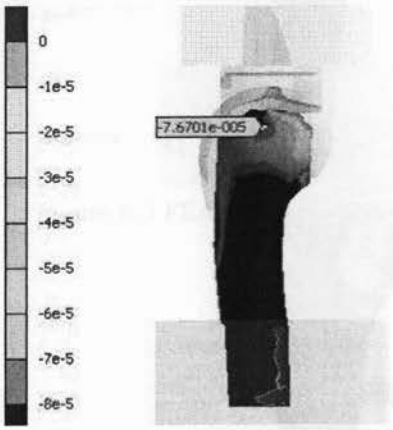

Figure B.14 FEA strain readings (με) taken at Location 8

APPENDIX C UHMWPE STRAIN DISTRIBUTION

The maximum equivalent von Mises strain experienced by the UHMWPE component is 0.02818 and 0.054597 for the 2000 N case (Figure C.1) and 3000 N case (Figure C.2), respectively. As the maximum strains under both test loads are around 0.5 or less, the linear elastic model for UHMWPE (E = 900 MPa) was a choice of sufficient accuracy for the FE model in this study (see the straight-line without plotted points in Figure C.3).

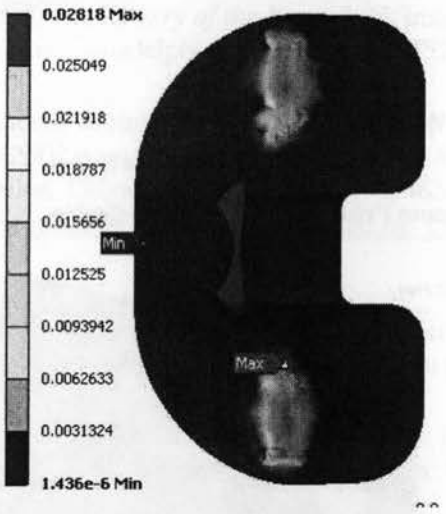

Figure C.1 2000 N case – UHMWPE surface von Mises strain distribution (exaggerated deformation)

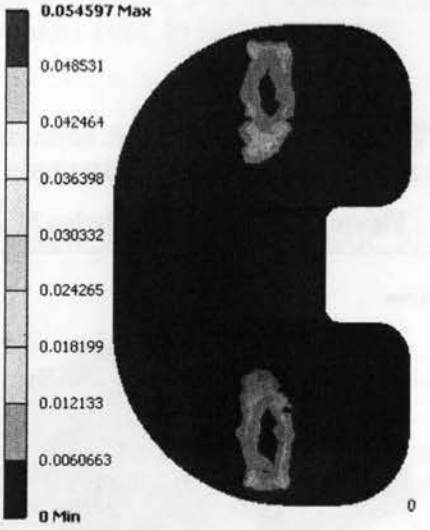

Figure C.2 3000 N case – UHMWPE surface von Mises strain distribution

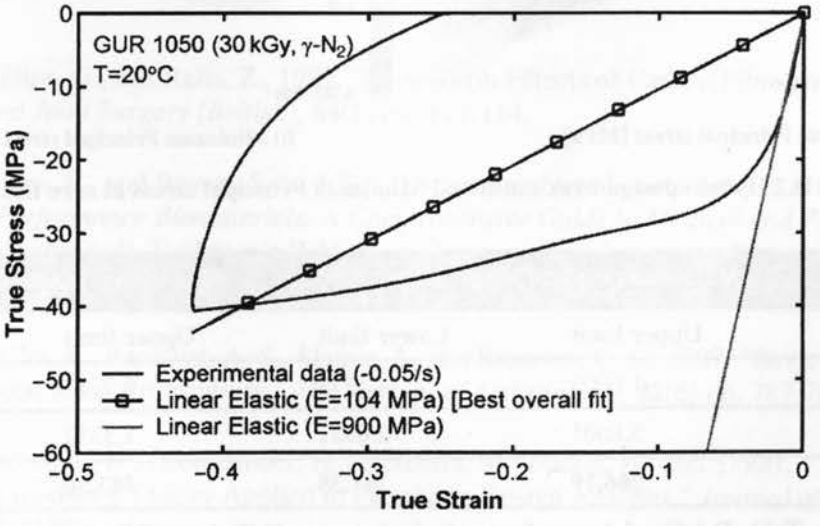

Figure C.3 Linear elasticity model compared to actual compression behaviour of UHMWPE as per Bergström [165]

APPENDIX D CONDYLAR SURFACE PRINCIPAL STRESSES FOR 0° FLEXION

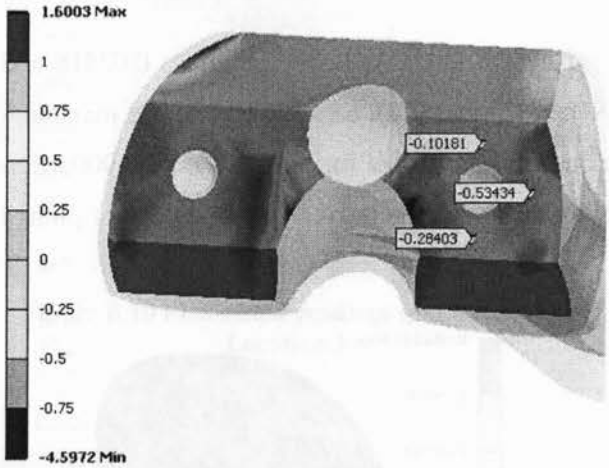

a) Maximum Principal Stress [MPa]

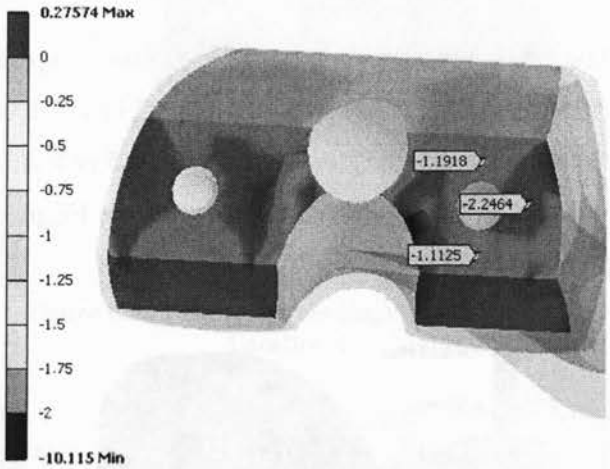

b) Minimum Principal Stress [MPa]

Figure D.1 Conventional design M aximum and Minimum Principal stress at zero flexion

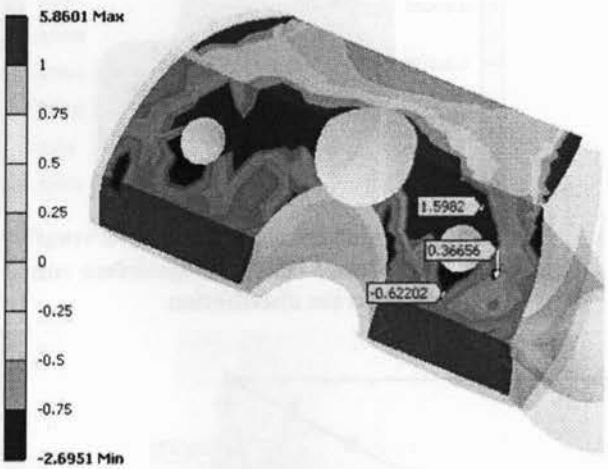

a) Maximum Principal stress [MPa]

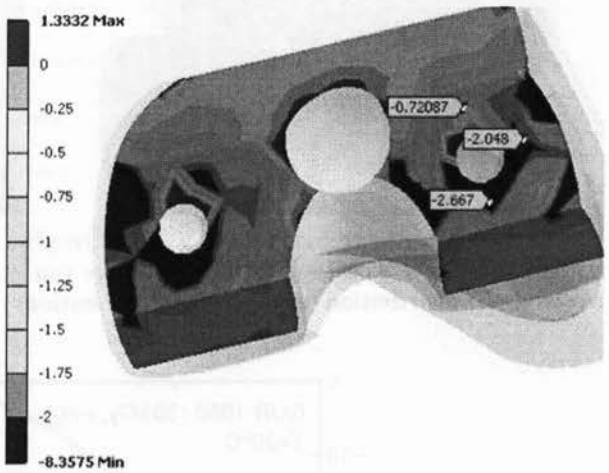

b) Minimum Principal stress [MPa]

Figure D.2 Hybrid design Maximum and Minimum Principal stress at zero flexion

	Maximum principal stress (MPa)		Minimum principal stress (MPa)	
	Upper limit	**Lower limit**	**Upper limit**	**Lower limit**
Conventional	1.6003	-4.5972	0.2757	-10.1115
Hybrid	5.8601	-2.6951	1.3332	-8.3575
Increase (%)	**266.19**	**-41.38**	**383.50**	**-17.35**

Table D.1 Condylar surface principal stresses [MPa] for 0° flexion

REFERENCES

[1] Dictionary.com, *Dictionary.com Unabridged (v 1.1).* Random House, Inc, Accessed January 3, 2009, <http://dictionary.reference.com>.

[2] Bartel, D.L., Davy, D.T., and Keaveny, T.M., 2006. *Orthopaedic Biomechanics: Mechanics and Design in Musculoskeletal Systems,* Pearson Prentice Hall, Upper Saddle River, NJ. 370 p.

[3] Carr, B. C., and Goswami, T., 2009. "Knee Implants – Review of Models and Biomechanics," *Materials & Design,* **30**(2) pp. 398-413.

[4] Insall, J.N., and Clarke, H.D., 2001. "Historic development, classification, and characteristics of knee prostheses," in *Surgery of the Knee,* J. N. Insall and W. N. Scott (eds). (Vol. 2) 3rd Ed. Churchill Livingstone, Philadelphia, PA. pp. 1516-1552, Chap. 73.

[5] Canadian Institute for Health Information (CIHI), 2008. *"Canadian Joint Replacement Registry (CJRR) 2007 Annual Report: Hip and Knee Replacements in Canada,"* CIHI and Canadian Orthopaedic Association, Ottawa, ON. ISBN 978-1-55465-189-4, Available at <http://secure.cihi.ca/cihiweb/dispPage.jsp?cw_page=PG_835_E&cw_topic=835&cw_rel=AR_30_E#full>.

[6] Balamurugan, A., Rajeswari, S., Balossier, G., Rebelo, A. H. S., and Ferreira, J. M. F., 2008. "Corrosion Aspects of Metallic Implants - an Overview," *Materials and Corrosion,* **59**(11) pp. 855-869.

[7] Kurtz, S. M., Lau, E., Ong, K., Zhao, K., Kelly, M., and Bozic, K., 2009. "Younger Patient Demand for Primary and Revision Joint Replacement: National Projections from 2010 to 2030," *The Journal of Arthroplasty,* **24**(2) pp. e34-e34.

[8] Petersen, M. M., Olsen, C., Lauritzen, J. B., and Lund, B., 1995. "Changes in Bone Mineral Density of the Distal Femur Following Uncemented Total Knee Arthroplasty," *The Journal of Arthroplasty,* **10**(1) pp. 7-12.

[9] Tayton, K., Phillips, G., and Ralis, Z., 1982. "Long-Term Effects of Carbon Fibre on Soft Tissues," *Journal of Bone and Joint Surgery (British),* **64**(1) pp. 112-114.

[10] Christel, P., Claes, L., and Brown, S.A., 1991. "Carbon reinforced composites in orthopedic surgery," in *High Performance Biomaterials: A Comprehensive Guide to Medical and Pharmaceutical Applications,* M. Szycher (ed). Technomic Publishing Company, Inc, Lancaster, PA. pp. 499-518, Chap. 32.

[11] Gupta, S. K., Chu, A., Ranawat, A. S., Slamin, J., and Ranawat, C. S., 2007. "Review Article: Osteolysis After Total Knee Arthroplasty," *The Journal of Arthroplasty,* **22**(6) pp. 787-799.

[12] Huiskes, R., Weinans, H., Grootenboer, H. J., Dalstra, M., Fudala, B., and Slooff, T. J., 1987. "Adaptive Bone-Remodeling Theory Applied to Prosthetic-Design Analysis," *Journal of Biomechanics,* **20**(11-12) pp. 1135-1150.

[13] Huiskes, R., Weinans, H., and Van Rietbergen, B., 1992. "The Relationship between Stress Shielding and Bone Resorption Around Total Hip Stems and the Effects of Flexible Materials," *Clinical Orthopaedics and Related Research,* (274) pp. 124-134.

[14] Walker, P. S., Granholm, J., and Lowrey, R., 1982. "The Fixation of Femoral Components of Condylar Knee Prostheses," *Engineering Medicine,* **11**(3) pp. 135-140.

[15] Angelides, M., Chan, K., Ahmed, A. M., and Joly, L., 1988. "Effect of Total Knee Arthroplasty on Distal Femur Stresses," *Transactions of the Orthopaedic Research Society,* **13** pp. 475.

[16] Tissakht, M., Ahmed, A. M., and Chan, K. C., 1996. "Calculated Stress-Shielding in the Distal Femur After Total Knee Replacement Corresponds to the Reported Location of Bone Loss," *Journal of Orthopaedic Research,* **14**(5) pp. 778-785.

[17] Van Lenthe, G. H., De Waal Malefijt, M. C., and Huiskes, R., 1997. "Stress Shielding After Total Knee Replacement may Cause Bone Resorption in the Distal Femur," *Journal of Bone and Joint Surgery (British),* **79**(1) pp. 117-122.

[18] Naudie, D. D. R., Ammeen, D. J., Engh, G. A., and Rorabeck, C. H., 2007. "Wear and Osteolysis Around Total Knee Arthroplasty," *Journal of the American Academy of Orthopaedic Surgeons,* **15**(1) pp. 53-64.

[19] Cadambi, A., Engh, G. A., Dwyer, K. A., and Vinh, T. N., 1994. "Osteolysis of the Distal Femur After Total Knee Arthroplasty," *The Journal of Arthroplasty,* **9**(6) pp. 579-594.

[20] Soininvaara, T. A., Miettinen, H. J. A., Jurvelin, J. S., Suomalainen, O. T., Alhava, E. M., and Kröger, H. P. J., 2004. "Periprosthetic Femoral Bone Loss After Total Knee Arthroplasty: 1-Year Follow-Up Study of 69 Patients," *The Knee,* **11**(4) pp. 297-302.

[21] van Loon, C. J. M., de Waal Malefijt, M. C., Buma, P., Verdonschot, N., and Veth, R. P. H., 1999. "Femoral Bone Loss in Total Knee Arthroplasty. A Review," *Acta Orthopaedica Belgica,* **65**(2) pp. 154-163.

[22] Robertson, D. D., Mintzer, C. M., Weissman, B. N., Ewald, F. C., LeBoff, M., and Spector, M., 1994. "Distal Loss of Femoral Bone Following Total Knee Arthroplasty. Measurement with Visual and Computer-Processing of Roentgenograms and Dual-Energy x-Ray Absorptiometry," *Journal of Bone and Joint Surgery (American),* **76**(1) pp. 66-76.

[23] Mintzer, C. M., Robertson, D. D., Rackemann, S., Ewald, F. C., Scott, R. D., and Spector, M., 1990. "Bone Loss in the Distal Anterior Femur After Total Knee Arthroplasty," *Clinical Orthopaedics and Related Research,* (260) pp. 135-143.

[24] van Loon, C. J. M., Oyen, W. J. G., deWaal Malefijt, M. C., and Verdonschot, N., 2001. "Distal Femoral Bone Mineral Density After Total Knee Arthroplasty: A Comparison with General Bone Mineral Density," *Archives of Orthopaedic and Trauma Surgery,* **121**(5) pp. 282-285.

[25] Stulberg, S. D., 2003. "Bone Loss in Revision Total Knee Arthroplasty: Graft Options and Adjuncts," *The Journal of Arthroplasty,* **18**(3, Part 2) pp. 48-50.

[26] Lonner, J. H., Klotz, M., Levitz, C., and Lotke, P. A., 2001. "Changes in Bone Density After Cemented Total Knee Arthroplasty: Influence of Stem Design," *The Journal of Arthroplasty,* **16**(1) pp. 107-111.

[27] Au, A. G., James Raso, V., Liggins, A. B., and Amirfazli, A., 2007. "Contribution of Loading Conditions and Material Properties to Stress Shielding Near the Tibial Component of Total Knee Replacements," *Journal of Biomechanics,* **40**(6) pp. 1410-1416.

[28] Completo, A., Fonseca, F., and Simões, J. A., 2008. "Strain Shielding in Proximal Tibia of Stemmed Knee Prosthesis: Experimental Study," *Journal of Biomechanics,* **41**(3) pp. 560-566.

[29] Hernandez-Vaquero, D., Garcia-Sandoval, M., Fernandez-Carreira, J., and Gava, R., 2008. "Influence of the Tibial Stem Design on Bone Density After Cemented Total Knee Arthroplasty: A Prospective Seven-Year Follow-Up Study," *International Orthopaedics,* **32**(1) pp. 47-51.

[30] Completo, A., Talaia, P., Fonseca, F., and Simões, J. A., 2009. "Relationship of Design Features of Stemmed Tibial Knee Prosthesis with Stress Shielding and End-of-Stem Pain," *Materials & Design,* **30**(4) pp. 1391-1397.

[31] Sathappan, S., Pang, H., Manoj, A., Ashwin, T., and Satku, K., 2009. "Does Stress Shielding Occur with the use of Long-Stem Prosthesis in Total Knee Arthroplasty?" *Knee Surgery, Sports Traumatology, Arthroscopy,* **17**(2) pp. 179-183.

[32] American Association of Hip and Knee Surgeons, 2007. "Knee Implants," *www.aaos.org.* American Academy of Orthopaedic Surgeons, Accessed January 5, 2009, <http://orthoinfo.aaos.org/topic.cfm?topic=A00221>.

[33] Morscher, E., and Mathys, R., 1974. "Isoelastic Total Prosthesis of the Hip Fixed without Cement: First Results," *Acta Orthopaedica Belgica,* **40**(5-6) pp. 639-647.

[34] Bombelli, R., and Mathys, R., 1982. "Cementless Isoelastic RM Total Hip Prosthesis," *Journal of the Royal Society of Medicine,* **75**(8) pp. 588-597.

[35] Skinner, H. B., 1991. "Isoelasticity and Total Hip Arthroplasty," *Orthopedics,* **14**(3) pp. 323-328.

[36] Niinimaki, T., Puranen, J., and Jalovaara, P., 1994. "Total Hip Arthroplasty using Isoelastic Femoral Stems. A Seven- to Nine-Year Follow-Up in 108 Patients," *Journal of Bone and Joint Surgery (British),* **76-B**(3) pp. 413-418.

[37] De Groot, K., Wen, H. B., Liu, Y., Layrolle, P., and Barrere, F., 2000. "Biomimetic Coatings on Orthopedic Implants: A Review," *Materials Research Society Symposium - Proceedings,* **599** pp. 109-116.

[38] Campbell, M., Bureau, M. N., Bougherara, H. A., Denault, J., and Yahia, L. H., 2006. "Biomimetic polymer composites for orthopedic implants," *Proceedings of the Annual Technical Conference (ANTEC) at Charlotte, NC,* Anonymous Society of Plastics Engineers (SPC), **1,** pp. 158-162.

[39] Campbell, M., Bougherara, H. A., Yahia, L., Bureau, M. N., Legoux, J. G., and Denault, J., 2006. "Biomimetic polymer composites for orthopedic hip implants," *Medical Device Materials III:*

Proceedings of Materials & Processes for Medical Devices Conference at Boston, MA, November 14-16, 2005, R. Venugopalan and M. Wu, eds. ASM International, pp. 49-54.

[40] Campbell, M., Denault, J., Yahia, L., and Bureau, M. N., 2008. "CF/PA12 Composite Femoral Stems: Manufacturing and Properties," *Composites Part A: Applied Science and Manufacturing,* **39**(5) pp. 796-804.

[41] Campbell, M., Bureau, M., and Yahia, L., 2008. "Performance of CF/PA12 Composite Femoral Stems," *Journal of Materials Science: Materials in Medicine,* **19**(2) pp. 683-693.

[42] Bougherara, H., Bureau, M., Campbell, M., Vadean, A., and Yahia, L., 2007. "Design of a Biomimetic Polymer-Composite Hip Prosthesis," *Journal of Biomedical Materials Research Part A,* **82A**(1) pp. 27-40.

[43] Robinson, R. P., 2005. "The Early Innovators of Today's Resurfacing Condylar Knees," *The Journal of Arthroplasty,* **20**(Supplement 1) pp. 2-26.

[44] Scott, R.D., 2006. *Total Knee Arthroplasty,* Saunders Elsevier, Philadelphia, PA. 148 p.

[45] Hohler, S. E., 2008. "Total Knee Arthroplasty: Past Successes and Current Improvements," *The Association of periOperative Registered Nurses Journal,* **87**(1) pp. 143-162.

[46] Stryker Corporation, 2009. "Duracon Total Stabilizer Knee System," *Stryker.com (Stryker Orthopaedics: Knee Replacement System).* Stryker Corporation, Kalamazoo, MI. Accessed January, 5, 2009, <http://www.stryker.com/en-us/products/Orthopaedics/KneeReplacement/Revision/DuraconTS/index.htm#>.

[47] University of Minnesota, 2008. "Anatomy Tutorial: Anatomic Positions," *Atlas of Human Cardiac Anatomy.* Regents of the University of Minnesota, Accessed January 15, 2009, <http://www.vhlab.umn.edu/atlas/anatutorial/anatutorial1.shtml>.

[48] Martini, F.H., Timmons, M.J., and Tallitsch, R.B., 2008. *Human Anatomy,* 6th Edition. Pearson Benjamin Cummings, Upper Saddle River, NJ. 869 p.

[49] Fitt, S.S., 1996. *Dance Kinesiology,* 2nd Edition. Schirmer Books, New York, NY. 484 p.

[50] American Association of Hip and Knee Surgeons, 2007. "Total Knee Replacement," *www.aaos.org.* American Academy of Orthopaedic Surgeons, Accessed January 5, 2009, <http://orthoinfo.aaos.org/topic.cfm?topic=A00389>.

[51] Felson, D. T., Lawrence, R. C., Dieppe, P. A., Hirsch, R., Helmick, C. G., Jordan, J. M., Kington, R. S., Lane, N. E., Nevitt, M. C., Zhang, Y., Sowers, M., McAlindon, T., Spector, T. D., Poole, A. R., Yanovski, S. Z., Ateshian, G., Sharma, L., Buckwalter, J. A., Brandt, K. D., and Fries, J. F., 2000. "Osteoarthritis - New Insights. Part 1: The Disease and its Risk Factors," *Annals of Internal Medicine,* **133** pp. 635-646.

[52] Union Hospitals, 2006. "Unispacer Knee Replacement," *Union Hospitals Center of Orthopedic Surgery.* Accessed January 18, 2009,

<http://unionhospitals.com/ORTHOPEADIC%20SURGERY/UNISPACER%20KNEE%20REPLACEMENT_LINK.htm>.

[53] Deluzio, K., "Knee Osteoarthritis," *Mechanical and Materials Engineering, Faculty of Applied Science.* Queen's University, Kingston, ON. Accessed January 11, 2009, <http://me.queensu.ca/people/deluzio/KneeOsteoarthritis.php>.

[54] Thompson, D. M., 2002. "Introduction to the Study of Human Walking: Basics of Gait Terminology," *Lectures on the Control of Human Movement.* Department of Biostatics and Epidemiology, University of Oklahoma Health Sciences Centre, Accessed January 8, 2009, <http://moon.ouhsc.edu/dthompso/gait/terms.htm>.

[55] Seedhom, B. B., and Wallbridge, N. C., 1985. "Walking Activities and Wear of Prostheses." *Annals of Rheumatic Disease,* **44**(12) pp. 838-843.

[56] Kaufman, K.R., and Sutherland, D.H., 2006. "Kinematics of Normal Human Walking: Gait events," in *Human Walking,* J. Rose and J. G. Gamble (eds). 3rd Ed. Lippincott Williams & Wilkins, Philadelphia, PA. pp. 39-42, Chap. 3.

[57] Deluzio, K., "Gait Analysis," *Mechanical and Materials Engineering, Faculty of Applied Science.* Queen's University, Kingston, ON. Accessed January 11, 2009, <http://me.queensu.ca/people/deluzio/GaitAnalysis.php>.

[58] Gage, J. R., 1990. "An Overview of Normal Walking," *Instructional Course Lectures,* **39** pp. 291-303.

[59] Clarke, H.D., Scott, W.N., Insall, J.N., Pedersen, H.B., Math, K.R., Vigorita, V.J., and Cushner, F.D., 2001. "Anatomy: Motion and Function," in *Surgery of the Knee,* J. N. Insall and W. N. Scott (eds). (Vol. 1) 3rd Ed. Churchill Livingstone, New York, NY. pp. 71-74, Chap. 2.

[60] Eberhart, H.D., Inman, V.T., and Saunders, J.B., 1947. *"Fundamental studies of human locomotion and other information relating to design of artificial limbs,"* Report to the National Research Council, USA. University of California, Berkeley, CA.

[61] Andriacchi, T. P., and Alexander, E. J., 2000. "Studies of Human Locomotion: Past, Present and Future," *Journal of Biomechanics,* **33**(10) pp. 1217-1224.

[62] Pauwels, F., 1935. *Der Schenkelhalsbruck ein Mechanische Problem,* Ferd. Encke., Stuttgart, Germany.

[63] Rasch, P. J., 1958. "Notes Toward a History of Kinesiology I," *Journal of the American Osteopathic Association,* **57**(9) pp. 572-574.

[64] Rasch, P. J., 1958. "Notes Toward a History of Kinesiology II," *Journal of the American Osteopathic Association,* **57**(10) pp. 641-644.

[65] Paul, J. P., 1976. "Approaches to Design: Force Actions Transmitted by Joints in the Human Body," *Proceedings of the Royal Society of London - Series B, Biological Sciences,* **192**(1107, A Discussion on the Treatment of Arthritis by Joint Replacement) pp. 163-172.

[66] Winter, D. A., 1980. "Overall Principle of Lower Limb Support during Stance Phase of Gait," *Journal of Biomechanics,* **13**(11) pp. 923-927.

[67] Sutherland, D. H., Olshen, R., Cooper, L., and Woo, S. L., 1980. "The Development of Mature Gait," *Journal of Bone and Joint Surgery (American),* **62**(3) pp. 336-353.

[68] Morrison, J. B., 1970. "The Mechanics of the Knee Joint in Relation to Normal Walking," *Journal of Biomechanics,* **3**(1) pp. 51-61.

[69] Paul, J. P., 1970. "The Effect of Walking Speed on the Force Actions Transmitted at the Hip and Knee Joints." *Proceedings of the Royal Society of Medicine,* **63**(2) pp. 200-202.

[70] Denham, R. A., and Bishop, R. E., 1978. "Mechanics of the Knee and Problems in Reconstructive Surgery," *Journal of Bone and Joint Surgery (British),* **60-B**(3) pp. 345-352.

[71] Paul, J. P., 1982. "Biomechanics of the Leg in Relation to Joint Replacement," *Medical Progress through Technology,* **9**(2-3) pp. 137-140.

[72] Ruff, C. B., and Hayes, W. C., 1984. "Bone-Mineral Content in the Lower Limb: Relationship to Cross-Sectional Geometry," *Journal of Bone and Joint Surgery (American),* **66**(7) pp. 1024-1031.

[73] Ruff, C. B., and Hayes, W. C., 1984. "Age Changes in Geometry and Mineral Content of the Lower Limb Bones," *Annals of Biomedical Engineering,* **12**(6) pp. 573-584.

[74] Reilly, D. T., and Burstein, A. H., 1974. "The Mechanical Properties of Cortical Bone," *Journal of Bone and Joint Surgery (American),* **56**(5) pp. 1001-1022.

[75] Reilly, D. T., and Burstein, A. H., 1975. "The Elastic and Ultimate Properties of Compact Bone Tissue," *Journal of Biomechanics,* **8**(6) pp. 393-396.

[76] Wirtz, D. C., Schiffers, N., Pandorf, T., Radermacher, K., Weichert, D., and Forst, R., 2000. "Critical Evaluation of Known Bone Material Properties to Realize Anisotropic FE-Simulation of the Proximal Femur," *Journal of Biomechanics,* **33**(10) pp. 1325-1330.

[77] Fondrk, M., Bahniuk, E., Davy, D. T., and Michaels, C., 1988. "Some Viscoplastic Characteristics of Bovine and Human Cortical Bone," *Journal of Biomechanics,* **21**(8) pp. 623-630.

[78] McElhaney, J. H., 1966. "Dynamic Response of Bone and Muscle Tissue." *Journal of Applied Physiology,* **21**(4) pp. 1231-1236.

[79] Goldstein, S. A., 1987. "The Mechanical Properties of Trabecular Bone: Dependence on Anatomic Location and Function," *Journal of Biomechanics,* **20**(11-12) pp. 1055-1061.

[80] Goulet, R. W., Goldstein, S. A., Ciarelli, M. J., Kuhn, J. L., Brown, M. B., and Feldkamp, L. A., 1994. "The Relationship between the Structural and Orthogonal Compressive Properties of Trabecular Bone," *Journal of Biomechanics,* **27**(4) pp. 375-377.

[81] Kopperdahl, D. L., and Keaveny, T. M., 1998. "Yield Strain Behavior of Trabecular Bone," *Journal of Biomechanics,* **31**(7) pp. 601-608.

[82] Goldstein, S. A., Wilson, D. L., Sonstegard, D. A., and Matthews, L. S., 1983. "The Mechanical Properties of Human Tibial Trabecular Bone as a Function of Metaphyseal Location," *Journal of Biomechanics,* **16**(12) pp. 965-969.

[83] Ciarelli, M. J., Goldstein, S. A., Kuhn, J. L., Cody, D. D., and Brown, M. B., 1991. "Evaluation of Orthogonal Mechanical Properties and Density of Human Trabecular Bone from the Major Metaphyseal Regions with Materials Testing and Computed Tomography," *Journal of Orthopaedic Research,* **9**(5) pp. 674-682.

[84] Chamay, A., and Tschantz, P., 1972. "Mechanical Influences in Bone Remodeling. Experimental Research on Wolff's Law," *Journal of Biomechanics,* **5**(2) pp. 173-180.

[85] Woo, S. L. Y., Kuei, S. C., and Amiel, D., 1981. "The Effect of Prolonged Physical Training on the Properties of Long Bone: A Study of Wolff's Law," *Journal of Bone and Joint Surgery (American),* **63**(5) pp. 780-787.

[86] Treharne, R. W., 1981. "Review of Wolff's Law and its Proposed Means of Operation," *Orthopaedic Review,* **10**(1) pp. 35-47.

[87] Cowin, S. C., 1986. "Wolff's Law of Trabecular Architecture at Remodeling Equilibrium," *Journal of Biomechanical Engineering,* **108**(1) pp. 83-88.

[88] Behrens, J. C., Walker, P. S., and Shoji, H., 1974. "Variations in Strength and Structure of Cancellous Bone at the Knee," *Journal of Biomechanics,* **7**(3) pp. 201-207.

[89] Lindahl, O., 1976. "Mechanical Properties of Dried Defatted Spongy Bone," *Acta Orthopaedica Scandinavica,* **47**(1) pp. 11-19.

[90] Carter, D. R., and Hayes, W. C., 1977. "The Compressive Behavior of Bone as a Two-Phase Porous Structure," *Journal of Bone and Joint Surgery (American),* **59**(7) pp. 954-962.

[91] Williams, J. L., and Lewis, J. L., 1982. "Properties and an Anisotropic Model of Cancellous Bone from the Proximal Tibial Epiphysis," *Journal of Biomedical Engineering,* **104**(1) pp. 50-56.

[92] Hvid, I., and Hansen, S. L., 1985. "Trabecular Bone Strength Patterns at the Proximal Tibial Epiphysis," *Journal of Orthopaedic Research,* **3**(4) pp. 464-472.

[93] Ciarelli, M. J., Goldstein, S. A., and Dickie, D., 1986. "Experimental Determination of the Orthogonal Mechanical Properties, Density and Distribution of Human Trabecular Bone from the Major Metaphyseal Regions Utilizing Material Testing and Computed Tomography," *Transactions of the Orthopaedic Research Society,* pp. 42.

[94] Linde, F., and Hvid, I., 1989. "The Effect of Constraint on the Mechanical Behaviour of Trabecular Bone Specimens," *Journal of Biomechanics,* **22**(5) pp. 485-490.

[95] Ashman, R. B., Rho, J. Y., and Turner, C. H., 1989. "Anatomical Variation of Orthotropic Elastic Moduli of the Proximal Human Tibia," *Journal of Biomechanics,* **22**(8-9) pp. 895-900.

[96] Pugh, J. W., Rose, R. M., and Radin, E. L., 1973. "Elastic and Viscoelastic Properties of Trabecular Bone: Dependence on Structure," *Journal of Biomechanics,* **6**(5) pp. 475-478.

[97] Ducheyne, P., Heymans, L., Martens, M., Aernoudt, E., de Meester, P., and Mulier, J. C., 1977. "The Mechanical Behaviour of Intracondylar Cancellous Bone of the Femur at Different Loading Rates," *Journal of Biomechanics,* **10**(11-12) pp. 747-762.

[98] Rohlmann, A., Zilch, H., Bergmann, G., and Kolbel, R., 1980. "Material Properties of Femoral Cancellous Bone in Axial Loading. PartI: Time-Independent Properties," *Archives of Orthopaedic and Trauma Surgery,* **97**(2) pp. 95-102.

[99] Brekelmans, W. A. M., Poort, H. W., and Slooff, T. J. J. H., 1972. "A New Method to Analyse the Mechanical Behaviour of Skeletal Parts," *Acta Orthopaedica,* **43**(5) pp. 301 AB.

[100] Valliappan, S., Svensson, N. L., and Wood, R. D., 1977. "Three Dimensional Stress Analysis of the Human Femur," *Computers in Biology and Medicine,* **7**(4) pp. 253-264.

[101] Huiskes, R., 1982. "On the Modelling of Long Bones in Structural Analyses," *Journal of Biomechanics,* **15**(1) pp. 65-69.

[102] Cheal, E. J., Hayes, W. C., White, A. A., and Perren, S. M., 1985. "Stress Analysis of Compression Plate Fixation and its Effects on Long Bone Remodeling," *Journal of Biomechanics,* **18**(2) pp. 141-150.

[103] Cheal, E. J., Spector, M., and Hayes, W. C., 1992. "Role of Loads and Prosthesis Material Properties on the Mechanics of the Proximal Femur After Total Hip Arthroplasty," *Journal of Orthopaedic Research,* **10**(3) pp. 405-422.

[104] McNamara, B. P., Cristofolini, L., Toni, A., and Taylor, D., 1997. "Relationship between Bone-Prosthesis Bonding and Load Transfer in Total Hip Reconstruction," *Journal of Biomechanics,* **30**(6) pp. 621-630.

[105] Taylor, M. E., Tanner, K. E., Freeman, M. A. R., and Yettram, A. L., 1996. "Stress and Strain Distribution within the Intact Femur: Compression Or Bending?" *Medical Engineering & Physics,* **18**(2) pp. 122-131.

[106] Zdero, R., Olsen, M., Bougherara, H., and Schemitsch, E. H., 2008. "Cancellous Bone Screw Purchase: A Comparison of Synthetic Femurs, Human Femurs, and Finite Element Analysis," *Proceedings of the Institution of Mechanical Engineers - Part H: Journal of Engineering in Medicine,* **222** pp. 1175-1183(9).

[107] Papini, M., Zdero, R., Schemitsch, E. H., and Zalzal, P., 2007. "The Biomechanics of Human Femurs in Axial and Torsional Loading: Comparison of Finite Element Analysis, Human Cadaveric Femurs, and Synthetic Femurs," *Journal of Biomechanical Engineering,* **129**(1) pp. 12-19.

[108] Chong, A. C. M., Friis, E. A., Ballard, G. P., Czuwala, P. J., and Cooke, F. W., 2007. "Fatigue Performance of Composite Analogue Femur Constructs Under High Activity Loading," *Annals of Biomedical Engineering,* **35**(7) pp. 1196-1205.

[109] Chong, A. C. M., Miller, F., Buxton, M., and Friis, E. A., 2007. "Fracture Toughness and Fatigue Crack Propagation Rate of Short Fiber Reinforced Epoxy Composites for Analogue Cortical Bone," *Journal of Biomechanical Engineering,* **129**(4) pp. 487-493.

[110] Cristofolini, L., Viceconti, M., Cappello, A., and Toni, A., 1996. "Mechanical Validation of Whole Bone Composite Femur Models," *Journal of Biomechanics,* **29**(4) pp. 525-535.

[111] Sawbones Worldwide, 2009. "Composite Bones: Typical Properties," *Sawbones.com.* Pacific Research Laboratories, Inc, Accessed January 16, 2009, <http://www.sawbones.com/products/bio/composite.aspx>.

[112] Heiner, A. D., and Brown, T. D., 2001. "Structural Properties of a New Design of Composite Replicate Femurs and Tibias," *Journal of Biomechanics,* **34**(6) pp. 773-781.

[113] Szivek, J. A., and Gealer, R. L., 1991. "Technical Note. Comparison of the Deformation Response of Synthetic and Cadaveric Femora during Simulated One-Legged Stance," *Journal of Applied Biomaterials,* **2**(4) pp. 277-280.

[114] McNamara, B. P., Cristofolini, L., Toni, A., and Taylor, D., 1994. "Evaluation of Experimental and Finite Element Models of Synthetic and Cadaveric Femora for Pre-Clinical Design-Analysis," *Clinical Materials,* **17**(3) pp. 131-140.

[115] Sawbones Worldwide, 2009. "Medium Left Fourth Generation Composite Femur (Item #3403)," *Sawbones.com.* Pacific Research Laboratories, Inc., Vashon, WA, USA. Accessed January 11, 2009, <http://www.sawbones.com/products/product.aspx?1936>.

[116] Ferguson, W., 1861. "Excision of the Knee Joint. Recovery with a False Joint and a Useful Limb," *Medical Times Gazette,* **1** pp. 601.

[117] Campbell, W. C., 2005. "The Classic: Interposition of Vitallium Plates in Arthroplasties of the Knee - Preliminary Report (1940)," *Clinical Orthopaedics and Related Research,* **440** pp. 22-23.

[118] Palmer, S. H., and Cross, M. J., 2004. "Total Knee Arthroplasty," *eMedicine from WebMD.* Medscape, Accessed January 5, 2009, <http://emedicine.medscape.com/article/1250275-print>.

[119] McKeever, D. C., 2005. "The Classic: Tibial Plateau Prosthesis (1960)," *Clinical Orthopaedics and Related Research,* **440** pp. 4-8.

[120] Walldius, B., 1996. "Arthroplasty of the Knee using an Endoprosthesis (1957)," *Clinical Orthopaedics and Related Research,* (331) pp. 4-10.

[121] McAllister, C. M., 2008. "The Role of Unicompartmental Knee Arthroplasty Versus Total Knee Arthroplasty in Providing Maximal Performance and Satisfaction." *Journal of Knee Surgery,* **21**(4) pp. 286-292.

[122] Swanson, S. A., and Freeman, M. A., 1972. "A New Prosthesis for the Total Replacement of the Knee." *Acta Orthopaedica Belgica,* **38, Suppl. 1** pp. 55-62.

[123] Freeman, M. A. R., Swanson, S. A. V., and Todd, R. C., 1973. "Total Replacement of the Knee using the Freeman Swanson Knee Prosthesis," *Clinical Orthopaedics,* **94** pp. 153-170.

[124] Swanson, S. A. V., and Freeman, M. A. R., 1974. "The Design of a Knee Joint Implant," *Bio-Medical Engineering,* **9**(8) pp. 348-352.

[125] Yamamoto, S., 1979. "Total Knee Replacement with the Kodema-Yamamoto Knee Prosthesis," *Clinical Orthopaedics and Related Research,* **145** pp. 60-67.

[126] Yamamoto, S., Hachinota, M., and Nakata, S., 1984. "The Kodama-Yamamoto Knee Prostheses, the Mark is and Mark II," *Japanese Journal of Artificial Organs,* **13**(3) pp. 1083-1086.

[127] Buechel, F. F., and Pappas, M. J., 1989. "New Jersey Low Contact Stress Knee Replacement System. Ten-Year Evaluation of Meniscal Bearings," *Orthopedic Clinics of North America,* **20**(2) pp. 147-177.

[128] Buechel Sr., F. F., Buechel Jr., F. F., Pappas, M. J., and Dalessio, J., 2002. "Twenty-Year Evaluation of the New Jersey LCS Rotating Platform Knee Replacement." *The Journal of Knee Surgery,* **15**(2) pp. [d]84-89.

[129] Hungerford, D. S., Kenna, R. V., and Krackow, K. A., 1982. "The Porous-Coated Anatomic Total Knee," *Orthopedic Clinics of North America,* **13**(1) pp. 103-122.

[130] Kurtz, S.M., 2004. "The clinical performance of UHMWPE in knee replacements," in *The UHMWPE Handbook: Ultra-High Molecular Weight Polyethylene in Joint Replacement,* Anonymous Elsevier Academic Press, San Diego, CA. pp. 151-188, Chap. 8.

[131] Stryker Corporation, 2009. "Knee Replacement," *Stryker.com (Stryker Solutions).* Stryker Corporation, Kalamazoo, MI. Accessed January 11, 2009, <http://www.stryker.com/en-us/Solutions/KneeReplacement/index.htm>.

[132] Tokash, J. C., Stojilovic, N., Ramsier, R. D., Kovacik, M. W., and Mostardi, R. A., 2005. "Surface Analysis of Prosthetic Wear Debris," *Surface and Interface Analysis,* **37**(4) pp. 379-384.

[133] Fregly, B. J., Sawyer, W. G., Harman, M. K., and Banks, S. A., 2005. "Computational Wear Prediction of a Total Knee Replacement from in Vivo Kinematics," *Journal of Biomechanics,* **38**(2) pp. 305-314.

[134] Alhassan, S., and Goswami, T., 2008. "Wear Rate Model for UHMWPE in Total Joint Applications," *Wear,* **265**(1-2) pp. 8-13.

[135] Goswami, T., and Alhassan, S., 2008. "Wear Rate Model for UHMWPE in Total Hip and Knee Arthroplasty," *Materials & Design,* **29**(2) pp. 289-296.

[136] Pilliar, R. M., Lee, J. M., and Maniatopoulos, C., 1986. "Observations on the Effect of Movement on Bone Ingrowth into Porous-Surfaced Implants," *Clinical Orthopaedics and Related Research,* **208** pp. 108-113.

[137] Skripitz, R., and Aspenberg, P., 1998. "Tensile Bond between Bone and Titanium. A Reappraisal of Osseointegration," *Acta Orthopaedica Scandinavica,* **69**(3) pp. 315-319.

[138] Nielsen, P. T., Hansen, E. B., and Rechnagel, K., 1992. "Cementless Total Knee Arthroplasty in Unselected Cases of Osteoarthritis and Rheumatoid Arthritis: A 3-Year Follow-Up Study of 103 Cases," *The Journal of Arthroplasty,* **7**(2) pp. 137-143.

[139] Rakotomanana, R. L., Leyvraz, P. F., Curnier, A., Heegaard, J. H., and Rubin, P. J., 1992. "A Finite Element Model for Evaluation of Tibial Prosthesis-Bone Interface in Total Knee Replacement," *Journal of Biomechanics,* **25**(12) pp. 1413-1424.

[140] Van Rietbergen, B., Huiskes, R., Weinans, H., Sumner, D. R., Turner, T. M., and Galante, J. O., 1993. "The Mechanism of Bone Remodeling and Resorption Around Press-Fitted Total Hip Arthroplasty Stems," *Journal of Biomechanics,* **26**(4-5) pp. 369-382.

[141] Van Lenthe, G. H., Willems, M. M. M., Verdonschot, N., De Waal Malefijt, M. C., and Huiskes, R., 2002. "Stemmed Femoral Knee Prostheses: Effects of Prosthetic Design and Fixation on Bone Loss," *Acta Orthopaedica Scandinavica,* **73**(6) pp. 630-637.

[142] Paul, J. P., 1999. "Strength Requirements for Internal and External Prostheses," *Journal of Biomechanics,* **32**(4) pp. 381-393.

[143] Mudali, U. K., Sridhar, T. M., and Baldev, R. A. J., 2003. "Corrosion of Bio Implants," *Sadhana - Academy Proceedings in Engineering Sciences,* **28**(3-4) pp. 601-637.

[144] Villa, T., Migliavacca, F., Gastaldi, D., Colombo, M., and Pietrabissa, R., 2004. "Contact Stresses and Fatigue Life in a Knee Prosthesis: Comparison between in Vitro Measurements and Computational Simulations," *Journal of Biomechanics,* **37**(1) pp. 45-53.

[145] Goswami, T., 2003. "Fatigue Crack Growth Behavior of Ti-6Al-4V Alloy Forging," *Materials and Design,* **24**(6) pp. 423-433.

[146] Barrack, R. L., and Wolfe, M. W., 2000. "Patellar Resurfacing in Total Knee Arthroplasty," *Journal of the American Academy of Orthopaedic Surgeons,* **8**(2) pp. 75-82.

[147] Parvizi, J., Seel, M. J., Hanssen, A. D., Berry, D. J., and Morrey, B. F., 2002. "Patellar Component Resection Arthroplasty for the Severely Compromised Patella," *Clinical Orthopaedics and Related Research,* (397) pp. 356-361.

[148] Hanssen, A. D., 2001. "Bone-Grafting for Severe Patellar Bone Loss during Revision Knee Arthroplasty," *Journal of Bone and Joint Surgery (American),* **83**(2) pp. 171-176.

[149] Kurtz, S.M., 2004. *The UHMWPE Handbook: Ultra-high Molecular Weight Polyethylene in Total Joint Replacement,* Elsevier Academic Press, San Diego, CA. 379 p.

[150] Lombardi, A. V., Mallory, T. H., Staab, M., and Herrington, S. M., 1998. "Particulate Debris Presenting as Radiographic Dense Masses Following Total Knee Arthroplasty." *The Journal of Arthroplasty,* **13**(3) pp. 351-351-5.

[151] Cameron, H. U., and Cameron, G., 1987. "Stress-Relief Osteoporosis of the Anterior Femoral Condyles in Total Knee Replacement. A Study of 185 Patients." *Orthopaedic Review,* **16**(7) pp. 449-456.

[152] Hamlin, F. D., Buechel, F. F., and Pappas, M. J., 1993. "Stress Shielding as it Relates to Proximally Porous Coated Femoral Stems of Varying Configurations: A 10-Year Cementless Total Hip Replacement Study," *Journal of Orthopaedic Rheumatology,* **6**(2-3) pp. 57-70.

[153] Cristofolini, L., 1997. "A Critical Analysis of Stress Shielding Evaluation of Hip Prostheses," *Critical Reviews in Biomedical Engineering,* **25**(4-5) pp. 409-483.

[154] Gross, S., and Abel, E. W., 2001. "A Finite Element Analysis of Hollow Stemmed Hip Prostheses as a Means of Reducing Stress Shielding of the Femur," *Journal of Biomechanics,* **34**(8) pp. 995-1003.

[155] Adam, F., Hammer, D. S., Pfautsch, S., and Westermann, K., 2002. "Early Failure of a Press-Fit Carbon Fiber Hip Prosthesis with a Smooth Surface," *The Journal of Arthroplasty,* **17**(2) pp. 217-223.

[156] Kienapfel, H., Sprey, C., Wilke, A., and Griss, P., 1999. "Implant Fixation by Bone Ingrowth," *The Journal of Arthroplasty,* **14**(3) pp. 355-368.

[157] Schrøder, H. M., Berthelsen, A., Hassani, G., Hansen, E. B., and Solgaard, S., 2001. "Cementless Porous-Coated Total Knee Arthroplasty: 10-Year Results in a Consecutive Series," *The Journal of Arthroplasty,* **16**(5) pp. 559-567.

[158] Benjamin, J., Engh, G., Parsley, B., Donaldson, T., and Coon, T., 2001. "Morselized Bone Grafting of Defects in Revision Total Knee Arthroplasty," *Clinical Orthopaedics and Related Research,* (392) pp. 62-67.

[159] Harrysson, O. L. A., Hosni, Y. A., and Nayfeh, J. F., 2007. "Custom-Designed Orthopedic Implants Evaluated using Finite Element Analysis of Patient-Specific Computed Tomography Data: Femoral-Component Case Study," *BMC Musuloskeletal Disorders,* **8**(91) .

[160] Legoux, J. -., Chellat, F., Lima, R., Marple, B., Bureau, M. N., Shen, H., and Antonio Candeliere, G., 2006. "Development of Osteoblast Colonies on New Bioactive Coatings," *Journal of Thermal Spray Technology,* **15**(4) pp. 628-633.

[161] Ramakrishna, S., Mayer, J., Wintermantel, E., and Leong, K. W., 2001. "Biomedical Applications of Polymer-Composite Materials: A Review," *Composites Science and Technology,* **61**(9) pp. 1189-1224.

[162] Bartel, D. L., Bicknell, V. L., and Wright, T. M., 1986. "The Effect of Conformity, Thickness, and Material on Stresses in Ultra-High Molecular Weight Components for Total Joint Replacement," *Journal of Bone and Joint Surgery (American),* **68**(7) pp. 1041-1051.

[163] Ingham, E., and Fisher, J., 2000. "Biological Reactions to Wear Debris in Total Joint Replacement," *Proceedings of the Institution of Mechanical Engineers - Part H: Journal of Engineering in Medicine,* **214**(1) pp. 21-37.

[164] Kurtz, S. M., Villarraga, M. L., Herr, M. P., Bergström, J. S., Rimnac, C. M., and Edidin, A. A., 2002. "Thermomechanical Behavior of Virgin and Highly Crosslinked Ultra-High Molecular Weight Polyethylene used in Total Joint Replacements," *Biomaterials,* **23**(17) pp. 3681-3697.

[165] Bergström, J., 2004. "Computer Modeling and Simulation of UHMWPE," in *The UHMWPE Handbook: Ultra-High Molecular Weight Polyethylene in Total Joint Replacement,* S. M. Kurtz (ed). Elsevier Academic Press, San Diego, CA. pp. 309-336, Chap. 14.

[166] Bergström, J. S., Kurtz, S. M., Rimnac, C. M., and Edidin, A. A., 2002. "Constitutive Modeling of Ultra-High Molecular Weight Polyethylene Under Large-Deformation and Cyclic Loading Conditions," *Biomaterials,* **23**(11) pp. 2329-2343.

[167] Bergström, J. S., Rimnac, C. M., and Kurtz, S. M., 2003. "Prediction of Multiaxial Mechanical Behavior for Conventional and Highly Crosslinked UHMWPE using a Hybrid Constitutive Model," *Biomaterials,* **24**(8) pp. 1365-1380.

[168] Bergström, J. S., Rimnac, C. M., and Kurtz, S. M., 2004. "An Augmented Hybrid Constitutive Model for Simulation of Unloading and Cyclic Loading Behavior of Conventional and Highly Crosslinked UHMWPE," *Biomaterials,* **25**(11) pp. 2171-2178.

[169] Bergström, J. S., Rimnac, C. M., and Kurtz, S. M., 2005. "Molecular Chain Stretch is a Multiaxial Failure Criterion for Conventional and Highly Crosslinked UHMWPE," *Journal of Orthopaedic Research,* **23**(2) pp. 367-375.

[170] Ogden, R.W., 1997. *Non-linear elastic deformations,* Courier Dover Publications, Mineola, NY. xii, 532 p.

[171] Stryker Corporation, 2009. "Stryker X3 Advanced Bearing Technology: REFERENCES," *Stryker.com (Stryker Orthopaedics: Knee Replacement Systems).* Stryker Corporation, Kalamazoo, MI. Accessed January 11, 2009, <http://www.stryker.com/en-us/products/Orthopaedics/KneeReplacement/X3AdvancedBearingTechnology/index.htm>.

[172] Deopura, B.L., 2008. *Polyesters and polyamides,* Woodhead Publishing, in association with Textile Institute and CRC Press, Cambridge, UK. xxii, 608 p.

[173] Snyder, S. M., and Schneider, E., 1991. "Estimation of Mechanical Properties of Cortical Bone by Computed Tomography," *Journal of Orthopaedic Research,* **9**(3) pp. 422-431.

[174] Bougherara, H., Klika, V., Marîsík, F., Bureau, M. N., and Yahia, L., 2006. "Biomimetic hip prosthesis including bone remodeling process induced by dynamical loading," *Proceedings of the 7th International Symposium on Computer Methods in Biomechanics and Biomedical Engineering, 21-25th March,* Anonymous CMBBE, Juan les Pins, France, .

[175] Bougherara, H., Zdero, R., Miric, M., Shah, S., Hardisty, M., Zalzal, P., and Schemitsch, E. H., 2009. "The Biomechanics of the T2 Femoral Nailing System: A Comparison of Synthetic Femurs with Finite Element Analysis," *Proceedings of the Institution of Mechanical Engineers, Part H: Journal of Engineering in Medicine,* **223**(3) pp. 303-314.

[176] Ogden, C.L., Fryar, C.D., Carroll, M.D., and Flegal, K.M., 2004. *"Mean Body Weight, Height, and Body Mass Index, United States 1960–2002,"* Advance Data No. 347. Department of Health and Human Services, Centers for Disease Control and Prevention (CDC), National Centre for Health Statistics, USA. Available at <http://www.cdc.gov/nchs/data/ad/ad347.pdf>.

[177] Chu, T., 1999. "An Investigation on Contact Stresses of New Jersey Low Contact Stress (NJLCS) Knee using Finite Element Method," *Journal of Systems Integration,* **9**(2) pp. 187-199.

[178] Miyoshi, S., Takahashi, T., Ohtani, M., Yamamoto, H., and Kameyama, K., 2002. "Analysis of the Shape of the Tibial Tray in Total Knee Arthroplasty using a Three Dimension Finite Element Model," *Clinical Biomechanics,* **17**(7) pp. 521-525.

[179] Godest, A. C., Beaugonin, M., Haug, E., Taylor, M., and Gregson, P. J., 2002. "Simulation of a Knee Joint Replacement during a Gait Cycle using Explicit Finite Element Analysis," *Journal of Biomechanics,* **35**(2) pp. 267-275.

[180] Halloran, J. P., Petrella, A. J., and Rullkoetter, P. J., 2005. "Explicit Finite Element Modeling of Total Knee Replacement Mechanics," *Journal of Biomechanics,* **38**(2) pp. 323-331.

[181] Liau, J., Hu, C., Cheng, C., Huang, C., and Lo, W., 2001. "The Influence of Inserting a Fuji Pressure Sensitive Film between the Tibiofemoral Joint of Knee Prosthesis on Actual Contact Characteristics," *Clinical Biomechanics,* **16**(2) pp. 160-166.

[182] Liau, J., Cheng, C., Huang, C., and Lo, W., 2002. "Effect of Fuji Pressure Sensitive Film on Actual Contact Characteristics of Artificial Tibiofemoral Joint," *Clinical Biomechanics,* **17**(9-10) pp. 698-704.

[183] Liau, J., Cheng, C., Huang, C., and Lo, W., 2002. "The Effect of Malalignment on Stresses in Polyethylene Component of Total Knee Prostheses – a Finite Element Analysis," *Clinical Biomechanics,* **17**(2) pp. 140-146.

[184] Burstein, A. H., Currey, J. D., Frankel, V. H., and Reilly, D. T., 1972. "The Ultimate Properties of Bone Tissue: The Effects of Yielding," *Journal of Biomechanics,* **5**(1) .

[185] Simkin, A., and Robin, G., 1973. "The Mechanical Testing of Bone in Bending," *Journal of Biomechanics,* **6**(1) pp. 31-36.

[186] Reilly, D. T., Burstein, A. H., and Frankel, V. H., 1974. "The Elastic Modulus for Bone," *Journal of Biomechanics,* **7**(3) pp. 271-272.

[187] Burstein, A. H., Reilly, D. T., and Martens, M., 1976. "Aging of Bone Tissue: Mechanical Properties," *Journal of Bone and Joint Surgery (American),* **58**(1) pp. 82-86.

[188] Hvid, I., 1988. "Mechanical Strength of Trabecular Bone at the Knee." *Danish Medical Bulletin,* **35**(4) pp. 345-365.

[189] Hvid, I., Bentzen, S. M., Linde, F., Mosekilde, L., and Pongsoipetch, B., 1989. "X-Ray Quantitative Computed Tomography: The Relations to Physical Properties of Proximal Tibial Trabecular Bone Specimens," *Journal of Biomechanics,* **22**(8-9) pp. 837-844.

[190] Burgers, T. A., Mason, J., Niebur, G., and Ploeg, H. L., 2008. "Compressive Properties of Trabecular Bone in the Distal Femur," *Journal of Biomechanics,* **41**(5) pp. 1077-1085.

[191] Heiner, A. D., and Brown, T. D., 2003. "Structural Properties of an Improved Re-Design of Composite Replicate Femurs and Tibias," *Transactions of the 29th Society for Biomaterials,* **26** pp. 702.

[192] Heiner, A. D., 2008. "Structural Properties of Fourth-Generation Composite Femurs and Tibias," *Journal of Biomechanics,* **41**(15) pp. 3282-3284.

[193] Szivek, J.A., and Gharpuray, V.M., 2000. "Strain gauge measurements from bone surfaces," in *Mechanical Testing of Bone and the Bone-Implant Interface,* Y. H. An and R. A. Draughn (eds). CRC Press, Boca Raton, FL. pp. 305-320, Chap. 20.

[194] Coope, M., "How they Work: The Strain Gauge," *Sensorland.com, The online information centre for sensing and measurement.* Copidate Technical Publicity, Accessed March 12, 2009, <http://www.sensorland.com/HowPage002.html>.

[195] National Instruments, 2008. "Choosing the Right Strain-Gauge for Your Application," *NI Developer Zone.* National Instruments Corportaion, Austin, TX, USA. Accessed September 29, 2008, <http://zone.ni.com/devzone/cda/tut/p/id/3092>.

[196] Krimbalis, P., 2004. "A Validated Finite Element Study of Blunt Trauma to the Human Maxilla," M.A.Sc. Thesis, Ryerson University, Toronto, ON, Canada.

[197] National Instruments, 2008. "How is Temperature Affecting Your Strain Measurement Accuracy?" *NI Developer Zone.* National Instruments Corportaion, Austin, TX, USA. Accessed September 29, 2008, <http://zone.ni.com/devzone/cda/tut/p/id/3432>.

[198] Weymouth, L., 1991. "Strain gage system and component considerations," in *Strain Gage User's Handbook,* R. L. Hannah and S. E. Reed (eds). Elsevier Applied Science, and Society for Experimental Mechanics (SEM), New York, NY, USA (Elsevier); Bethel, CT, USA (SEM). pp. xiv, 476, Chap. 9.

[199] Vishay Micro-Measurements, 2008. "125UW General Purpose Strain Gages - Linear Pattern," *Vishay.com.* Vishay Intertechnology, Inc, Raleigh, NC, USA. Accessed March 15, 2009, <http://www.vishay.com/docs/11241/125uw.pdf>.

[200] Sawbones Worldwide, 2009. "Large Left Fourth Generation Composite Femur (Item #3406)," *Sawbones.com.* Pacific Research Laboratories, Inc, Accessed January 12, 2009, <http://www.sawbones.com/products/product.aspx?1937>.

[201] Illinois Tool Works, 2009. "Table Model Axial Torsion: FastTrack™ 8874," *Instron® Materials Testing Solutions (Instron.us).* Illinois Tool Works, Inc, Norwood, MA. Accessed February 25, 2009, <http://www.instron.us/wa/products/fatigue_testing/table_axial_torsion.aspx>.

[202] Swenson, L. W., Schurman, D. J., and Piziali, R. L., 1981. "Finite Element Temperature Analysis of a Total Hip Replacement and Measurement of PMMA Curing Temperatures," *Journal of Biomedical Materials Research,* **15**(1) pp. 83-96.

[203] Greene, K. A., Magoline, M. R., and Ripepi, V., 1998. "Primary Total Knee Arthroplasty using the Duracon Total Knee System: 2- to 5- Year Follow-Up Study of 100 Knees," *Johns Hopkins University Good Samaritan Hospital (www.aboutjoints.com).* Crystal Clinic and the Department of Orthopaedic Surgery, Summa Health System, Akron, OH, USA. Accessed March 10, 2009, <http://www.aboutjoints.com/physicianinfo/topics/duracontkasys/duracontka.htm>.

[204] Duffy, G. P., Murray, B. E., and Trousdale, R. R., 2007. "Hybrid Total Knee Arthroplasty: Analysis of Component Failures at an Average of 15 Years," *The Journal of Arthroplasty,* **22**(8) pp. 1112-1115.

[205] Vishay Micro-Measurements, 2005. "Instruction Bulletin B-127-14: Strain Gage Installations with M-Bond 200 Adhesive (Document no. 11127)," *Vishay.com.* Vishay Intertechnology, Inc, Raleigh, NC, USA. Accessed March 10, 2009, <http://www.vishay.com/docs/11127/11127_b1.pdf>.

[206] Integrated Measurement and Control, 2004, July 24. *"UNI2-8 for CRONOS-PL/-SL: Technical Specifications,"* TD_CRPL(SL)_UNI2-8_eng.doc, Version 1.1. Johne & Reilhofer, Seine, France. Available at <http://www.jr-france.com/bdfile/aaelement/c5af259017d29a76cd17b081b2fd520b.pdf>.

[207] Liau, J., Cheng, C., Huang, C., Lee, Y., Chueh, S., and Lo, W., 1999. "The Influence of Contact Alignment of the Tibiofemoral Joint of the Prostheses in in Vitro Biomechanical Testing," *Clinical Biomechanics,* **14**(10) pp. 717-721.

[208] Stewart, T., Jin, Z. M., Shaw, D., Auger, D. D., Stone, M., and Fisher, J., 1995. "Experimental and Theoretical Study of the Contact Mechanics of Five Total Knee Joint Replacements," *Proceedings of the Institution of Mechanical Engineers, Part H: Journal of Engineering in Medicine,* **209**(4) pp. 225-231.

[209] FUJIFILM NDT Systems Inc, 2009. "Prescale Film," FUJIFILM USA, Hanover Park, IL, USA. Accessed March 15, 2009, <http://www.fujindt.com/products/prescale/prescale-film.asp>.

[210] Freedman, M., 1988. *Clinical imaging: An introduction to the role of imaging in clinical practice,* Churchill Livingstone, New York, NY. xiv, 620 p.

[211] Shrivastava, S. C., Ahmed, A. M., Shirazi-Adl, A., and Burke, D. L., 1982. "Effect of a Cement-Bone Composite Layer and Prosthesis Geometry on Stresses in a Prosthetically Resurfaced Tibia," *Journal of Biomedical Materials Research,* **16**(6) pp. 929-949.

[212] Vasu, R., Carter, D. R., Schurman, D. J., and Beaupre, G. S., 1986. "Epiphyseal-Based Designs for Tibial Plateau Components-I. Stress Analysis in the Frontal Plane," *Journal of Biomechanics,* **19**(8) pp. 647-662.

[213] Beaupre, G. S., Vasu, R., Carter, D. R., and Schurman, D. J., 1986. "Epiphyseal-Based Designs for Tibial Plateau Components-II. Stress Analysis in the Sagittal Plane," *Journal of Biomechanics,* **19**(8) pp. 663-673.

[214] Garg, A., and Walker, P. S., 1986. "The Effect of the Interface on the Bone Stresses Beneath Tibial Components," *Journal of Biomechanics,* **19**(12) pp. 957-967.

[215] Shi, J. F., Wang, C. J., Laoui, T., Hart, W., and Hall, R., 2007. "A Dynamic Model of Simulating Stress Distribution in the Distal Femur After Total Knee Replacement," *Proceedings of the Institution of Mechanical Engineers, Part H: Journal of Engineering in Medicine,* **221**(8) pp. 903-912.

[216] Guess, T. M., and Maletsky, L. P., 2005. "Computational Modelling of a Total Knee Prosthetic Loaded in a Dynamic Knee Simulator," *Medical Engineering and Physics,* **27**(5) pp. 357-367.

[217] Chao, E. Y. S., MacWilliams, B. A., Chan, B., and Mejia, L. C., 1994. "Evaluation of a dynamic joint simulator using a prosthetic knee system," *Proceedings of the 1994 International Mechanical*

Engineering Congress and Expositio, November 6-11, 1994, Anonymous ASME, New York, NY, **28,** pp. 281-282.

[218] Turner, C. H., and Cowin, S. C., 1988. "Errors Induced by Off-Axis Measurement of the Elastic Properties of Bone," *Journal of Biomechanical Engineering,* **110**(3) pp. 213-215.

[219] Kurtz, S.M., 2004. "Alternatives to conventional UHMWPE for hip arthroplasty," in *The UHMWPE Handbook: Ultra-High Molecular Weight Polyethylene in Total Joint Replacement,* Anonymous Elsevier Academic Press, San Diego, CA. pp. 93-121, Chap. 6.

[220] Carpenter Technology Corporation, "Technical Datasheet: BioDur® CCM Plus® Alloy," *Carpenter Tech Centre (Cartech.com).* CRS Holdings Inc, Reading, PA. Accessed February 6, 2009, <http://www.cartech.com/techcenter.aspx?id=1692>.

[221] eFunda, I., "Pure Elements: Element Listing (Cobalt, Chromium, Molybdenum)," *Engineering Fundamentals (efunda.com): Materials Home.* eFunda, Inc, Sunnyvale, CA. Accessed February 5, 2009, <http://www.efunda.com/materials/elements/element_list.cfm>.

[222] Suedam, V., Souza, E. A. C., Moura, M. S., Jacques, L. B., and Rubo, J. H., 2009. "Effect of Abutment's Height and Framework Alloy on the Load Distribution of Mandibular Cantilevered Implant-Supported Prosthesis," *Clinical Oral Implants Research,* **20**(2) pp. 196-200.

[223] Mahmoud, A., Wakabayashi, N., Takahashi, H., and Ohyama, T., 2005. "Deflection Fatigue of Ti-6Al-7Nb, Co-Cr, and Gold Alloy Cast Clasps," *The Journal of Prosthetic Dentistry,* **93**(2) pp. 183-188.

[224] ANSYS Inc, 2009. "SOLID187 3-D 10-Node Tetrahedral Structural Solid," *kxcad.net; Release 11.0 Documentation for ANSYS.* Accessed March 9, 2009, <http://www.kxcad.net/ansys/ANSYS/ansyshelp/Hlp_E_SOLID187.html#solid187.tab.2.ft.6>.

[225] ANSYS Inc, 2005. "CONTA174 3-D 8-Node Surface-to-Surface Contact," *University of Illinois at Chicago Academic Computing and Communications Centre.* Accessed March 2, 2009, <http://uic.edu/depts/accc/software/ansys/html/elem_55/chapter4/ES4-174.htm>.

[226] ANSYS Inc, 2009. "TARGE170 3-D Target Segment," *kxcad.net; Release 11.0 Documentation for ANSY.* Accessed March 9, 2009, <http://www.kxcad.net/ansys/ANSYS/ansyshelp/Hlp_E_TARGE170.html>.

[227] ANSYS Inc, 2005. "TARGE170 3-D Target Segment," *University of Illinois at Chicago Academic Computing and Communications Centre.* Accessed March 2, 2009, <http://uic.edu/depts/accc/software/ansys/html/elem_55/chapter4/ES4-170.htm>.

[228] Murray, M. P., Drought, A. B., and Kory, R. C., 1964. "Walking Patterns of Normal Men," *Journal of Bone and Joint Surgery (American),* **46**(2) pp. 335-360.